# The Cenozoic evolution of crustal shortening and left-lateral shear in the central East Kunlun Shan: implications for the uplift history of the Tibetan Plateau


**Authors**

Lydia M. Staisch[1, 2, †], Nathan A. Niemi[1], Marin K. Clark[1], Chang Hong[3]

**Affiliations**

[1] Department of Earth and Environmental Sciences, University of Michigan, Ann Arbor, MI, USA

[2] (now at) US Geological Survey, Geology Minerals Energy and Geophysics Science Center, Moffett Field, CA, USA

[3] Institute of Earth Environment, CAS, Xi'an, China

[†] Corresponding author: lstaisch@usgs.gov


## Key Points

1) The central East Kunlun Shan is an ideal setting to investigate the tectonic evolution of northern Tibet and plateau-wide geodynamic drivers
2) The central East Kunlun Shan experienced crustal shortening from Paleocene–Oligocene time followed by a 23-20 Ma onset of strike-slip faulting
3) The plateau-wide mid-Miocene onset of strike-slip and normal faulting signals the attainment of high GPE and elevation


## ABSTRACT

The timing of crustal shortening and strike-slip faulting along the East Kunlun Shan provides insight into the history of surface uplift and may constrain the time at which the Tibetan Plateau reached high elevations. We investigate a series of extensional basins and restraining bends along the Xidatan strand of the Kunlun strike-slip fault, which provide an ideal setting to unravel the tectonic history of the northern plateau margin. We present new apatite (U-Th)/He, apatite fission track, and zircon (U-Th)/He ages and QTQt thermal modeling, $^{40}Ar/^{39}Ar$ fault gouge dating, and structural mapping from the central East Kunlun Shan.

Our data suggest that the East Kunlun Shan experienced slow to negligible exhumation until late Cretaceous time, followed by an increase in rate by 65 – 50 Ma. Along with a ~47 Ma fault gouge age, we posit that the Paleocene–early Eocene was a time of crustal shortening along the northern plateau. Rapid exhumation along transpressional portions of the Xidatan fault initiated by 23 – 20 Ma, which we interpret as the local onset of strike-slip faulting. An early Miocene transition from north-south crustal shortening to left-lateral shear along the East Kunlun Shan, the onset of normal and strike-slip faulting in central and southern Tibet by 18 Ma, and lower crustal flow in eastern Tibet by 13 Ma, suggests the establishment of orogen-wide east-west oriented extension and extrusion by the middle Miocene. The plateau-wide shift in stress accommodation implies that high gravitational potential energy, and likely high elevation, was attained by the middle Miocene.

## 1. INTRODUCTION

The timing of onset of strike-slip faulting within the East Kunlun Shan, located along the northern margin of the Tibetan Plateau, is an outstanding controversy with significant implications for unraveling the tectonic evolution of the Himalayan-Tibetan orogen. Currently, the Kunlun fault accommodates convergence between India and Eurasia via left-lateral shear at a rate of ~10 – 11 mm $yr^{-1}$ (Avouac and Tapponnier, 1993; van der Woerd et al., 1998, 2000, 2002; Li et al., 2005; Kirby et al., 2007). However, the East Kunlun Shan was previously the site of north-south oriented pure shear deformation, which is suggested to have initiated between 41 and 27 Ma (Mock et al., 1999; Jolivet et al., 2003; Wang et al., 2004; Yin et al., 2007; Wu et al., 2009; Clark et al., 2010; Duvall et al., 2013; Wang et al., 2017; Shi et al., 2018). The transition in structural style, from crustal thickening to eastward extrusion, along the East Kunlun Shan indicates a shift in the orientation of principal stresses. This kinematic change may directly relate to the attainment of high elevation and associated high gravitational potential energy of the northern Tibetan Plateau (Burke and Şengör, 1986; Platt and England, 1994; Rey et al., 2001). Few constraints exist on the timing of the switch from predominantly pure shear to simple shear deformation or when northern Tibet attained high elevation, thus fueling debate about when and how the Tibetan Plateau was uplifted to its modern elevation.

While most studies agree that left-lateral shear in the East Kunlun Shan initiated in the Cenozoic, there is uncertainty about the exact timing of onset (Kidd and Molnar, 1988; Wu et al., 2001; Jolivet et al., 2003; Fu and Awata; 2007; Dai et al., 2013; Duvall et al., 2013). Several studies infer that strike-slip faulting initiated in Plio – Pleistocene time based on the offset of fluvial and glacial features (Kidd and Molnar, 1988; Wu et al., 2001), while others infer ~10 Ma initiation of shear based on fault displacement and extrapolation of the modern fault slip rate (Fu and Awata, 2007). Uncertainties in both the timing of geomorphic feature development and in potential variations of the long-term slip history of the Kunlun fault result in uncertainties in estimates of the onset of shear. Alternatively, the timing of magmatism associated with extensional features near the Kunlun fault has been used to infer shear onset at 15 Ma (Jolivet et al., 2003). These volcanic constraints provide a minimum age for the onset of shear and suggest an older onset of faulting than interpretations from offset features and fault displacement (Kidd and Molnar, 1988; Wu et al., 2001; Fu and Awata, 2007). The initiation of shear at 20 – 15 Ma, with a possible phase from 30 – 20 Ma, is inferred from the initiation of rapid cooling from thermochronologic data (Dai et al., 2013; Duvall et al., 2013). However, difficulty in isolating the onset of strike-slip motion from the earlier, multi-phase deformation history of the northern plateau margin may lead to overestimates in the timing of strike-slip fault onset, particularly when using exhumation of discrete fault blocks as a proxy for the onset of lateral shear. An additional complicating factor is the heterogeneous onset of strike-slip faulting along the >1000 km length of the Kunlun fault, as inferred by Duvall et al. (2013). To unravel the kinematic history of the East Kunlun Shan, detailed structural analyses of faulting style in concert with age constraints on exhumation from thrust and strike-slip motion are necessary.

In this study, we present new low-temperature thermochronologic data and modeling from the central Kunlun fault zone and $^{40}Ar/^{39}Ar$ fault gouge dating to assess the tectonic evolution of the northern margin of the Tibetan Plateau. Strike-slip motion within the East Kunlun Shan has produced localized basin subsidence in *en echelon* rhombochasms and uplift along restraining bends, steps, and fault junctions (Fig. 1; Fu and Awata, 2007; Duvall et al., 2013), such as along the Xidatan segment of the Kunlun fault between the Dongdatan Valley and Deshuiwai Basin (Fig. 1). We focus our work along this section of the Kunlun fault because thrust faults are well exposed throughout the region, are commonly crosscut by major and subordinate strike-slip faults, and exposures found in extensional step-overs are ideal for isolating the timing of crustal shortening in the East Kunlun Shan. Additionally, restraining bends and fault junctures may concentrate strike-slip related vertical exhumation, and are ideal for constraining the initiation of strike-slip faulting. Along with structural mapping and previous work on normal and strike-slip fault initiation, these data clarify for the timing of stress reorganization throughout the Tibetan Plateau and provide the opportunity to link this shift to the attainment of high gravitational potential energy via surface uplift.

## 2. GEOLOGIC SETTING

The East Kunlun Shan form a boundary between the high-elevation (>4.5 km), low-relief surfaces of the Tibetan Plateau to the south and the moderate elevation Qaidam Basin (~2.5 km) to the north (Fig. 1). Originating as a Paleozoic suture between the Kunlun-Qaidam and Songpan-Ganzi terranes, the East Kunlun Shan is a long-lived tectonic boundary that has experienced multiple periods of tectonic reactivation, including Cretaceous shearing (Mock et al., 1999; Chen et al., 2002), Eocene – Oligocene crustal shortening (Yin et al., 2008; Wu et al., 2009; Clark et al., 2010), and recent left-lateral shear (van der Woerd et al., 1998; 2002). The multi-stage tectonic history of the East Kunlun Shan has resulted in a complex structural evolution with a diverse assemblage of rock types. Perhaps the most complete record of this complex history is found within the central portion of the East Kunlun Shan, where the Kunlun fault and subordinate fault splays have produced a series of structurally-controlled basins and narrow, intervening ranges.

### *2.1. Geologic units*

We focused our geologic mapping, structural analysis, and sample collection in the central East Kunlun Shan from the Dongdatan Valley in the west to the Deshuiwai Basin in the east. Rock units range from Proterozoic to Quaternary in age (Figs. 1 and 2; Qinghai Bureau of Geology and Mineral Resources (QBGMR), 1980; 1981). Below we describe sedimentary and metasedimentary units followed by igneous units exposed in the study area, organized from oldest to youngest.

#### *2.1.1. Sedimentary and metasedimentary units*

The Proterozoic Wanbaoguo Group, which largely consists of limestone, dolomite and shale, is crosscut by mafic dikes and is exposed north of the Middle Kunlun fault (Figs. 1 and 2B; QBGMR, 1980, 1981). The Carboniferous Haoteluowa Group is composed largely of marine carbonate with interbedded sandstone and shale and unconformably overlies the Wanbaoguo Group

(QBGMR, 1980, 1981). Within our field area, the Haoteluowa Group is exposed in fault contact with both Mesozoic and Cenozoic strata (Figs. 2A and 3; QBGMR, 1980, 1981). The Permian Ganjia and Maerzheng groups consist of marine carbonate, often fossiliferous, and locally metamorphosed to marble (QBGMR, 1980, 1981). These units are spatially extensive and form the steep topography to the north of the Dongdatan Valley and in the southeastern East Deshuiwai Mountains (Fig. 2). In the following sections, we refer to the Ganjia and Maerzheng units together as Permian carbonates.

The Triassic Babaoshan and Naocangjiangou groups are largely composed of shale, siltstone, and fine to coarse sandstone with limited conglomerate, arkose, fossil-bearing coal layers, and interbedded volcanic flows (QBGMR, 1980, 1981). In many regions, these units have been metamorphosed to greenschist facies (Wu et al., 2009). Regional stratigraphic work suggests that the Babaoshan Group unconformably overlies the Naocangjiangou Group (Wang et al., 2009). A 244 Ma volcanic tephra interbedded within the Naocangjianguo Group provides an early Middle Triassic age for the unit (Wu et al., 2010). We refer to these units together as Triassic metapelites in the following sections. In the east, the Jurassic – Cretaceous Yangqu Group is conformably deposited over the Babaoshan Group and both units are flat-lying to mildly tilted (Figs. 4A-B; QBGMR, 1980, 1981; Wang et al., 2009). Together, the Babaoshan, Naocangjianguo, and Yangqu groups are part of the A’nyemaqen mélange belt, deposited between the Qaidam block and South Kunlun terrane during the Mesozoic (Wang et al., 2009). The Yangqu Group consists of siltstone, arkosic sandstone, and conglomerate and tends to be brick red with grey-green mottling (Figs. 4B-C).

Previously, recognition of the Yangqu Group was limited localities within to the East Deshuiwai Mountains. However, our mapping and new age dating suggest that this unit is also exposed in the East Wenquan Basin and in Dongdatan Valley (Fig. 2B and 3) where it was previously mapped as Cenozoic terrestrial red bed strata (QBGMR, 1980, 1981). The Cenozoic age for well-indurated and strongly weathered red bed strata exposed in the Dongdatan Valley and on the north side of Wenquan Hu is called into question by recent detrital zircon analyses, which show zircon populations no younger than 174 Ma with well-defined age peaks at ~250 and ~425 Ma (Wu et al., 2019). As we will show below, our zircon (U-Th)/He ages in combination with the recent detrital zircon ages support an interpretation for an older depositional age. The new age and unit assignment for these terrestrial red bed strata are reflected in Figures 2A and 3.

Cenozoic strata are unconformably deposited across both Mesozoic and Paleozoic units and are exposed throughout the Dongdatan Valley and East Wenquan Basin, as well as to the south of the East Deshuiwai Mountains (Figs. 2, 3, and 4F; QBGMR, 1980, 1981). The depositional age of Cenozoic strata are not well constrained with absolute age dating. The unnamed Paleogene – Neogene red bed unit is composed of fluvial sandstone, lacustrine siltstone, and conglomerate (Fig. 4D) and can be distinguished from the Yangqu Group by its lack of induration, lack of weathering, and absence of green mottling. The Neogene Quguo Group is composed of lacustrine carbonates and fine-grained siltstone and is exposed in the eastern East Wenquan Basin (QBGMR, 1980, 1981). This unit is characteristically light greyish-yellow to pistachio green in color (Fig. 4E).

*2.1.2. Igneous units*

Igneous units are exposed throughout the central East Kunlun Shan and range from outcrop-sized plutonic bodies and volcanic flows to large intrusive and extrusive complexes. In the eastern portion of the field area (Fig. 2B), Permian granite intrudes the Paleozoic Wanbaoguo Group and is exposed in the high peaks to the north of the Middle Kunlun fault (QBGMR, 1980, 1981). The Triassic Babaoshan and Yalixige units are granitic and granodioritic intrusive complexes, respectively, over which the Babaoshan Group strata are unconformably deposited (Fig. 4A; QBGMR, 1980, 1981). The Babaoshan Group is interbedded with a thick sequence of basalt flows (Fig. 2B), which in some regions exhibits columnar jointing. These basalts are exposed directly south of the Middle Kunlun fault and in the eastern Deshuiwai Basin (QBGMR, 1980, 1981). Within the western portion of our field area (Figs. 2A and 3), igneous units are sparse, small in volume, and generally intrude into the Triassic Naocangjiangou Group (QBGMR, 1980, 1981). The small intrusions are generally rhyolitic to dacitic in composition and have been moderately metamorphosed along with the host rock. These magmatic intrusions are thought to be associated with Triassic metamorphic overprint in the Xidatan area, dated between 212 and 242 Ma (Liu et al., 2005). Andesitic – dacitic tephra layers are interbedded within the Triassic Naocangjiangou Group and have been dated with U-Pb methods at ~244 Ma (QBGMR, 1980, 1981; Wu et al., 2010). Where observed in the eastern portion of the field area (Fig. 2B), these units tend to be <1 m in thickness. In the southern East Deshuiwai Mountains, a package of andesitic lavas is faulted into place (Fig. 2B; QBGMR, 1980, 1981). The structural complexity associated with the exposure of these andesitic rocks obscures the relationship with any specific sedimentary unit. South of the East Deshuiwai Mountains, small-volume andesitic intrusions are exposed within the Triassic Naocangjiangou Group (QBGMR, 1980, 1981).

### *2.2. Structural Geology*

#### *2.2.1. North-south oriented crustal shortening*

The dominant style of modern deformation in the central East Kunlun Shan is left-lateral strike-slip faulting (Molnar and Tapponnier, 1978; Kidd and Molnar, 1988); however, evidence for north-south contraction is also preserved (Wu et al., 2007, 2009). Throughout the study region, the

Carboniferous Haoteluowa Group and the Permian Ganjia and Maerzheng Groups have been thrust over Triassic metapelites (Figs. 2A and 3; QBGMR, 1980, 1981). This fault relationship is best exposed on either side of the Dongdatan Valley, along the northern East Wenquan Basin, and as a series of small klippen in a tectonic sliver immediately north of the Wenquan Reservoir (Figs. 2A and 3). Deformed Triassic Naocangjiangou metapelites preserve tight east-west oriented folds and near-vertical axial planar cleavage (Fig. 5A), suggesting that the maximum compressive stress was oriented north-south, in modern coordinates, and the least compressive stress was oriented vertically during the episode of deformation preserved in these strata. Based on field observations and the degree of tilting preserved in the strata, the contractional strain preserved in Jurassic to Cenozoic sedimentary units is far less than in the Triassic Naocangjiangou. Thus, major shortening of the Triassic strata took place prior to deposition of the Yangqu Group, and perhaps before deposition of the Triassic Babaoshan Group. In the central East Wenquan Basin, Cenozoic red beds are typically mildly tilted and overlie the Triassic Naocangjiangou Group in angular unconformity (Fig. 4F), with the exception of red bed exposures near strike-slip faults that are locally strongly deformed. North of the Wenquan Reservoir, the Wenquan Hu thrust fault has been eroded on either side and is preserved as a klippe (Figs. 2A and 3) that places Triassic metapelites over Jurassic – Cretaceous Yangqu Group (Fig. 5D).

*2.2.2. Left-lateral shear*

The Kunlun fault zone deforms a broad region within the central East Kunlun Shan, such that left-lateral faulting is pervasive within the study area. Major faults identified include the Xidatan fault (the Xidatan-Dongdatan segment from van der Woerd et al [2002]), which is the main strand of the Kunlun fault east of the Kunlun Pass, and the Middle Kunlun fault, which delineates a major structural boundary between Proterozoic and Triassic strata in the eastern portion of the field area (Figs. 1 and 2B; QBGMR, 1980, 1981; Kidd et al., 1988). The mountainous terrane north of the Dongdatan Valley is crosscut by left-lateral faults that are subordinate to the main Xidatan fault (Fig. 2A). Subordinate faults offset Permian – Cenozoic strata, form well defined gouge and fault rock zones, and tend to produce steep, near-vertical, topography when exposed in the Permian carbonate units (Figs. 5B and 5C). Few minor strike-slip faults are exposed along the southern Dongdatan Valley (Fig. 2A).

Where the Xidatan fault crosscuts the East Deshuiwai Mountains, to the east of Dongdatan Valley, it has created a wide fault gouge zone, up to 100s of meters in thickness, and forms a major structural discontinuity that separates Triassic metapelites to the north from Permian carbonate to the south (Fig. 2B; QBGMR, 1980, 1981). Within the East Deshuiwai Mountains, left-lateral faulting is accommodated over a broad network of multiple strike-slip faults. The Xidatan fault and subordinate faults occasionally carry small fault bound blocks of allochthonous Permian carbonates that are isolated within a separate lithologic unit (QBGMR, 1980, 1981). The southern boundary of the East Deshuiwai Mountains is a strike-slip fault, here named the Da Lang fault (after a large wolf sighted nearby), which continues to the west into the East Wenquan Basin and eventually merges with the Xidatan fault (Figs. 2A-B; QBGMR, 1980, 1981).

*2.2.3. Modern fault activity*

Offset Quaternary alluvial strata along the Xidatan and Da Lang faults, along with active seismicity, suggests that strike-slip motion is presently accommodated within the central East Kunlun Shan (U.S. Geological Survey National Earthquake Information Center [USGS NEIC]). In the western and central portions of the field area, the surficial trace of the Xidatan fault is evident from pressure ridges and offset Quaternary fluvial and alluvial features and is occasionally associated with hot springs and sag ponds. Terrestrial cosmogenic nuclide dating of offset river terraces in Dongdatan Valley suggests that the Xidatan fault has accommodated 10 – 11 mm $yr^{-1}$ of Late Pleistocene – recent left lateral motion (van der Woerd et al., 1998; 2002). Modern seismic data also suggest that faults within the East Deshuiwai Mountains are active (USGS NEIC). Slip rates along the Middle Kunlun fault and subordinate strike-slip faults have not been quantified and seismic data does not provide evidence for modern fault activity (USGS NEIC). We found no compelling field evidence for recent faulting along the Middle Kunlun fault in the mapping area, suggesting that it may not be a major active structure.

## 3. LOW-TEMPERATURE THERMOCHRONOLOGIC DATA

The timing of fault initiation can be derived from thermochronologic methods in extensional or contractional deformation regimes, where tectonic activity generates topographic relief and a local increase in erosion rate (Ehlers and Farley, 2003; Braun, 2005). Conversely, thermochronologic studies along strike-slip faults are relatively few since strike-slip faulting typically results in the lateral translation of fault blocks rather than vertical exhumation. Certain strike-slip fault geometries, however, are capable of producing vertical exhumation of sufficient magnitude to be recorded by low-temperature thermochronology, such as near fault junctions, terminations, and splays, as well as within restraining bends and along non-vertical fault planes (Spotila et al., 1998; 2001; 2007; Benowitz et al., 2011; Duvall et al., 2013; Niemi et al., 2014). We targeted these types of structural environments within the central East Kunlun Shan to constrain the timing of strike-slip fault motion. In order to constrain the timing of thrust faulting, on the other hand, we were required to avoid locations in which strike-slip related deformation had caused considerable exhumation. We therefore also targeted sampling sites in which clear thrust fault relationships exist and where we observed strike-slip related exhumation to be absent or negligible (Fig. 1).

### *3.1. Sample collection and preparation*

Bedrock samples were collected from apatite and zircon bearing rock types, including volcanic and plutonic rocks of andesitic-dacitic composition (Table 1). We also collected medium to coarse-grained sandstones that may have experienced sufficient burial to reset the apatite and zircon thermochronologic system prior to more recent fault-related exhumation. The limited topographic relief and heterogeneous geologic setting of our study site limited our ability to collect steep elevation transects, so we dated single samples to constrain the time of exhumation through the apatite (U-Th)/He, apatite fission-track, and zircon (U-Th)/He effective closure temperatures. Sample locations and descriptions are available in Table 1.

Once collected, samples were crushed and sieved using standard laboratory procedures. Apatite and zircon crystals were separated from the bulk sample using standard density and magnetic techniques. Crystals were handpicked at the University of Michigan to ensure grain quality using standard procedures (Farley and Stockli, 2002; Reiners et al., 2002). For (U-Th)/He analyses, apatite and zircon crystals were individually analyzed for He content at the University of Michigan HeliUM Laboratory following procedures in Niemi and Clark (2016). Apatites for (U-Th)/He dating were analyzed for U, Th, and Sm content at the University of Arizona Radiogenic Helium Dating Laboratory, and zircons for (U-Th)/He dating were analyzed for U and Th content at the University of Colorado Thermochronology Research and Instrumentation Laboratory. Apatite fission-track analyses were completed for one sample (12DDT10) at the University of Cincinnati and for seven other samples at the University of Arizona. Mounts of apatite grains were etched in 5 M $HNO_3$ solution (5.5 M for 12DDT10) at 21ºC for 20 s to expose tracks from spontaneous fission of $^{238}U$. Following neutron irradiation at the Oregon State TRIGA Reactor, mica external detectors were etched in 40% HF at 20ºC for 45 min (40 min for 12DDT10) to reveal induced tracks.

### *3.2. Apatite (U-Th)/He age results*

We collected and dated 19 bedrock samples for apatite (U-Th)/He thermochronology with a minimum of 4 apatite single-grain replicates analyzed per sample. Measured AHe ages range widely across the central East Kunlun Shan, with mean ages between 20 and 148 Ma (Tables 1 and S1). Two samples, 13DDT23 and 13DDT36, were removed from further analysis because the standard deviation of replicate apatite ages exceeded 20%, indicating that the mean ages for these samples are not well constrained (Table 1). Five other samples exhibit correlations between age and effective Uranium content (eU) or grain size (samples 12DDT07, 13DDT008, 13DDT009, 13DDT016, 13DDT017; Figs. S1, S2). In the following paragraphs, we describe the results and geologic setting for samples from west to east.

We collected nine bedrock samples from Dongdatan Valley and the East Wenquan Basin. The westernmost sample, 11UMT53, was collected from a small plutonic body that intruded the Triassic Naocangjiangou Group prior to metamorphism. This sample had an AHe age of 19.2 ± 2.1 Ma (Fig. 2A; Table 1). To the east, samples 12DDT24, 12DDT10, 11UMT63, and 12DDT09, and 12DDT07 were collected from small plutonic bodies within the hanging wall of the Wenquan Hu thrust fault (Figs. 2A, 3, and 5D; Table 1). The AHe ages for these samples range between 25 and 33 Ma, with the exception of 12DDT07 that was dated at 63.0 ± 7.1 Ma (Table 1). Sample 12DDT07 shows a strong correlation between eU content and AHe age (Table S1; Fig. S1), the implications of which are discussed below.

From the footwall of the Wenquan Hu thrust fault, samples 11UMT56 (sandstone) and 12DDT17 (interbedded tephra) were collected from the Yangqu Group strata. The mean AHe age for sample 11UMT56 is 21.5 ± 3.7 Ma and the mean AHe age for sample 12DDT17 is 37.4 ± 6.0 Ma (Figs. 2A and 3; Table 1). In the northwestern corner of the East Wenquan Basin, sample 12DDT22 was collected from the upper Triassic Babaoshan Group and provides an AHe age of 38.3 ± 10.0 Ma (Fig. 2A; Table 1). Sample 12DDT22 was collected ~2 km to the north of the surface exposure of the Middle Kunlun fault (Fig. 2A).

Within the East Deshuiwai Mountains, we collected samples 13DDT008 and 13DDT009 from interbedded volcanic and metamorphosed arkosic sandstone layers, respectively, of the Triassic Naocangjiangou Group. The replicate AHe ages from 13DDT008 range between 86 and 201 Ma, and the replicate ages from sample 13DDT009 range between 16 and 309 Ma (Fig. 2B; Table 1). Apatite replicates for samples 13DDT008 and 13DDT009 show a strong correlation between AHe age and crystal size, suggesting slow cooling (Fig. S2; Reiners and Farley, 2001). To the southeast of the East Deshuiwai Mountains, sample 13DDT017, collected from a small plutonic body that intrudes into the Triassic Naocangjiangou Group, displays a strong correlation between age and eU. Within the East Deshuiwai Mountains, sample 13DDT011 was collected from a metamorphosed volcanic unit and provides an AHe age of 31.8 ± 4.1 Ma (Fig. 2B; Table 1). This region of the East Deshuiwai Mountains is strongly deformed due to strike-slip motion and largely composed of Permian marine carbonate, such that exposed apatite-bearing rock types are scarce.

To the north of the Deshuiwai Basin, we collected several igneous samples that intrude the Proterozoic Wanbaoguo Group. Apatite quality was poor and only one sample (13DDT032) provided reproducible AHe ages. Sample 13DDT032 was collected from an andesitic dike and provides a mean AHe age of 36.4 ± 7.1 (Fig. 2B; Table 1). Within the center of the Deshuiwai

Basin, the Triassic Babaoshan and Jurassic – Cretaceous Yangqu Group are fairly undeformed and well exposed. We collected a bedrock sample from an arkosic sandstone of the Babaoshan Group (13DDT016), which provided an AHe age of 49.5 ± 9.5 Ma (Fig. 2B; Table 1). This sample shows a correlation between eU and replicate age (Fig. S1), similar to samples 13DDT017 and 12DDT07. Nearby, to the northeast, several plutonic units of lower Triassic age are exposed (Fig. 2B; QBGMR, 1980; 1981). We collected two samples, 13DDT022 and 13DDT023, from these large intrusions of andesitic – dacitic composition. Sample 13DDT022 was dated using AHe analysis at 35.4 ± 6.7 Ma and 13DDT023 has very poor replicate agreement and was omitted from further analysis (Tables 1 and S1).

### *3.3. Apatite fission-track age results*

We selected 8 samples for apatite fission-track (AFT) analysis (Figs. 2A and 3; Tables 1 and S2) and analyzed between 12 and 23 apatite grains for each sample. Samples with fewer than 20 analyzed apatite crystals suffered from mediocre apatite yield (11UMT56, 13DDT011, 13DDT022). All samples passed the $\chi 2$-test, suggesting that all grains from each sample are representatives of a single age population (Table S2; Galbraith, 1981). Track density was insufficient for track length analyses in most mounted samples aside from sample 12DDT09, from which we measured a mean confined track length of 13.93 ± 0.20 μm (n=13).

The apatite fission-track age for the westernmost sample (11UMT53) is within uncertainty of the apatite (U-Th)/He age, at 19.0 ± 2.2 Ma (Figs. 2A and 3; Table 1). To the east, AFT ages for samples 11UMT56 and 12DDT24 are within uncertainty of each other at 43.2 ± 4.4 Ma and 43.0 ± 3.8 Ma, respectively (Figs. 2A and 3; Table 1). Near the Wenquan Reservoir, AFT ages for samples 12DDT09 and 12DDT10 are 47.0 ± 5.1 Ma and 52.0 ± 4.8 Ma, respectively, and within uncertainty of each other (Figs. 2A and 3; Table 1). Between the Xidatan and Da Lang fault strands, sample

13DDT011 was dated at 64.4 ± 12.8 Ma (Fig. 2B; Table 1). We obtained Cretaceous AFT ages of 114.9 ± 12.9 for sample 13DDT032 and 96.5 ± 14.9 Ma for sample 13DDT022 collected from the Deshuiwai Basin (Fig. 2B; Table 1).

### *3.4. Zircon (U-Th)/He age results*

We obtained zircon (U-Th)/He (ZHe) ages for 6 of the 19 samples collected for thermochronologic analysis (Figs. 2A and 3; Table 1). We dated a minimum of 3 zircon crystals per sample (Table S3). All samples had reproducible ZHe ages with standard deviation of replicate zircon ages less than 20% of the mean age (Tables 1 and S3).

The zircon (U-Th)/He age for the westernmost sample collected for thermochronologic analysis (11UMT53) provided an Eocene age of 39.6 ± 2.8 Ma (Figs. 2A and 3; Table 1). To the east, samples 12DDT09 and 12DDT10 were collected from the hanging wall of the Wenquan Hu thrust fault and have ZHe ages of 98.1 ± 20.1 Ma and 72.5 ± 9.2 Ma, respectively (Figs. 2A and 3; Table 1). Samples 11UMT56 and 12DDT17 in the footwall of the Wenquan Hu thrust fault, and were dated using ZHe analysis at 256.6 ± 59.3 Ma and 140.0 ± 12.4 Ma, respectively (Figs. 2A and 3; Table 1). We collected sample 12DDT22 from the northern East Wenquan Basin, from which we obtained a ZHe age of 97.1 ± 11.6 Ma (Fig. 2A; Table 1).

## 4. LOW-TEMPERATURE THERMOCHRONOLOGY MODELING AND IMPLICATIONS

### *4.1. Implications for the timing of red bed deposition in the Dongdatan Valley*

The age of strata in the footwall of the Wenquan Hu thrust fault provides an important constraint for thermal modeling and interpretations of local and regional faulting. While previous mapping suggests that the footwall strata are Paleocene – Neogene, our thermochronologic data suggest otherwise. The mean ZHe ages attained from the footwall samples 11UMT56 and 12DDT17 are over 100 Ma apart and 11UMT56 displays considerable scatter. Furthermore, our zircon He ages from 11UMT56 are older than the youngest detrital U-Pb zircon ages and generally overlap with a major 200 – 280 Ma detrital U-Pb age populations from the same strata (Wu et al., 2019; McRivette et al., 2019). From this, we suggest that the red bed strata in the footwall of the Wenquan Hu thrust fault was not buried to sufficient depth to reset the zircon He system, such that the ages from 11UMT56 represent detrital zircon cooling ages. Furthermore, the 140 Ma zircon (U-Th)/He age from 12DDT17 is much younger than the ~245 Ma maximum depositional age from detrital U-Pb data (McRivette et al., 2019) and thus represent syn-depositional volcanic tephra ages. Given the Cretaceous ZHe age for sample 12DDT17, we suggest that these strata are not Cenozoic, as previously mapped, but are rather part of the Jurassic – late Cretaceous Yangqu Group. Since the ZHe ages do not inform us about the cooling history of the footwall fault block, they are excluded from QTQt modeling, below.

### *4.2. Thermal modeling results*

In order to quantify the timing and rate of cooling of different fault blocks in the central East Kunlun Shan, we used QTQt version 5.5.1c, a program for modeling low-temperature thermochronology that employs a Bayesian trans-dimensional Markov chain Monte Carlo inversion scheme (Gallagher, 2012). For most thermal models, we grouped multiple samples to model fault blocks because QTQt is particularly useful for handling large datasets. For models with multiple samples, we allowed the temperature offset between samples to vary over time and input sample elevations to inform the model of modern temperature offset. The fault blocks modeled include a block proximal to the Xidatan fault and the East Deshuiwai Mountains restraining bend to constrain the timing of strike-slip related exhumation, the Wenquan Hu thrust fault hanging wall and footwall to constrain the timing of thrust fault related exhumation, and the Deshuiwai Basin to constrain the cooling history in the eastern study region and discern whether the Middle Kunlun fault has caused recent exhumation (Fig. 6). A list of samples, types of thermochronologic data, geologic constraints, reasoning for geologic constraints, and general priors for each fault block modeled are provided in Table 2.

For every model, we ran $10^4$ burn-in trials and $10^5$ post-burn-in trials, the latter of which are retained for analysis. Additionally, we inspected the posterior iteration chain to ensure that trials had sufficiently sampled the parameter space. We placed minimal geologic constraints on our models to avoid forcing the results to any preconceived prior assumptions. We require that every model reached surface temperatures (0 – 20ºC) by 0 Ma. For the Wenquan Hu footwall block, we required the model to be near surface temperatures (0 – 20ºC) during a broadly defined depositional age of the Yangqu Group (170 – 50 Ma). In order to assess whether a model fit well or if additional parameters and constraints needed adjustment, we compared predicted and observed thermochronologic ages for mean sample ages and individual grain ages (Fig. 7).

*4.2.1. Xidatan fault model results*

To model cooling of the Xidatan section of the Kunlun fault and constrain the timing of strike-slip faulting related exhumation, we used a single sample collected from a small intrusive body near the trace of the main fault strand (Fig. 2A). Sample 11UMT53 was collected in a region for which expected exhumation due to strike-slip faulting is expected based on the high relief of the landscape associated with pervasive strike-slip fault zones (Fig. 1). The apatite (U-Th)/He and fission track ages are within uncertainty of each other, and the zircon (U-Th)/He ages are the youngest in our dataset (Table 1). Our QTQt model results show a broad swath of possible time-temperature paths prior to 55 Ma, with best fit model results showing isothermal holding, followed by an acceleration in cooling that likely initiated between 55 and 40 Ma (Fig. 6A). This early Cenozoic stage of cooling is not required by all models but is preferred by the Maximum Likelihood and Maximum Posterior models (Fig. 6A; MLM and MPM). Rapid cooling of 20.0 – 21.6 °C Myr$^{-1}$ initiated ca. 23 Ma, followed by a deceleration in cooling rate by ca. 17 Ma (Fig. 6A). The modeled and observed thermochronologic ages are in general agreement with each other, with (U-Th)/He mean predicted and observed ages within uncertainty of each other (Fig. 7A). However, models were unable to reproduce the young apatite fission track age (Fig. 7A). Despite the difficulty in modeling overlapping AHe and AFT ages, the similarity in these ages qualitatively requires rapid exhumation at this time.

#### *4.2.2. Wenquan Hu thrust fault hanging wall model results*

For our QTQt model for the hanging wall of the Wenquan Hu thrust fault, we used five samples with apatite (U-Th)/He, apatite fission track, and zircon (U-Th)/He ages to constrain time-temperature paths. Samples were collected from a klippe exposed near Wenquan Reservoir (Fig. 3), in a region where exhumation due to strike-slip faulting is not observed (Fig. 1). Model results show slow to moderate cooling rates over Mesozoic time. Cooling rates accelerated by 50 – 65 Ma and remained elevated for roughly until 19 – 21 Ma (Fig. 6B), followed by slow to negligible cooling from the Miocene to present time.

Predicted mean thermochronologic ages are generally in good agreement with observed data, with the notable exception of sample 12DDT07 (Fig. 7E). This sample shows a strong correlation between effective uranium and apatite (U-Th)/He age (Fig. S1), suggesting that ages may be influenced by radiation damage in the apatite crystals that accumulated during a period of isothermal holding. Isothermal holding and the accumulated radiation damage may have occurred at an earlier period in time, possibly Cretaceous given the observed ages, thus inhibiting our ability to discern the Cenozoic cooling history from sample 12DDT07. The possible existence of micro-inclusions is another potential explanation for the unusually old observed ages in 12DDT07. We modeled the Wenquan Hu hanging wall both with and without 12DDT07 ages and found that model results are agnostic to this sample. Selecting the RDAAM radiation damage model in QTQt did not improve the fit to sample 12DDT07. In our thermal model, we also included zircon (U-Th)/He ages from sample 12DDT10, despite the scatter in individual grain ages. Inclusion of these ages results in a better fit to all other thermochronologic data (Fig. 7B), and model results are also capable of matching the mean observed zircon (U-Th)/He ages for 12DDT10.

While our mean observed and predicted ages show good agreement, some of the individual modeled and observed AHe grain ages do not agree well (Fig. 7B). This is likely a result of combining multiple samples into a single thermal model of the entire fault block. To investigate this further, we modeled each sample individually in QTQt. We found that differences between observed and predicted individual grain ages are reduced when each sample is modeled separately, however the QTQt algorithm simplifies the time-temperature paths for each sample, as these are constrained by fewer data points (Fig. S3). Nonetheless, the individually modeled sample runs show significant overlap in preferred time-temperature paths, suggesting a common exhumation history. Indeed, we find that the modeled time-temperature histories for individually modeled samples are within uncertainty of the predicted time-temperature paths modeled using all samples together (Fig. S3). We therefore suggest that modeling the samples together is advantageous and informative about the exhumation history experienced by all hanging wall samples, despite having slightly diminished goodness of fit to individual AHe ages.

*4.2.3. Wenquan Hu thrust fault footwall model results*

We used two samples collected from the Wenquan Hu thrust fault footwall strata (11UMT56 and 12DDT17) to constrain the timing of burial due to thrust faulting and subsequent regional exhumation. Samples were collected in a region where significant exhumation due to strike-slip faulting is not expected (Fig. 1). Our model included a surface temperature constraint for the depositional age of the terrestrial Yangqu sedimentary strata, forcing time-temperature paths to pass through 10 ± 10ºC from 170 – 50 Ma (Fig. 6C). Since the samples were collected several kilometers from each other (Fig. 3), we allowed the initial temperature offset to vary between 20 ± 20ºC, but required that the temperature offset converge to more similar values by modern time.

Model results show a range of possible time-temperature paths prior to ca. 65 Ma, after which time model results show with heating from near-surface temperatures. Heating is followed by moderate, monotonic cooling rates to surface temperatures initiating by 50 Ma. Predicted thermochronologic ages for model results agree well with the observed ages (Fig. 7C and 7F). Based on the similarity of apatite fission track ages in the hanging wall and footwall (Table 1), we suggest that the Wenquan Hu thrust fault ceased motion by 43 Ma, and that the hanging wall and footwall began to cool together after this time. This is supported by the similarity in post-43 Ma cooling rates for the hanging wall and footwall thermal models, where the average post-43 Ma cooling rate for the hanging wall and footwall models are 1.9 ± 0.3 °C $Myr^{-1}$ and 2.0 ± 0.3 °C $Myr^{-1}$, respectively.

### *4.2.4. East Deshuiwai Mountains restraining bend model results*

We modelled the time-temperature paths for the East Deshuiwai Mountains, which is a restraining bend between the East Wenquan and Deshuiwai basins, to constrain the timing of strike-slip related exhumation (Figs. 1 and 2B). For this model, we included apatite (U-Th)/He ages from samples 13DDT008 and 13DDT009. Apatite ages from these samples display significant scatter between 16 – 309 Ma (Table 1). These samples were collected from the Triassic-age Babaoshan unit, and thus the apatite (U-Th)/He ages appear to record partial resetting of the (U-Th)/He systematics arising from post-depositional exhumation of the region. Both samples also show a strong correlation between crystal size and age (Tables 1 and S1). Grain size-age correlations are often associated with isothermal holding in the partial retention zone followed by rapid uplift (Reiners and Farley, 2001). Model results show generally slow cooling over Mesozoic – present time, with a possible brief increase in cooling rate between 160 – 120 Ma (Fig. 6D). Unfortunately, predicted model ages do not agree well with observed apatite (U-Th)/He ages (Fig. 7D). Qualitative assessment of sample ages from the East Deshuiwai Mountain may provide some assessment on the timing of exhumation within the restraining bend, as discussed below, but detailed cooling information is not resolved by inverse thermal modeling of these samples, likely due to the wide spread in observed grain ages.

*4.2.5. Deshuiwai Basin and Middle Kunlun fault model results*

We used apatite (U-Th)/He and fission track ages from samples 13DDT016, 13DDT022 and 13DDT032 to model time-temperature paths in QTQt for the Deshuiwai Basin and the Middle Kunlun fault (Fig. 2B). The goal of this modeling approach was to constrain the timing and rate of regional cooling of the Deshuiwai Basin, where we do not observe field evidence for exhumation due to motion on Cenozoic structures (Fig. 1). The range immediately north of the Middle Kunlun fault, on the other hand, may have a history of exhumation separate from the Deshuiwai Basin (Fig. 1). We tested whether or not faulting along the Middle Kunlun fault caused significant exhumation north of Deshuiwai Basin by dating sample 13DDT032. The apatite (U-Th)/He and fission track results from 13DDT032 are within uncertainty of ages from 13DDT022 (Tables 1, S1 and S2), and are collected on the other side of the Middle Kunlun fault (Fig. 2B), suggesting that both samples have experienced similar cooling histories since mid-Cretaceous time. Thus, we used all three samples in QTQt to model the cooling history of the Deshuiwai Basin and mountains immediately to the north (Fig. 6E). Since sample 13DDT016 was collected from the terrestrial Triassic Babaoshan Group, we added constraint that cooling paths are preferred to pass through 10 ± 10ºC from 250 – 200 Ma (Table 2). Model results show slow burial starting in the Triassic. Burial and heating continued until ~90 Ma, possibly lasting until 60 – 50 Ma, followed by monotonic cooling to the present (Fig. 6E). We ran a similar model without sample 13DDT032, which was collected north of the Middle Kunlun fault zone, and found no major difference in the modeled cooling history.

For the Deshuiwai Basin and Middle Kunlun fault models, predicted apatite (U-Th)/He and apatite fission track mean ages are in general agreement with observed ages (Figs. 7E-F). Slow cooling rates since Cretaceous or early Eocene time is in agreement with field observations that the Yangqu and Babaoshan groups are flat-lying to mildly tilted but otherwise relatively undeformed in the Deshuiwai Basin (Figs. 4A and B). The degree of tilting and deformation of Mesozoic terrestrial strata increases near the Middle Kunlun fault, however the similarity in cooling histories on either side of the fault indicates that either deformation occurred before the mid-Cretaceous or that exhumation due to strike-slip faulting along the Middle Kunlun fault did not result in significant vertical exhumation.

## 5. $^{40}$Ar/$^{39}$Ar FAULT GOUGE DATING

Fault gouge, formed along fault surfaces during discrete events of fault slip as wall rock undergoes brittle deformation, contains clay-sized minerals that are well suited for age dating, such as potassium-bearing illite (van der Pluijm et al., 2001). Authigenically-grown illite (polytype $1M_d$) is a diagenetic product of tectonic activity and is a common target for fault gouge dating (van der Pluijm et al., 2001). Separation of pure authigenic illite from detrital illite (polytype $2M_1$) is not usually possible in fault gouge material because of the fine grain size of these clays and similar density and settling properties, and so authigenic and detrital illite ages are typically estimated from a two-end member mixing model derived from $^{40}Ar/^{39}Ar$ ages determined on mixtures with differing fractions of each polytype (van der Pluijm et al., 2001). The authigenic illite age is often interpreted to record the timing of faulting, whereas the detrital illite age corresponds to an inherited component reflecting the time of regional illite growth or the timing of metamorphism (van der Pluijm et al., 2001). Authigenic illite can, however, grow under a variety of conditions, such as during regional low-temperature metamorphism (Verdel et al., 2012), and thus interpretation of fault gouge ages requires careful consideration of independent records of regional tectonic and metamorphic history. Several recent analyses of combined thermochronologic and fault gouge dating highlight the potential power of using multiple independent chronometers to constrain the timing of upper crustal brittle deformation (Duvall et al., 2011; Staisch et al., 2016).

### *5.1. Sample collection and preparation*

We collected fault gouge samples from thrust and strike-slip faults throughout the Dongdatan Valley, East Wenquan Basin, and East Deshuiwai Mountains by identifying fault zones with clay rich gouge material. Because authigenic illite crystals tends to be smaller than detrital illite crystals (Grathoff and Moore, 1996), aliquots in which the relative proportion of each illite polytype varied were created by gravitational separation in a centrifuge. We measured each sample aliquot on a Scintag X1 Powder X-Ray Diffractometer (PXRD) at the University of Michigan Electron Microbeam Analysis Laboratory (EMAL). The relative abundance of detrital and authigenic illite was estimated by comparing standard $2M_1$ and $1M_d$ powder patterns to measured patterns. The error of polytype pattern matching is generally between 3 and 5 % (Haines and van der Pluijm, 2008), and we assume a ±4% error for the mixing fraction of each aliquot. Aliquots were analyzed for

$^{40}$Ar/$^{39}$Ar geochronology at the University of Michigan Argon Geochronology Laboratory. For illite age analysis, the total gas ages are used to determine the age of the illite polytype mixtures present in each aliquot. We assumed an uncertainty in of 3% for the $^{40}$Ar/$^{39}$Ar age of each aliquot in order to account for external errors (Renne et al., 1998; Karner and Renne, 1998; Dazé et al., 2003).

Possible natural loss of $^{40}$Ar was assessed by examining the fraction of $^{39}$Ar recoil during irradiation for each sample aliquot (f-recoil; Table 3), which is a proxy for illite crystallinity (Dong et al., 1995). Finally, the authigenic and detrital ages are estimated using the same Bayesian linear regression method employed by Staisch et al. (2016), in which the error in polytype concentration and geochronologic age are propagated into the uncertainty of the extrapolated end-member ages (Fig. 6). The modeled linear regression with the highest likelihood of fitting the observed data was deemed the best-fit line, from which we calculated the estimated authigenic and detrital illite ages for each sample. We report errors in slope and intercept values at the 2σ level. An expanded description of fault gouge illite age analysis methodology is in Supplementary text S1.

### *5.2. $^{40}$Ar/$^{39}$Ar fault gouge dating results*

The XRD powder patterns and modeled illite mixtures for each aliquot are available in Figures S4 – S7, $^{40}$Ar/$^{39}$Ar age spectra are plotted in Figures S8 – S11, and Ar release data is available in Table S4. The simplified results for each sample aliquot are in Table 3 and plotted in Fig. 8. In the following sections, we discuss the results and interpretations of the fault gouge geochronologic data.

#### *5.2.1. Thrust fault gouge ages*

The two fault gouge samples from thrust faults (11UMT55 and 12DDT18) were collected from similar structural settings in which Triassic metapelites are thrust over the Jurassic - Cretaceous Yangqu Group along the Wenquan Hu thrust fault (Fig. 2A). Under the assumption that authigenically-grown illite is younger than the formation age of detrital illite within the surrounding wall rock, and given that that authigenic illite grains tend to be are smaller than detrital grains, we expect younger $^{40}Ar/^{39}Ar$ ages in smaller size fraction aliquots (van der Pluijm et al., 2001). However, in both thrust fault gouge samples collected from Dongdatan Valley, we do not see a well-defined relationship between the aliquot ages and authigenic illite proportions. Samples 11UMT55 and 12DDT18 display a linear age-illite polytype fraction relationship in the three finest size fractions measured, but the coarsest size fraction in both samples deviates from this trend and is younger than the next coarsest size fraction (Fig. 8; Table 3). In both samples, we see an increase in f-recoil measured in the coarsest size fraction compared to the next largest size fraction, which likely corresponds to a decrease in illite crystallinity (Fig. S12; Table 3; Text S1). On this basis we suggest that apparent total gas ages measured for the coarse size fractions are erroneously young. Thus, we omit the coarsest size fraction for both thrust fault gouge samples and analyze the remaining three finest size fractions to determine an age of authigenic illite growth (Fig. 8). The Bayesian linear regression for sample 11UMT55 produces an authigenic illite age of 46.6 ± 4.0 Ma, a detrital illite age of 124.5 ± 11.3 Ma, and an $R^2$ value of 0.99 (Fig. 8A). Using a similar regression scheme, sample 12DDT18 produces a fault gouge age of 112.5 ± 5.8 Ma, a detrital illite age of 273.1 ± 27.4 Ma, and an $R^2$ of 0.99 (Fig. 8B).

*5.2.2. Strike-slip faults*

Samples 11UMT50 and 11UMT52 were collected from recently or currently active strike-slip faults located to the north and south of the Dongdatan Valley, respectively. Only sample 11UMT50 provides an interpretable age-illite concentration pattern. Sample 11UMT52 has a non-linear relationship between illite concentration and $^{40}Ar/^{39}Ar$ age and the deviation from the expected linear trend cannot be explained by the measured f-recoil. We therefore suggest that the

$^{40}Ar/^{39}Ar$ age data from sample 11UMT52 cannot be interpreted using a two end-member mixing model. Fault gouge ages from sample 11UMT50 do show a correlation between $^{40}Ar/^{39}Ar$ age and detrital illite component. The Bayesian linear regression through this fault gouge data suggests that the authigenic illite component was formed at 90.4 ± 4.7 Ma and that the detrital illite has an age of 177.0 ± 16.4 Ma. The best-fit regression has an $R^2$ value of 0.95 (Fig. 8C).

## 6. DISCUSSION

In this work, the thermochronologic and geochronologic data presented from the central East Kunlun Shan, along the northern margin of the Tibetan Plateau, record the timing, rate, and magnitude of upper crustal exhumation and fault activity over the past several tens of millions of years. In concert with detailed geologic mapping that characterizes the structural position of these thermochronologic samples, we can resolve the timing of major changes in structural style, and thus potentially stress orientation, throughout the Cenozoic evolution of the Tibetan Plateau. The structural evolution and shift in stress accommodation is a promising avenue for understanding the attainment of high elevation throughout the orogen, and complimentary to more paleoaltimetric data. Thus, we will interpret thermochronologic and structural data in light of several fundamental tectonic questions with respect to the northern plateau margin, specifically, and the evolution of high topography throughout the Tibet Plateau, more generally.

In the following section, we constrain the deformation history of the East Kunlun Shan by exploring the structural and exhumation histories from (1) regions that have evidence for Cenozoic thrust faulting but have not been subject to significant cooling following the onset of major lateral shear as well as (2) regions that appear to be dominated by recent strike-slip fault deformation and exhumation. We then integrate this tectonic history into a broader perspective of the evolution of the Tibetan Plateau and discuss how changes in structural style along the northern plateau margin may reflect the evolution of stress state of the Tibetan Plateau, as a proxy for the attainment of high elevation and gravitational potential energy. Furthermore, the spatiotemporal details of structural changes may provide insight into the geodynamic mechanisms responsible for elevation gain.

### *6.1. The timing of crustal shortening*

The East Wenquan Basin was formed in part as an extensional step over between the Xidatan and Middle Kunlun faults and forms a topographic low in the central East Kunlun Shan (Fig. 1). As a region of strike-slip fault related subsidence, it is more likely to preserve an older record of thrust-fault related exhumation and cooling, such as along the Wenquan Hu thrust fault (Figs. 2 and 3). QTQt modeling of the Wenquan Hu thrust fault hanging wall shows slow cooling over the majority of the Mesozoic followed by an increase in exhumation as early as 50 – 65 Ma, coincident with burial in the footwall (Figs. 6B-C). The similarity of apatite fission track ages and post-43 Ma cooling rates on either side of the Wenquan Hu thrust fault suggests that motion along this structure had ceased by 43 Ma and that the hanging wall and footwall blocks were subsequently exhumed together (Figs. 6B-C). We interpret thermochronologic data and models to indicate a period of crustal shortening along the Wenquan Hu thrust fault between Paleocene and early Eocene time (Fig. 9C). Post-43 Ma cooling rates may be due to a combination of regional uplift along other tectonic structures, discussed below, and surface processes.

Illite age analyses of fault gouge collected from the Wenquan Hu thrust fault yield authigenic illite ages of 47 Ma and 113 Ma from two different samples collected along strike (Fig. 8A-B). The Eocene fault gouge age determined for the westernmost sample overlaps with the timing of crustal shortening inferred from our thermochronologic modeling. The Cretaceous age for the easternmost fault gouge sample, on the other hand, coincides with a time of slow to negligible cooling in the hanging wall (Fig. 6B). We suggest that the 113 Ma authigenic illite age from the easternmost sample is an inherited age from either $^{40}Ar$ loss during Cretaceous low-grade metamorphism, which can produce a similar age-size fraction relationship as expected for fault-related authigenic illite growth (Verdel et al., 2012), or from an earlier phase of shear deformation as inferred from $^{40}Ar/^{39}Ar$ dating of nearby shear zones (Arnaud et al., 2003). The inherited age indicates that the site of our eastern fault gouge sample may not have been suitable for authigenic illite growth during Eocene thrust faulting along the Wenquan Hu thrust fault, possibly due to a lack of circulating hot fluids or other environmental parameters that stimulate authigenic illite growth.

While our thermochronologic modeling suggests that shortening accommodated on the Wenquan Hu thrust fault ceased by 43 Ma, previous studies show that crustal shortening and resultant exhumation continued elsewhere in the central East Kunlun Shan into late Eocene time, and possibly into late Oligocene time (Fig. 9C). For example, thermochronologic data and modeling in the East Kunlun Shan shows initial rapid exhumation as early as 40 – 41 Ma (Mock et al., 1999; Wang et al., 2017; Shi et al., 2018), and modeling of apatite (U-Th)/He ages from the southern margin of the Qaidam Basin show unroofing initiating around 35 Ma (Clark et al., 2010). Clark et al. (2010) suggest that shortening and exhumation continued along the Kunlun-Qaidam Basin margin due to motion along the South Qaidam fault until at least 24 Ma. Exhumation along the South Qaidam fault may have caused uplift and cooling in our study area and may thus be a component of Eocene – early Miocene cooling modeled across the Wenquan Hu thrust fault and in the East Deshuiwai Basin (Fig. 6). Taken together, these data from northern Tibet suggest that shortening initiated in Paleocene to early Eocene time in the south-central East Kunlun Shan such that the modern northern margin was established early in the Indo-Asian collision history and that shortening-related exhumation continued farther north along Kunlun-Qaidam Basin margin into the middle Miocene (Yin et al., 2002; Clark et al., 2010; Duvall et al., 2011).

***6.2. The onset of left-lateral shear***

In the western Dongdatan Valley, thermochronologic ages from a Triassic gneiss collected within 1 km of the Xidatan fault yield ~19 Ma cooling ages from both apatite (U-Th)/He and fission track methods (Fig. 2A). According to experimental and field studies of transpressional environments, exhumation due to strike-slip faulting is commonly of high magnitude and highly localized near the fault trace (Wilcox et al., 1973; Spotila et al., 2001; Niemi et al., 2014; Malusà and Fitzgerald, 2019). Thermal modeling of our data indicates rapid cooling between 20.0 and 21.6 ºC $Myr^{-1}$ in the interval between 23 and 17 Ma (Fig. 6A). Near the Kunlun Pass, thermochronologic ages collected along the Kunlun fault are similarly young, with AHe ages between 8 and 17 Ma and ZHe ages between 8 and 29 Ma (Fig. 1; Duvall et al., 2013). Importantly, the Miocene episode of rapid cooling is only captured in thermochronologic datasets collected near the Kunlun and Xidatan faults and is not apparent in datasets collected distal from strike-slip faulting. Thus, we interpret Miocene rapid cooling to be caused by localized exhumation along strike-slip faults.

Thermochronologic data from the East Deshuiwai Mountains, a restraining bend along the Xidatan fault zone (Fig. 1), suggest post-early Miocene exhumation related to strike-slip faulting. While thermal modeling results from samples 13DDT008 and 13DDT009 is not able to clearly determine the cooling histories recorded in either sample (Figs. 6D and 7D), apatite (U-Th)/He data show a strong correlation between measured age and crystal sizes (Fig. S2). A similar relationship has been recognized in the Big Horn Mountains in the United States and has been shown to suggest exhumation of a partial retention zone and that the youngest age can be used as a maximum time prior to exhumation (Reiners and Farley, 2001). Thus, we suggest that these rocks were isothermally held for upwards of 100 Myr, and that cooling increased after ~16 Ma, the youngest age measured in these samples, due to transpressional shear. Prolonged isothermal holding is in agreement with thermochronologic modeling of Clark et al. (2010) and our QTQt modeling throughout the region (Fig. 6). However, this interpretation is based on a single crystal age and we stress that this model should be considered with caution. Taken together, our thermochronologic data and thermal modeling from the Dongdatan Valley and East Deshuiwai Mountains suggest that strike-slip faulting initiated as early as 23 Ma and that transpression-related exhumation is highly localized near the trace of the Xidatan fault and within restraining bends.

Illite age analysis of fault gouge collected from a shear zone north of the Dongdatan Valley does not record Miocene strike-slip fault activity, but rather a mid-Cretaceous authigenic illite age. The absence of young illite age populations may suggest that the environment along sampled strike-slip faults is not conducive to authigenic illite growth or that there has been insufficient transpressional exhumation such that any Miocene or younger authigenic illite produced at depth has not been brought to the surface. The Cretaceous authigenic illite age may be remnant from low-grade metamorphism and $^{40}$Ar loss in nature (Verdel et al., 2012) or an earlier phase of mid-Cretaceous deformation (Arnaud et al., 2003). Regardless of genesis, fault gouge ages from material sampled along strike-slip faults in our field area do not provide meaning for data to constraining the onset of lateral shear in the East Kunlun Shan.

Based on thermochronologic ages and structural observations from the Dongdatan Valley and East Deshuiwai Mountains, we suggest that left-lateral faulting within the East Kunlun Shan initiated by 20 Ma and possibly as early as 23 Ma. This is in agreement with an increase in the cooling rate between 20 – 15 Ma inferred from thermochronologic data farther to the west along the Kunlun fault (Duvall et al., 2013). Thermochronologic data from Duvall et al. (2013) may also record an earlier phase of cooling that initiated between 30 and 25 Ma and continued until 20 – 15 Ma. This period overlaps with the period of inferred crustal shortening (Clark et al., 2010) as well as our inferred onset of strike-slip faulting by 23 – 20 Ma in the East Kunlun Shan. Model results from Duvall et al. (2013) are constrained by apatite and zircon (U-Th)/He ages that are similar to our ages collected near the Xidatan fault, however our inclusion of apatite fission-track data allow our model to define a discrete 23 – 20 Ma interval of cooling along the Xidatan fault. Thus, we suggest that Duvall et al. (2013) age results are produced from the same period of transpression along the Kunlun fault, but that their lack of AFT age constraints lead to a more broadly defined period of cooling.

### *6.3. Deformation history throughout the Tibetan Plateau and implications for surface uplift*

A main goal of this study was to constrain the timing of the transition in mode of deformation, from shortening to shear, in the central East Kunlun Shan and to relate this transition to broader geodynamic implications for the evolution of the Tibetan Plateau. We integrate our new structural, thermochronologic, and geochronologic datasets with previous work from throughout Tibet to obtain a spatial and temporal framework for the kinematic and topographic evolution of the orogen.

#### *6.3.1. Early Cenozoic crustal shortening*

Prior to the Indo-Asian collision, the northern Tibetan Plateau was a major depocenter for material eroded from an Andean-type margin, which stretched from the Gangdese batholith in the south to the Tanggula Shan in the north (Staisch et al., 2014; McRivette et al., 2019). During or soon after the ~50 – 60 Ma Indo-Asian collision, it has been inferred that crustal shortening stepped north of the Tanggula Shan to the modern northern plateau margin at the southern edge of the Qaidam Basin (Rowley, 1996; Yin et al., 2002; 2008; Molnar and Stock, 2009; Clark et al., 2010; Dupont-Nivet et al., 2010; Najman et al., 2010; Duvall et al., 2011; 2013; Staisch et al., 2016). Our new mapping, thermochronologic modeling, and fault gouge dating in the East Kunlun Shan are consistent with the inference of northward stepping of the plateau margin near the time of collision.

Strong lithospheric blocks to the north of the East Kunlun Shan focused plateau growth to the south of the Qaidam Basin, thus the majority of crustal shortening in northern Tibet from 50 – 35 Ma occurred between the Tanggula Shan and the Kunlun Shan (Fig. 10a; Burg et al., 1983; England and Searle, 1986; Murphy et al., 1997; Kapp et al., 2005, 2007a, 2007b; DeCelles et al., 2007a; Yin et al., 2008; Clark et al., 2010; Duvall et al., 2011; Hetzel et al., 2011; Clark, 2012; Rohrmann et al., 2012; Ding et al., 2014; Lin et al., 2020). DeCelles et al. (2010) postulate that the Greater Indian lithosphere underthrust the Lhasa terrane early in the collision history, which may explain the propagation of crustal shortening north of the Tanggula Shan after the Indo-Asian collision, as well as a northward sweep in volcanism into the Qiangtang terrane (Fig. 10a; Ding et al., 2003, 2007; Kapp et al., 2003, 2005; Lee et al., 2009; Li et al., 2006; Miller et al., 1999, 2000; Nomade et al., 2004; Williams et al., 2001, 2004; Zhao et al., 2009; Yakovlev et al., 2019; Lin et al., 2020).

High elevation may have been attained in the central Tibetan Plateau by Eocene – Oligocene time (DeCelles et al., 2007a; 2007b; Polissar et al., 2009; Ding et al., 2014), however low to moderate elevation persisted in the intervening Hoh Xil Basin from late Oligocene to early Miocene time (Pollisar et al., 2009; Sun et al., 2015), as well as in the Kailas Basin of southern Tibet (DeCelles et al., 2010), suggesting that crustal shortening alone did not produce high elevation throughout the Tibetan Plateau (Staisch et al., 2016). In the Lhasa and Qiangtang terranes, the temporal coincidence of late Oligocene to early Miocene arc-parallel extension in southern Tibet and a southward sweep of volcanism from the Qiangtang to the Lhasa terranes has been interpreted to result from slab rollback beneath Tibet (Figs. 10b and 10c; DeCelles et al., 2010; Yakovlev et al., 2019). This geodynamic model also provides a mechanism for the coeval cessation of deformation in northern Tibet, in that slab rollback would potentially relieve northern Tibet of its deep-seated southern buttress and lead to an eventual change in stress orientations throughout the plateau (Fig. 10c).

*6.3.2. Miocene plateau-wide change in faulting style*

Abundant evidence suggests that the Tibetan Plateau underwent a significant reorganization of faulting style following the late Oligocene – early Miocene cessation of crustal shortening in the northern Tibetan Plateau (Figs. 10d and 10e). For example, the Kunlun and Altyn Tagh are major strike-slip faults that dominate the deformation field of northern Tibet. Pre-Miocene piercing points along the Altyn Tagh fault show a common magnitude of offset, indicating that the inception of strike-slip likely occurred in late Oligocene – early Miocene time (Yue et al., 2001; 2003; Yin et al., 2002; Ritts et al., 2008). This overlaps with our interpretation of new thermochronologic data, which suggest that left-lateral motion along the Kunlun fault initiated as early as 23 Ma and may have propagated to the east and west by ~16 – 8 Ma (Fig. 11; Jolivet et al., 2003; Duvall et al., 2013).

In addition to the Kunlun and Altyn Tagh faults in northern Tibet, strike-slip faults throughout in the Tibetan Plateau initiated in the Miocene. In the Qilian Shan, left-lateral motion along the Haiyuan fault initiated slightly after Kunlun fault activity, ca. 17 Ma (Duvall et al., 2013). In the eastern Qilian Shan, thermochronologic data, along with sediment accumulation rates, provenance and stable isotope records, indicate that north-south shortening ceased by 20 Ma and transitioned to eastward-directed plateau expansion by ca. 13 Ma (Hough et al., 2011; Lease et al., 2011; 2012; Wang et al., 2012). Within central and southern Tibet, strike-slip faulting initiated by ~18 – 13 Ma (Fig. 11; Armijo et al., 1986; 1989; Murphy et al., 2000; Lee et al., 2003; Phillips et al., 2004; Taylor et al., 2003; Taylor and Peltzer, 2006; Wang et al., 2009). Normal faults throughout the southern Tibetan Plateau also appear to initiate in early to middle Miocene time (Fig. 11; Blisniuk et al., 2001; Garzione et al., 2003; Murphy et al., 2002; Lee et al., 2011; Ratschbacher et al., 2011; McCallister et al., 2013; Sundell et al., 2013; Styron et al., 2013). The coeval onset of normal and strike-slip faulting may reflect a change in the stress state across the Tibetan Plateau.

*6.3.3. Geodynamic mechanisms responsible for elevation gain and a shift in stress accommodation*

Recent work has suggested that stress reorganization throughout the Tibetan Plateau may be due to a shift in middle Miocene related to changes in Pacific - Eurasia plate convergence (Zhuang et al., 2018). However, early Miocene onset of normal and strike-slip faulting throughout the Tibetan Plateau and its coincidence with records of uplift to high elevation throughout the plateau (Rowley and Currie, 2006; DeCelles et al., 2007a, 2007b; Wu et al., 2008; Polissar et al., 2009; Xu et al., 2013; Ding et al., 2014) and onset of eastward plateau expansion via lower crustal flow (Royden et al., 1997; Clark and Royden, 2000; Clark et al., 2005b; Ouimet et al., 2010) implies a regional mechanistic cause rather than one of distal plate reorganization. Furthermore, the onset of strike-slip faulting along the Kunlun and Altyn Tagh faults is ~5 – 8 Ma older than normal and strike-slip fault initiation in central and southern Tibet, which indicates that the mechanistic cause for stress reorganization was initially focused in the northern Tibetan Plateau.

The mechanism of Miocene elevation gain in northern Tibet is debated, however post-Oligocene crustal thickening of the Hoh Xil Basin, possibly via lower crustal flow, likely contributed to elevation gain in northern Tibet (Staisch et al., 2016). Additionally, widespread post-30 Ma magmatism in the Hoh Xil Basin may be suggestive of mantle root loss, which could result in relatively rapid uplift of 1 – 3 km (England and Houseman, 1989; McKenna and Walker, 1990;

Molnar et al., 1993; Ding et al., 2003; Lai et al., 2003; Williams et al., 2004; Chung et al., 2005; Wang et al., 2005; Guo et al., 2006; Jiang et al., 2006; Molnar and Stock, 2009; Chen et al., 2012; Yakovlev et al., 2019). We propose that the late Oligocene to early Miocene period of slab rollback may have primed the northern Tibetan mantle lithosphere for delamination and foundering in the Miocene (Fig. 10c and 10d). We do not exclude lower crustal flow as a separate mechanism for post-Oligocene surface uplift possible as they are not mutually exclusive (Staisch et al., 2016) and are both supported by petrologic and geophysical data (Arnaud et al., 1992; Turner et al., 1993, 1996; Owens and Zandt, 1997; Ding et al., 2003; McKenna and Williams et al., 2004; Guo et al., 2006, 2014; Klemperer, 2006; Jiang et al., 2008; Karplus et al., 2011; Wang et al., 2012; Yang and Ding, 2013; Jiang et al., 2014). Regardless of the mechanism, an increase in elevation in northern Tibet would affect the average of force per unit length throughout the orogen (Molar and Stock, 2009), indicating that uplift need not occur simultaneously or of equal magnitude to produce a plateau-wide shift in gravitational potential energy. Given the temporal coincidence in elevation gain in northern Tibet and the shift in stress accommodation throughout the Tibetan Plateau between 23 – 16 Ma, we suggest that uplift to high elevation in northern Tibet resulted in the increase in average gravitational potential energy across the orogen and the plateau-wide inception of strike-slip and normal faulting activity within ~5 – 8 Ma of onset (Fig. 10d and 10e).

## 7. CONCLUSIONS

Our data from the central East Kunlun Shan provide new constraints on the deformation history of the northern Tibetan Plateau margin. Results from thermochronologic ages and modeling, $^{40}Ar/^{39}Ar$ fault gouge dating, and structural mapping suggest that north-south oriented crustal shortening initiated between 65 and 50 Ma and ceased within the Dongdatan Valley by 43 Ma.

Previous data collected elsewhere in the central East Kunlun Shan broaden the timing of crustal shortening into late Oligocene time (Mock et al., 1999; Clark et al., 2010). Our thermochronologic modeling results suggest a 23 – 20 Ma phase of rapid cooling near the Xidatan segment of the Kunlun fault zone. We interpret the increased cooling rate to result from highly localized uplift along transpressional sections of the Kunlun fault. We suggest these ages to represent the onset of strike-slip faulting in the central East Kunlun Shan, as they are slightly older but consistent with previous work on the timing of sinistral shear in the Kunlun Shan (Jolivet et al., 2003; Duvall et al., 2013).

The early to middle Miocene kinematic shift from north-south oriented pure shear to east-west oriented simple shear throughout the orogen was likely driven by an increase in gravitational potential energy. One potential mechanism for increasing gravitational potential energy and reorganizing crustal scale stress is the development of high topography in the northern Tibetan Plateau. Given the absence of shortening in northern Tibet after late Oligocene to early Miocene time (Staisch et al., 2016), elevation gain and increase in gravitational potential energy was likely due to lower crustal thickening or mantle lithospheric thinning. The roughly coeval onset of strike-slip and normal fault activity throughout the Tibetan Plateau (Blisniuk et al., 2001; Murphy et al., 2000; Murphy et al., 2002; Garzione et al., 2003; Lee et al., 2003; Phillips et al., 2004; Taylor and Peltzer, 2006; Wang et al., 2009; Lee et al., 2011; Ratschbacher et al., 2011; McCallister et al., 2013; Sundell et al., 2013; Styron et al., 2013) and eastward plateau expansion via lower crustal flow (Clark and Royden, 2000; Clark et al., 2005A; Clark et al., 2005b) suggest that peak elevations may have been reached by middle Miocene time.

**ACKNOWLEDGEMENTS**

This work was funded through NSF Continental Dynamics grants EAR-0908711 and EAR-1211434 to Niemi and Clark, an NSF Graduate Research Fellowship awarded to Staisch, a GSA Graduate Student Research Award to Staisch, and two University of Michigan Turner Grants awarded to Staisch. We acknowledge NFSC grant 40921120406 to An Zhisheng, which supported our Chinese colleagues at the Institute for Earth Environment and our joint fieldwork in the Tibetan Plateau. We thank Peter Molnar for his efforts in leading our NSF Continental Dynamics group. Petr Yakovlev, Jiang Yi, and Zhang Peng provided considerable assistance in the field. Special thanks to Amanda Maslyn for assistance in apatite and zircon separation, to Stuart Thomson and Eva Enkelmann for fission track analysis, to Jim Metcalf for U, Th, and Sm measurement, to Chris Hall for $^{40}Ar/^{39}Ar$ analyses. We thank Richard Lease, Jingen Dai and an anonymous reviewer for their constructive reviews of this manuscript. All data and supplementary data are catalogued and publicly available at the USGS ScienceBase repository (https://doi.org/10.5066/P9F3DZYQ).

## REFERENCES

Arnaud, N.O., P. Vidal, P. Tapponnier, P. Matte, and W. M. Deng, 1992, The high K2O volcanism of northwestern Tibet: Geochemistry and tectonic implications, Earth Planet. Sci. Lett., 111, 351–367, doi:10.1016/0012-821X(92)90189-3.

Arnaud, N.O., Tapponnier, P., Roger, F., Brunel, M., Scharer, U., Wen, C., and Zhiqin, X., 2003, Evidence for Mesozoic shear along the western Kunlun and Altyn-Tagh fault, northern Tibet (China):, J. Geophys. Res., v. 108, doi:10.1029/2001JB000904, B1.

Armijo, R., Tapponnier, P., and Han, T. L., 1989, Late Cenozoic Faulting in Southern Tibet: Journal of Geophysical Research, v. 94, p. 2787-2838.

Armijo, R., Tapponnier, P., Mercier, J.L., and Tonglin, H., 1986, Quaternary extension in southern Tibet: field observations and tectonic implications: Journal of Geophysical Research, v. 91, p. 13,803–13,872.

Avouac, J.-P., and Tapponnier, P., 1993, Kinematic model of active deformation in central Asia: Geophysical Research Letters, v. 20, p. 895–898.

Benowitz, J.A., Layer, P.W., Armstrong, P., Perry, S.E., Haeussler, P.J., Fitzgerald, P.G., and Van Laningham, S., 2011, Spatial variations in focused exhumation along a continental-scale strike-slip fault: The Denali fault of the eastern Alaska Range: Geosphere, v. 7, p. 455-467, doi:10.1130/GES00589.1

Biddle, K. T., and N. Christie-Blick (Eds), 1985, Strike-Slip Deformation, Basin Formation, and Sedimentation: Spec. Publ. Soc. Econ. Paleontol. Mineral., v. 37, p. 356.

Bilham, R., and G. King, 1989, The morphology of strike-slip faults—Examples from the San Andreas Fault, California: J. Geophys. Res., v. 94, p. 10,204–10,216.

Blisniuk, P.M., Hacker, B.R., Glodny, J., Ratschbacher, L., Bi, S., Wu, Z., McWilliams, M.O., Calvert, A., and Geowissenschaften, È., 2001, Normal faulting in central Tibet since at least 13.5 Myr ago: Nature, v. 412, p. 628–632.

Braun, J., 2005, Quantitative Constraints on the Rate of Landform Evolution Derived from Low-Temperature Thermochronology: Reviews in Mineralogy and Geochemistry, v. 58, p. 351–374, doi: 10.2138/rmg.2005.58.13.

Burg, J.P., Proust, F., Tapponnier, P., and Chen, G.M., 1983, Deformation phases and tectonic evolution of the Lhasa block: Eclogae Geol. Helv, v. 76, p. 643–683.

Burke, K., and Sengor, C., 1986, Tectonic escape in the evolution of the continental crust: Reflection Seismology: The Continental Crust, v. 14, p. 41–53.

Chen, W., Zhang, Y., Ji, Q., Wang, S., & Zhang, J., 2002, Magmatism and deformation times of the Xidatan rock series, East Kunlun Mountains: Science in China Series B: Chemistry, v. 45, no. 1, p. 20-27.

Chen, J.-L., Xu, J.-F., Wang, B.-D., and Kang, Z.-Q., 2012, Cenozoic Mg-rich potassic rocks in the Tibetan Plateau: Geochemical variations, heterogeneity of subcontinental lithospheric mantle and tectonic implications: Journal of Asian Earth Sciences, v. 53, p. 115–130, doi: 10.1016/j.jseaes.2012.03.003.

Chinnery, M. A., 1965, The vertical displacements associated with transcurrent faulting: J. Geophys. Res., v. 70, doi:10.1029/JZ070;018p04627

Chung, S.-L., Chu, M.-F., Zhang, Y., Xie, Y., Lo, C.-H., Lee, T.-Y., Lan, C.-Y., Li, X., Zhang, Q., and Wang, Y., 2005, Tibetan tectonic evolution inferred from spatial and temporal variations in post-collisional magmatism: Earth-Science Reviews, v. 68, p. 173–196, doi: 10.1016/j.earscirev.2004.05.001.

Clark, M.K., and Royden, L.H., 2000, Topographic ooze : Building the eastern margin of Tibet by lower crustal flow: Geology, v. 28, no. 8, p. 703–706.

Clark, M.K., Bush, J.W.M., and Royden, L.H., 2005a, Dynamic topography produced by lower crustal flow against rheological strength heterogeneities bordering the Tibetan Plateau: Geophysical Journal International, v. 162, no. 2, p. 575–590, doi: 10.1111/j.1365-246X.2005.02580.x.

Clark, M.K., House, M.A., Royden, L.H., Whipple, K., Burchfiel, B.C., Zhang, X., and Tang, W., 2005b, Late Cenozoic uplift of southeastern Tibet: Geology, v. 33, no. 6, p. 525–528, doi: 10.1130/G21265.1.

Clark, M.K., Farley, K.A., Zheng, D., Wang, Z., and Duvall, A.R., 2010, Early Cenozoic faulting of the northern Tibetan Plateau margin from apatite (U–Th)/He ages: Earth and Planetary Science Letters, v. 296, p. 78–88, doi: 10.1016/j.epsl.2010.04.051.

Clark, M.K., 2012, Continental collision slowing due to viscous mantle lithosphere rather than topography: Nature, v. 483, p. 74–7, doi: 10.1038/nature10848.

Crowell, J. C., 1974, Origin of late Cenozoic basins in southern California, in tectonics and sedimentation: Soc. Econ. Paleontologists and Mineralogists Spec. Pub. 22, p. 190–204.

Dai, J., X. Zhao, C. Wang, L. Zhu, Y. Li, and D. Finn (2012), The vast proto-Tibetan Plateau: New constraints from Paleogene Hoh Xil Basin, Gondwana Res.: v. 22, no. 2, p. 434–446, doi:10.1016/j.gr.2011.08.019.

Dai, J., C. Wang, J. Hourigan, M. Santosh (2013), Multi-stage tectono-magmatic events of the Eastern Kunlun Range, northern Tibet: Insights from U-Pb geochronology and (U-Th)/He thermochronology, Tectonophysics: v. 599, p. 97-106

Dazé, A., Lee, J.K.., and Villeneuve, M., 2003, An intercalibration study of the Fish Canyon sanidine and biotite 40Ar/39Ar standards and some comments on the age of the Fish Canyon Tuff: Chemical Geology, v. 199, p. 111–127, doi: 10.1016/S0009-2541(03)00079-2.

DeCelles, P.G., Quade, J., Kapp, P., Fan, M., Dettman, D.L., and Ding, L., 2007a, High and dry in central Tibet during the Late Oligocene: Earth and Planetary Science Letters, v. 253, no. 3-4, p. 389–401, doi: 10.1016/j.epsl.2006.11.001.

DeCelles, P.G., Kapp, P., Ding, L., and Gehrels, G.E., 2007b, Late Cretaceous to middle Tertiary basin evolution in the central Tibetan Plateau: Changing environments in response to tectonic partitioning, aridification, and regional elevation gain: Geological Society of America Bulletin, v. 119, no. 5-6, p. 654–680, doi: 10.1130/B26074.1.

Ding, L., Kapp, P., Zhong, D., Deng, W., 2003, Cenozoic Volcanism in Tibet: Evidence for a Transition from Oceanic to Continental Subduction: Journal of Petrology, v. 44, p. 1833–1865.

Ding, L., Xu, Q., Yue, Y., Wang, H., Cai, F., and Li, S., 2014, The Andean-type Gangdese Mountains: Paleoelevation record from the Paleocene–Eocene Linzhou Basin: Earth and Planetary Science Letters, v. 392, p. 250–264, doi: 10.1016/j.epsl.2014.01.045.

Dodson, M.H., 1973, Closure Temperature in Cooling Geochronological and Petrological Systems: Contr. Mineral. and Petrol., v. 40, p. 259–274.

Dong, H., Hall, C.M., Peacor, D.R., and Halliday, A.N., 1995, Mechanisms of argon retention in clays revealed by laster 40Ar/39Ar dating: Science, v. 267, p. 355–359.

Duan, Z., Li, Y., Shen, Z., Zhu, X., and Zhong, C., 2007, Analysis of the evolution of the Cenozoic ecological environment and process of plateau surface uplift in the Wenquan area in the interior of the Qinghai-Tibet Plateau: Geology in China, v. 34, no. 4, p. 688 – 696.

Duan, Q., Zhang, K., Wang, J., Yao, H., and Niu, Z., 2008, Oligocene Palynoflora, Paleovegetation and Paleoclimate in the Tanggula Mountains, northern Tibet: Acta Micropalaeontologica Sinica, v. 25, no. 2, p. 185–195

Dupont-Nivet, G., P. C. Lippert, D. J. van Hinsbergen, M. J. Meijers, and P. Kapp (2010), Palaeolatitude and age of the Indo–Asia collision: Palaeomagnetic constraints, Geophys. J. Int., 182(3), 1189–1198.

Duvall, A.R., and Clark, M.K., 2010, Dissipation of fast strike-slip faulting within and beyond northeastern Tibet: Geology, v. 38, p. 223–226, doi: 10.1130/G30711.1.

Duvall, A.R., Clark, M.K., van der Pluijm, B. a., and Li, C., 2011, Direct dating of Eocene reverse faulting in northeastern Tibet using Ar-dating of fault clays and low-temperature thermochronometry: Earth and Planetary Science Letters, v. 304, p. 520–526, doi: 10.1016/j.epsl.2011.02.028.

Duvall, A.R., Clark, M.K., Kirby, E., Farley, K.A., Craddock, W.H., Li, C., and Yuan, D.-Y., 2013, Low-temperature thermochronometry along the Kunlun and Haiyuan Faults, NE Tibetan Plateau: Evidence for kinematic change during late-stage orogenesis: Tectonics, v. 32, p. 1190–1211, doi: 10.1002/tect.20072.

Ehlers, T.A., 2005, Crustal Thermal Processes and the Interpretation of Thermochronometer Data: Reviews in Mineralogy and Geochemistry, v. 58, p. 315–350, doi: 10.2138/rmg.2005.58.12.

Ehlers, T.A., and Farley, K.A., 2003, Apatite (U-Th)/He thermochronometry : methods and applications to problems in tectonic and surface processes: Earth and Planetary Science Letters, v. 206, p. 1–14.

England, P., and Houseman, G., 1989, Extension During Continental Convergence, With Application to the Tibetan Plateau: Journal of Geophysical Research, v. 94, no. B12, p. 17,561–17,579.

England, P., and Searle, M., 1986, The Cretaceous-tertiary deformation of the Lhasa Block and its implications for crustal thickening in Tibet: Tectonics, v. 5, p. 1–14.

Farley, K.A., 2000, Helium diffusion from apatite: General behavior as illustrated by Durango fluorapatite: Journal of Geophysical Research, v. 105, p. 2903–2914.

Farley, K.A., and Stockli, D.F., 2002, (U-Th)/He Dating of Phosphates: Apatite, Monazite, and Xenotime: Reviews in Mineralogy and Geochemistry, v. 48, p. 559–577, doi: 10.2138/rmg.2002.48.15.

Flowers, R.M., Ketcham, R. a., Shuster, D.L., and Farley, K. a., 2009, Apatite (U–Th)/He thermochronometry using a radiation damage accumulation and annealing model: Geochimica et Cosmochimica Acta, v. 73, p. 2347–2365, doi: 10.1016/j.gca.2009.01.015.

Fu, B., and Awata, Y., 2007, Displacement and timing of left-lateral faulting in the Kunlun Fault Zone, northern Tibet, inferred from geologic and geomorphic features: Journal of Asian Earth Sciences, v. 29, p. 253–265, doi: 10.1016/j.jseaes.2006.03.004.

Fu, B.H., Walker, R., Sandiford, M., 2011, The 2008 Wenchuan earthquake and active tectonics of Asia: Journal of Asian Earth Sciences, v. 40, p. 797-804.

Gallagher, K., 2012, Transdimensional inverse thermal history modeling for quantitative thermochronology. Journal of Geophysical Research: Solid Earth, v. 117(B2), p. 1–16.

Garzione, C.N., DeCelles, P.G., Hodkinson, D.G., Ojha, T.P., and Upreti, B.N., 2003, East-west extension and Miocene environmental change in the southern Tibetan plateau: Thakkhola graben, central Nepal: Geological Society of America Bulletin, v. 115, p. 3–20, doi: 10.1130/0016-7606(2003)115<0003:EWEAME>2.0.CO;2.

Grubb, S.M.B., Peacor, D.R., and Jjang, W., 1991, Transmission electron microscope observations of illite polytypism: Clays and Clay Minerals, v. 39, p. 540–550.

Guo, Z., Wilson, M., Liu, J., and Mao, Q., 2006, Post-collisional, Potassic and Ultrapotassic Magmatism of the Northern Tibetan Plateau: Constraints on Characteristics of the Mantle Source, Geodynamic Setting and Uplift Mechanisms: Journal of Petrology, v. 47, p. 1177–1220, doi: 10.1093/petrology/egl007.

Guo, Z., M. Wilson, L. Zhang, M. Zhang, Z. Cheng, and J. Liu, 2014, The role of subduction channel mélanges and convergent subduction systems in the petrogenesis of post-collisional

K-rich mafic magmatism in NW Tibet, Lithos, 198–199, 184–201, doi:10.1016/j.lithos.2014.03.020.

Haines, S.H., and van der Pluijm, B.A., 2008, Clay quantification and Ar–Ar dating of synthetic and natural gouge: Application to the Miocene Sierra Mazatán detachment fault, Sonora, Mexico: Journal of Structural Geology, v. 30, no. 4, p. 525–538, doi: 10.1016/j.jsg.2007.11.012.

Hetzel, R., Dunkl, I., Haider, V., Strobl, M., Von Eynatten, H., Ding, L., and Frei, D., 2011, Peneplain formation in southern Tibet predates the India-Asia collision and plateau uplift: Geology, v. 39, no. 10, p. 983–986, doi: 10.1130/G32069.1.

Hough, B.G., Garzione, C.N., Wang, Z.C., Lease, R.O., Burbank, D.W., and Yuan, D.Y., 2011, Stable isotope evidence for topographic growth and basin segmentation: Implications for the evolution of the NE Tibetan plateau: Geological Society of America Bulletin, v. 123, p. 168–185, doi:10.1130/B30090.1.

Jiang, C., Y. Yang, and Y. Zheng, 2014, Penetration of mid-crustal low velocity zone across the Kunlun Fault in the NE Tibetan Plateau revealed by ambient noise tomography, Earth Planet. Sci. Lett., 406, 81–92, doi:10.1016/j.epsl.2014.08.040.

Jiang, D., J. Liu, and L. Ding, 2008, Geochemistry and petrogenesis of Cenozoic potassic volcanic rocks in the Hoh Xil area, northern Tibet plateau, Acta Petrol. Sin., 24, 279–290, CNKI:SUN:YSXB.0.2008-02-010.

Jiang, Y.-H., Jiang, S.-Y., Ling, H.-F., and Dai, B.-Z., 2006, Low-degree melting of a metasomatized lithospheric mantle for the origin of Cenozoic Yulong monzogranite-porphyry, east Tibet: Geochemical and Sr–Nd–Pb–Hf isotopic constraints: Earth and Planetary Science Letters, v. 241, p. 617–633, doi: 10.1016/j.epsl.2005.11.023.

Jolivet, M., Brunel, M., Seward, D., Xu, Z., Yang, J., Malavieille, J., Roger, F., Leyreloup, A., Arnaud, N., and Wu, C., 2003, Neogene extension and volcanism in the Kunlun Fault Zone, northern Tibet: New constraints on the age of the Kunlun Fault: Tectonics, v. 22, p. 1–23, doi: 10.1029/2002TC001428.

Kapp, P., DeCelles, P.G., Leier, A.L., Fabijanic, J.M., He, S., Pullen, A., and Gehrels, G.E., 2007a, The Gangdese retroarc thrust belt revealed: GSA Today, v. 17, p. 4–9.

Kapp, P., DeCelles, P.G., Gehrels, G.E., Heizler, M., and Ding, L., 2007b, Geological records of the Lhasa-Qiangtang and Indo-Asian collisions in the Nima area of central Tibet: Geological Society of America Bulletin, v. 119, p. 917–933, doi: 10.1130/B26033.1.

Kapp, P., Yin, A., Harrison, T.M., and Ding, L., 2005, Cretaceous-Tertiary shortening, basin development, and volcanism in central Tibet: Geological Society of America Bulletin, v. 117, p. 865–878, doi: 10.1130/B25595.1.

Karner, D.B., and Renne, P.R., 1998, 40Ar/39Ar geochronology of Roman volcanic province tephra in the Tiber River valley : Age calibration of middle Pleistocene sea-level changes: Geological Society of America Bulletin, v. 110, p. 740–747, doi: 10.1130/0016-7606(1998)110<0740.

Karplus, M. S., W. Zhao, S. L. Klemperer, Z. Wu, J. Mechie, D. Shi, L. D. Brown, and C. Chen, 2011, Injection of Tibetan crust beneath the south Qaidam Basin: Evidence from INDEPTH IV wide-angle seismic data, J. Geophys. Res., 116, B07301, 1–23, doi:10.1029/2010JB007911.

Ketcham, R.A., 2005, Forward and Inverse Modeling of Low-Temperature Thermochronometry Data: Reviews in Mineralogy and Geochemistry, v. 58, p. 275–314, doi: 10.2138/rmg.2005.58.11.

Ketcham, R.A., Carter, A., Donelick, R.A., Barbarand, J., and Hurford, A.J., 2007, Improved modeling of fission-track annealing in apatite: American Mineralogist, v. 92, p. 799–810, doi: 10.2138/am.2007.2281.

Kidd, W.S., and Molnar, P., 1988, Quaternary and active faulting observed on the 1985 Academia Sinica- Royal Society Geotraverse of Tibet: Philosophical Transactions of the Royal Society of London. Series A, Mathematical and Physical Sciences, v. 327, p. 337–363.

Kidd, W.S., Pan, Y., Chang, C., Coward, M.P., Dewey, J.F., Gansser, A., Molnar, P., Shackleton, R.M., and Yiyin, S., 1988, Geological mapping of the 1985 Chinese-British Tibetan (Xizang-Qinghai) Plateau Geotraverse route: Philosophical Transactions of the Royal Society of London. Series A, Mathematical and Physical Sciences, v. 327, p. 287–305.

Kirby, E., Harkins, N., Wang, E., Shi, X., Fan, C., and Burbank, D., 2007, Slip rate gradients along the eastern Kunlun fault: Tectonics, v. 26, TC2010, doi:10.1029/2006TC002033.

Klemperer, S. L., 2006, Crustal flow in Tibet: Geophysical evidence for the physical state of Tibetan lithosphere, and inferred patterns of active flow, Geol. Soc. London Spec. Publ., 268(1), 39–70, doi:10.1144/GSL.SP.2006.268.01.03.

Lai, S.-C., Liu, C.-Y., and Yi, H.-S., 2003, Geochemistry and Petrogenesis of Cenozoic Andesite-Dacite Associations from the Hoh Xil Region, Tibetan Plateau: International Geology Review, v. 45, p. 998–1019, doi: 10.2747/0020-6814.45.11.998.

Lease, R.O., Burbank, D.W., Clark, M.K., Farley, K.A., Zheng, D., and Zhang, H., 2011, Middle Miocene reorganization of deformation along the northeastern Tibetan Plateau: Geology, v. 39, p. 359–362, doi:10.1130/G31356.1.

Lease, R.O., Burbank, D.W., Hough, B., Wang, Z., and Yuan, D., 2012a, Pulsed Miocene range growth in northeastern Tibet: Insights from Xunhua Basin magnetostratigraphy and provenance: Geological Society of America Bulletin, v. 124, p. 657–677, doi:10.1130/B30524.1.

Lee, H.-Y., Chung, S.-L., Wang, J.-R., Wen, D.-J., Lo, C.-H., Yang, T.F., Zhang, Y., Xie, Y., Lee, T.-Y., Wu, G., and Ji, J., 2003, Miocene Jiali faulting and its implications for Tibetan tectonic evolution: Earth and Planetary Science Letters, v. 205, p. 185–194, doi: 10.1016/S0012-821X(02)01040-3.

Lee, J., Hager, C., Wallis, S.R., Stockli, D.F., Whitehouse, M.J., Aoya, M., and Wang, Y., 2011, Middle to late Miocene extremely rapid exhumation and thermal reequilibration in the Kung Co rift, southern Tibet: Tectonics, v. 30, doi: 10.1029/2010TC002745.

Li G.W., Sandiford, M., Fang, A.M., Kohn, B., Sandiford, D., Fu, B.H., Zhang, T.L., Cao, Y.Y., and Chen, F., 2019, Multi-stage exhumation history of the West Kunlun orogen and the amalgamation of the Tibetan Plateau: Earth and Planetary Science Letters, p.528, doi.org/10.1016/j.epsl.2019.115833

Li, H.B., Van der Woerd, J., Tapponnier, P., Klinger, Y., Qi, X.X, Yang, J.S., and Zhu, Y. T., 2005, Slip rate on the Kunlun fault at Hongshui Gou, and recurrence time of great events comparable to the 14/11/2001, Mw~ 7.9 Kokoxili earthquake: Earth and Planetary Science Letters, v. 237(1), p. 285-299.

Lin et al., 2020, Late Eocene-Oligocene High Relief Paleotopography in the North Central Tibetan Plateau: Insights From Detrital Zircon U-Pb Geochronology and Leaf Wax Hydrogen Isotope Studies

Liu, Y., Genser, J., Neubauer, F., Jin, W., Ge, X., Handler, R., Takasu, A., 2005, $^{40}$Ar/$^{39}$Ar mineral ages from basement rocks in the Eastern Kunlun Mountains, NW China, and their tectonic implications. *Tectonophysics*, v. *398*(3-4), p. 199-224.

Malusà, M.G. and Fitzgerald, P.G., 2019, Application of thermochronology to geologic problems: bedrock and detrital approaches: In Fission-Track Thermochronology and its Application to Geology, p. 191-209.

McCallister, A.T., Taylor, M.H., Murphy, M.A., Styron, R.H., & Stockli, D.F., 2013, Thermochronologic constraints on the late Cenozoic exhumation history of the Gurla Mandhata metamorphic core complex, Southwestern Tibet: Tectonics, v. 33, p. 27–52.

McKenna, L.W., and Walker, J.D., 1990, Geochemistry of Crustally Derived Leucocratic Igneous Rocks From the Ulugh Muztagh Area, Northern Tibet and Their Implications for the Formation of the Tibetan Plateau: Journal of Geophysical Research, v. 95, p. 21483 – 21502.

McRivette, M.W., Yin, A., Chen, X., Gehrels, G.E., 2019, Cenozoic basin evolution of the central Tibetan plateau as constrained by U-Pb detrital zircon geochronology, sandstone petrology, and fission-track thermochronology: Tectonophysics, v. 751, p. 150-179, doi: 10.1016/j.tecto.2018.12.015.

Mock, C., Arnaud, N.O., and Cantagrel, J., 1999, An early unroofing in northeastern Tibet ? Constraints from 40Ar/39Ar thermochronology on granitoids from the eastern Kunlun range: Earth and Planetary Science Letters, v. 171, p. 107–122.

Molnar, P., and Stock, J.M., 2009, Slowing of India's convergence with Eurasia since 20 Ma and its implications for Tibetan mantle dynamics: Tectonics, v. 28, p. 1–11, doi: 10.1029/2008TC002271.

Molnar, P., and Tapponnier, P., 1978. Active faulting in Tibet: J. Geophys. Res, v. 83, p. 5361-5375.

Molnar, P., England, P., and Martinod, J., 1993, Mantle dynamics, uplift of the Tibetan Plateau, and the Indian Monsoon: Reviews in Geophysics, v. 31, no. 4, p. 357–396.

Murphy, M.A., Yin, A., Harrison, T.M., Dürr, S.B., Z, C., Ryerson, F.J., Kidd, W.S.F., X, W., and X, Z., 1997, Did the Indo-Asian collision alone create the Tibetan plateau?: Geology, v. 25, p. 719–722, doi: 10.1130/0091-7613(1997)025<0719:DTIACA>2.3.CO;2.

Murphy, M.A., Yin, A., Kapp, P., Harrison, T.M., Ding, L., and Jinghui, G., 2000, Southward propagation of the Karakoram fault system , southwest Tibet : Timing and magnitude of slip: Geology, v. 28, p. 451–454.

Murphy, M.A., Manning, C.E., Ryerson, F.J., and Lin, D., 2002, Structural evolution of the Gurla Mandhata detachment system, southwest Tibet : Implications for the eastward extent of the Karakoram fault system: , p. 428–447.

Najman, Y., Appel, E., Boudagher-Fadel, M., Bown, P., Carter, A., Garzanti, E., Godin, L., Han, J., Liebke, U., Oliver, G., Parrish, R., and Vezzoli, G., 2010, Timing of India-Asia collision: Geological, biostratigraphic, and palaeomagnetic constraints: Journal of Geophysical Research, v. 115, no. B12, p. 1–18, doi: 10.1029/2010JB007673.

Niemi, N.A., & Clark, M.K., 2017, Long-term exhumation rates exceed paleoseismic slip rates in the central Santa Monica Mountains, Los Angeles County, California, Geology, v. 46, p. 63-66, doi: 10.1130/G39388.1.

Niemi, N.A., Buscher, J.T., Spotila, J.A., House, M.A., and Kelley, S.A., 2013, Insights from low-temperature thermochronometry into transpressional deformation and crustal exhumation along the San Andreas fault in the western Transverse Ranges, California: Tectonics, v. 32, p. 1602–1622, doi: 10.1002/2013TC003377.

Ouimet, W., Whipple, K., Royden, L., Reiners, P., Hodges, K., and Pringle, M., 2010, Regional incision of the eastern margin of the Tibetan Plateau: Lithosphere, v. 2, p. 50–63, doi: 10.1130/L57.1.Polissar, P.J., Freeman, K.H., Rowley, D.B., McInerney, F.A., and Currie, B.S., 2009, Paleoaltimetry of the Tibetan Plateau from D/H ratios of lipid biomarkers: Earth and Planetary Science Letters, v. 287, p. 64–76, doi: 10.1016/j.epsl.2009.07.037.

Owens, T. J., and G. Zandt, 1997, Implications of crustal property variations for models of Tibetan Plateau evolution, Nature, 387, 37–43.

Platt, J. P., and England, P. C., 1994, Convective removal of lithosphere beneath mountain belts; thermal and mechanical consequences: American Journal of Science, v. 294, no. 3, p. 307-336.

Phillips, R.J., Parrish, R.R., and Searle, M.P., 2004, Age constraints on ductile deformation and long-term slip rates along the Karakoram fault zone, Ladakh: v. 226, p. 305–319, doi: 10.1016/j.epsl.2004.07.037.

van der Pluijm, B.A, Hall, C.M., Vrolijk, P.J., Pevear, D.R., and Covey, M.C., 2001, The dating of shallow faults in the Earth’s crust.: Nature, v. 412, p. 172–175, doi: 10.1038/35084053.

Polissar, P.J., Freeman, K.H., Rowley, D.B., McInerney, F.A., and Currie, B.S., 2009, Paleoaltimetry of the Tibetan Plateau from D/H ratios of lipid biomarkers: Earth and Planetary Science Letters, v. 287, p. 64–76, doi: 10.1016/j.epsl.2009.07.037.

QBGMR (Qinghai Bureau of Geology and Mineral Resources), 1980, Geologic map of the Dongwenquan region, scale 1:200,000.

QBGMR (Qinghai Bureau of Geology and Mineral Resources), 1981, Geologic map of the Aikendelesite region, scale 1:200,000.

Ratschbacher, L., Krumrei, I., lumenwitz, M., Staiger, M., Gloaguen, R., Miller, B.V., Samson, S.D., Edwards, M.A., Appel, E., 2011, Rifting and strike-slip shear in central Tibet and the geometry, age and kinematics of upper crustal extension in Tibet: Geol. Soc. Spec. Publ., v. 353, no. 1, p. 127–163, doi:10.1144/SP353.8.

Reiners, P.W., and Farley, K.A., 2001, Influence of crystal size on apatite (U-Th)/He thermochronology and example from the Bighorn Mountains, Wyoming: Earth and Planetary Science Letters, v. 188, p. 413–420.

Renne, P.R., Swisher, C.C., Deino, A.L., Karner, D.B., Owens, T.L., and Depaolo, D.J., 1998, Intercalibration of standards, absolute ages and uncertainties in $^{40}Ar/^{39}Ar$ dating: Chemical Geology, v. 145, p. 117–152.

Rey, P., Vanderhaeghe, O., and Teyssier, C., 2001, Gravitational collapse of the continental crust: definition, regimes and modes: Tectonophysics, v. 342, no. 3, p. 435-449.

Ritts, B.D., Yue, Y., Graham, S. a., Sobel, E.R., Abbink, O. a., and Stockli, D., 2008, From sea level to high elevation in 15 million years:Uplift history of the northern Tibetan Plateau margin in the Altun Shan: American Journal of Science, v. 308, no. 5, p. 657–678, doi: 10.2475/05.2008.01.

Rohrmann, A., Kapp, P., Carrapa, B., Reiners, P.W., Guynn, J., Ding, L., and Heizler, M., 2012, Thermochronologic evidence for plateau formation in central Tibet by 45 Ma: Geology, v. 40, no. 2, p. 187–190, doi: 10.1130/G32530.1.

Rowley, D.B., 1996, Age of initiation of collision between India and Asia: A review of stratigraphic data: Earth and Planetary Science Letters, v. 145, p. 1–13.

Rowley, D.B., and Currie, B.S., 2006, Palaeo-altimetry of the late Eocene to Miocene Lunpola basin, central Tibet: Nature, v. 439, p. 677–81, doi: 10.1038/nature04506.

Royden, L., Burchfiel, B., King, R., Wang, E., Chen, Z., Shen, F., and Liu, Y., 1997, Surface Deformation and Lower Crustal Flow in Eastern Tibet: Science, v. 276, p. 788–790.

Shi, W.B., Wang, F., Wu, L., Yang, L.K., Zhang, W.B., and Wang, Y.Z., 2018, A prolonged Cenozoic erosional period in East Kunlun (Western China): Constraints of detrital apatite

(U-Th)/He ages on the onset of mountain building along the northern margin of the Tibetan Plateau: Journal of Asian Earth Sciences, v. 151, p. 54-61.

Spotila, J., Farley, K.A., and Sich, K., 1998, Uplift and erosion of the San Bernardino Mountains associated with transpression along the San Andreas fault, California, as constrained by radiogenic helium thermochronometry: Tectonics, v. 17, p. 360–378.

Spotila, J. A., Farley, K. A., Yule, J.D., and Reiners, P.W., 2001, Near-field transpressive deformation along the San Andreas fault zone in southern California, based on exhumation constrained by (U-Th)/He dating: Journal of Geophysical Research, v. 106, p. 30909, doi: 10.1029/2001JB000348.

Spotila, J. A., Niemi, N., Brady, R., House, M., Buscher, J., and Oskin, M., 2007, Long-term continental deformation associated with transpressive plate motion: The San Andreas fault: Geology, v. 35, p. 967, doi: 10.1130/G23816A.1.

Srodon, J., and Eberl, D.D., 1984, Illite: Reviews in Mineralogy and Geochemistry1, v. 13, p. 495–544.

Staisch, L.M., Niemi, N.A., Chang, H., Clark, M.K., Rowley, D.B., and Currie, B.S., 2014, A Cretaceous-Eocene depositional age for the Fenghuoshan Group, Hoh Xil Basin: Implications for the tectonic evolution of the northern Tibet Plateau: Tectonics, v. 33, p. 281–301, doi: 10.1002/2013TC003367.

Staisch, L. M., N. A. Niemi, M. K. Clark, C. Hong, 2016, Eocene – late Oligocene history of crustal shortening within the Hoh Xil Basin and implications for the uplift history of the northern Tibetan Plateau, Tectonics, v. 35, p. 862–895, doi: 10.1002/2015TC003972.

Styron, R., Taylor, M., Okoronkwo, K., 2010, Database of active structures from the Indo-Asian collision. Eos, Transactions American Geophysical Union, v. 91(20), p. 181-182.

Styron, R.H., Taylor, M.H., Sundell, K.E., Stockli, D.F., Oalmann, J. a. G., Möller, A., McCallister, A.T., Liu, D., and Ding, L., 2013, Miocene initiation and acceleration of extension in the South Lunggar rift, western Tibet: Evolution of an active detachment system from structural mapping and (U-Th)/He thermochronology: Tectonics, v. 32, p. 880–907, doi: 10.1002/tect.20053.

Sundell, K.E., Taylor, M.H., Styron, R.H., Stockli, D.F., Kapp, P., Hager, C., Liu, D., Ding, L., 2013, Evidence for constriction and Pliocene acceleration of east-west extension in the North Lunggar rift region of west central Tibet: Tectonics, v. 32, no. 5, p. 1454–1479.

Taylor, M., Yin, A., Ryerson, F.J., Kapp, P., and Ding, L., 2003, Conjugate strike-slip faulting along the Bangong-Nujiang suture zone accommodates coeval east-west extension and north-south shortening in the interior of the Tibetan Plateau: Tectonics, v. 22, p. 1–16, doi: 10.1029/2002TC001361.

Taylor, M., and Peltzer, G., 2006, Current slip rates on conjugate strike-slip faults in central Tibet using synthetic aperture radar interferometry: Journal of Geophysical Research, v. 111, B12402, doi: 10.1029/2005JB004014.

Teyssier, C., Tikoff, B., and Markley, M., 1995, Oblique plate motion and continental tectonics: Geology, v. 23, p. 447–450, doi: 10.1130/0091-7613(1995)023<0447:OPMACT>2.3.CO;2.

Tikoff, B., and Teyssier, C., 1994, Strain modeling of displacement-field partitioning in transpressional orogens: Journal of Structural Geology, v. 16, p. 1575–1588.

Turner, S., C. Hawkesworth, J. Liu, N. Rogers, S. P. Kelley, and P. van Calsteren, 1993, Timing of Tibetan uplift constrained by analysis of volcanic rocks, Nature, 364, 50–54, doi:10.1038/364050a0.

Turner, S., N. Arnaud, J. Liu, N. Rogers, C. Hawkesworth, N. Harris, S. P. Kelley, P. van Calsteren, and W. Deng, 1996, Post-collision, shoshonitic volcanism on the Tibetan Plateau: Implications for convective thinning of the lithosphere and the source of ocean island basalts, J. Petrol., 37, 45–71, doi:10.1093/petrology/37.1.45

Verdel, C., van der Pluijm, B.A., and Niemi, N.A., 2012, Variation of illite/muscovite $^{40}Ar/^{39}Ar$ age spectra during progressive low-grade metamorphism: an example from the US Cordillera: Contributions to Mineralogy and Petrology, v. 164, p. 521–536, doi: 10.1007/s00410-012-0751-7.

Wang, F., Lo, C.-H., Li, Q., Yeh, M.-W., Wan, J., Zheng, D., and Wang, E., 2004, Onset timing of significant unroofing around Qaidam basin, northern Tibet, China: constraints from $^{40}Ar/^{39}Ar$ and FT thermochronology on granitoids: Journal of Asian Earth Sciences, v. 24, p. 59–69, doi: 10.1016/j.jseaes.2003.07.004.

Wang, Q., McDermott, F., Xu, J., Bellon, H., and Zhu, Y., 2005, Cenozoic K-rich adakitic volcanic rocks in the Hohxil area, northern Tibet: Lower-crustal melting in an intracontinental setting: Geology, v. 33, p. 465–468, doi: 10.1130/G21522.1.

Wang, C.S., Zhao, X., Liu, Z., Lippert, P.C., Graham, S.A, Coe, R.S., Yi, H., Zhu, L., Liu, S., and Li, Y., 2008, Constraints on the early uplift history of the Tibetan Plateau.: Proceedings of the National Academy of Sciences of the United States of America, v. 105, no. 13, p. 4987–4992, doi: 10.1073/pnas.0703595105.

Wang, S., Fang, X., Zheng, D., and Wang, E., 2009, Initiation of slip along the Xianshuihe fault zone, eastern Tibet, constrained by K/Ar and fission-track ages: International Geology Review, v. 51, p. 1121–1131, doi: 10.1080/00206810902945132.

Wang, Q., S. L. Chung, X. Li, D. A. Wyman, Z. X. Li, W. Sun, H. N. Qiu, Y. S. Liu, and Y. Zhu, 2012, Crustal melting and flow beneath northern Tibet: Evidence from mid-Miocene to Quaternary strongly peraluminous rhyolites in the Southern Kunlun Range, J. Petrol., 53, 2523–2566, doi:10.1093/petrology/egs058.

Wang, Z., Zhang, P., Garzione, C.N., Lease, R.O., Zhang, G., Zheng, D., Hough, B., Yuan, D., Li, C., and Liu, J., 2012, Magnetostratigraphy and depositional history of the Miocene Wushan basin on the NE Tibetan plateau, China: Implications for middle Miocene tectonics of the West Qinling fault zone: Journal of Asian Earth Sciences, v. 44, p. 189–202, doi:10.1016/j.jseaes.2011.06.009.

Warnock, A.C., Zeitler, P.K., Wolf, R.A., and Bergman, S.C., 1997, An evaluation of low-temperature apatite U-Th/He thermochronometry: Geochimica et Cosmochimica Acta, v. 61, p. 5371–5377, doi: 10.1016/S0016-7037(97)00302-5.

Wilcox, R.E., Harding, T.T., and Seely, D.R., 1973, Basic wrench tectonics: AAPG Bulletin, v. 57, p. 74–96.

Williams, H.M., Turner, S.P., Pearce, J.A., Kelley, S.P., and Harris, N.B.W., 2004, Nature of the Source Regions for Post-collisional, Potassic Magmatism in Southern and Northern Tibet from Geochemical Variations and Inverse Trace Element Modelling: Journal of Petrology, v. 45, p. 555–607, doi: 10.1093/petrology/egg094.

Wu, C., Zuza, A.V., Zhuo, Z., Yin, A., McRivette, M.W., Chen, X., Ding, L., Geng, J., 2019, Mesozoic-Cenozoic evolution of the Eastern Kunlun Range, central Tibet, and implications for basin evolution during the Indo-Asian collision, Lithosphere, doi: https://doi.org/10.1130/L1065.1.

van der Woerd, J., Tapponnier, P., Ryerson, F.J., Meriaux, A., Meyer, B., Gaudemer, Y., Finkel, R.C., Caffee, M.W., Guoguang, Z., and Zhiqin, X., 2002, Uniform postglacial slip-rate along the central 600 km of the Kunlun Fault (Tibet), from $^{26}$Al, $^{10}$Be, $^{14C}$ dating of riser offsets, and climatic orogin of the regional morphology: Geophysical Journal International, v. 148, p. 356–388.

van der Woerd, J., Ryerson, F.J., Tapponnier, P., Meriaux A.S., Gaudemer Y., Meyer, B., Finkel, R.C., Caffee, M.W., Zhao, G., and Xu, Z., 2000, Uniform slip-rate along the Kunlun Fault: Implications for seismic behaviour and large-scale tectonics: Geophysical Research Letters, v. 27, no. 16, p. 2353-2356.

van der Woerd, J., Ryerson, F.J., Tapponnier, P., Gaudemer, Y., Finkel, R.C., Meriaux, A.-S., Caffee, M.W., Zhao, G., and He, Q., 1998, Holocene left-slip rate determined by cosmogenic surface dating on the Xidatan segment of the Kunlun fault (Qinghai, China): Geology, v. 26, p. 695–698, doi: 10.1130/0091-7613(1998)026<0695.

Wolf, R.A., Farley, K.A., and Kass, D.M., 1998, Modeling of the temperature sensitivity of the apatite (U-Th)/He thermochronometer: Chemical Geology, v. 148, p. 105–114.

Wolf, R.A., Farley, K.A., Silver, L.T., Geological, D., Sciences, P., and Stop, M., 1996, Helium diffusion and low-temperature thermochronometry of apatite: Geochemica et Cosmochemica Acta, v. 60, p. 4231–4240.

Wu, F., Zhang, X.J., Zhang, Y.Q., Zhang, Y.L., 2010, Zircon U-Pb ages for rhyolitic tuffs of the Naocangjianguo Formation in the east Kunlun Orogenic Belt and their implication: Journal of Geomechanics, v. 16(1), p. 44–50.

Wu, C., Zuza, A.V., Chen, X., Lin, D., Levy, D.A., Liu, C., Liu, W., Tian, J., Stockli, D.F., 2019, Tectonics of the Eastern Kunlun Range: Cenozoic reactivation of a Paleozoic-early Mesozoic Orogen: Tectonics, v. 38, p. 1609–1650, doi: 10.1029/2018TC005370.

Wu, Y., Cui, Z., Liu, G., Ge, D., Yin, J., Xi, Q., and Pang, Q., 2001, Quaternary geomorphological evolution of the Kunlun Pass area and uplift of the Qinghai-Xizang, Tibet Plateau: Geomorphology, v. 36, p. 203–216.

Wu, Z. H., Ye, P. S., Zhao, W. J., et al., 2007, Late Cenozoic Overthrust System in the Southern East Kunlun Mountains, China: Geological Bulletin of China, v. 26, no. 4, p. 448–456 (in Chinese with English Abstract).

Wu, Z., Barosh, P.J., Wu, Z., Hu, D., Zhao, X., and Ye, P., 2008, Vast early Miocene lakes of the central Tibetan Plateau: Geological Society of America Bulletin, v. 120, no. 9-10, p. 1326–1337, doi: 10.1130/B26043.1.

Wu, Z., Ye, P., Patrick, B.J., Hu, D., Zhao, W., and Wu, Z., 2009, Late Oligocene-Early Miocene thrusting in southern East Kunlun Mountains, northern Tibetan plateau: Journal of Earth Science, v. 20, p. 381–390, doi: 10.1007/s12583-009-0031-2.

Xia, L., Li, X., Ma, Z., Xu, X., and Xia, Z., 2011, Cenozoic volcanism and tectonic evolution of the Tibetan plateau: Gondwana Research, v. 19, p. 850–866, doi: 10.1016/j.gr.2010.09.005.

Xu, Q., Ding, L., Zhang, L., Cai, F., Lai, Q., Yang, D., and Liu-Zeng, J., 2013, Paleogene high elevations in the Qiangtang Terrane, central Tibetan Plateau: Earth and Planetary Science Letters, v. 362, p. 31–42, doi: 10.1016/j.epsl.2012.11.058.

Yakovlev, P. V., Saal, A., Clark, M. K., Hong, C., Niemi, N. A., Mallick, S., 2019, The geochemistry of Tibetan lavas: Spatial and temporal relationships, tectonic links and geodynamic implications, Earth and Planetary Science Letters, vol. 520, p. 115–126.

Yang, D., and L. Ding, 2013, Geochronology and geochemistry of the high magnesium and high potassium ultrabasic leucite basanite in northern Tibetan Plateau, Chin. J. Geol., 48, 449–467.

Yin, A., Rumelhart, P.E., Butler, R., Cowgill, E., Harrison, T.M., Foster, D.A., Ingersoll, R.V., Qing, Z., Xian-Qiang, Z., Xiao-Feng, W., Hanson, A., and Raza, A., 2002, Tectonic history of the Altyn Tagh fault system in northern Tibet inferred from Cenozoic sedimentation: Geological Society of America Bulletin, v. 114, p. 1257–1295, doi: 10.1130/0016-7606(2002)114<1257:THOTAT>2.0.CO;2.

Yin, A., Dang, Y.-Q., Wang, L.-C., Jiang, W.-M., Zhou, S.-P., Chen, X.-H., Gehrels, G.E., and McRivette, M.W., 2008, Cenozoic tectonic evolution of Qaidam basin and its surrounding regions (Part 1): The southern Qilian Shan-Nan Shan thrust belt and northern Qaidam basin: Geological Society of America Bulletin, v. 120, p. 813–846, doi: 10.1130/B26180.1.

Yin, A., Dang, Y., Zhang, M., McRivette, M.W., Burgess, W.P., and Chen, X., 2007, Cenozoic tectonic evolution of Qaidam basin and its surrounding regions (part 2): Wedge tectonics in southern Qaidam basin and the Eastern Kunlun Range: Geological Society of America Special Papers, v. 433, p. 369–390, doi: 10.1130/2007.2433(18).

Yuan, W., Dong, J., Shicheng, W., and Carter, A., 2006, Apatite fission track evidence for Neogene uplift in the eastern Kunlun Mountains, northern Qinghai–Tibet Plateau, China: Journal of Asian Earth Sciences, v. 27, p. 847–856, doi: 10.1016/j.jseaes.2005.09.002.

Yue, Y., Ritts, B.D., and Graham, S. a., 2001, Initiation and Long-Term Slip History of the Altyn Tagh Fault: International Geology Review, v. 43, no. 12, p. 1087–1093, doi: 10.1080/00206810109465062.

Yue, Y., Ritts, B.D., Graham, S. a., Wooden, J.L., Gehrels, G.E., and Zhang, Z., 2004, Slowing extrusion tectonics: lowered estimate of post-Early Miocene slip rate for the Altyn Tagh fault: Earth and Planetary Science Letters, v. 217, no. 1-2, p. 111–122, doi: 10.1016/S0012-821X(03)00544-2.

Zhuang, G., Johnstone, S.A., Hourigan, J., Ritts, B., Robinson, A., Sobel, E.R., 2018, Understanding the geologic evolution of Northern Tibetan Plateau with multiple thermochronometers: Gondwana Research, v. 58, p. 195–210, doi: 10.1016/j.gr.2018.02.014

## FIGURE CAPTIONS

**Fig. 1.** Hillshade map of the central East Kunlun Shan with the general location marked in the inset map of the Tibetan Plateau. Active strike-slip faults and oblique-slip faults are shown. Thermochronologic and fault slip rate studies are denoted for reference. The modeled timing of initial rapid cooling, in millions of years, for samples from Mock et al. (1999), Clark et al. (2010), and Duvall et al. (2013) are outlined in blue, red, and black, respectively. Single numbers represent a well-constrained modeled onset of uplift whereas numbers separated by a hyphen represent a period of time during which the onset of uplift is modeled to have occurred. Numbers separated by a comma represent potential multiple stages of uplift. Locations labeled “not modeled” indicate sample locations for which geochronologic data exists, but was not modeled for uplift history. Thermochronologic samples from this study are marked in red. The orange - blue gradient overlay qualitatively shows expected vertical uplift and subsidence related to recent strike-slip fault motion. The assignment of strike-slip related vertical motion was assessed by comparing regional topographic patterns, known strike-slip fault locations from prior geologic mapping (QBGMR,

1980; 1981; Van der Woerd et al., 2002), and observations of strike-slip related vertical motion in field and theoretical studies (Chinnery, 1965; Crowell, 1974; Biddle and Christie-Blick, 1985; Bilham and King, 1989). The locations of geologic maps in Fig. 2 are indicated.

**Fig. 2.** Geologic maps of (A) the Dongdatan Valley and East Wenquan Basin and (B) the East Deshuiwai Mountains and Deshuiwai Basin based on original mapping, published geologic maps (QBGMR, 1980; 1981), and satellite imagery. Hillshade is based on data from the Advanced Spaceborne Thermal Emission and Reflection Radiometer (ASTER). Fault gouge and thermochronologic samples are shown as yellow and green circles, respectively. Apatite (U-Th)/He ages are printed in italics, apatite fission-track ages are printed in bold italics, and zircon (U-Th)/He ages are printed in bold. Most ages reported are mean and standard deviation, except for 13DDT008 and 13DDT009 which are reported as a range due to broad scatter in Apatite (U-Th)/He data.

**Fig. 3.** Geologic map of the Dongdatan Valley and East Wenquan Basin based on original mapping, published geologic maps (QBGMR, 1980; 1981), and satellite imagery. Hillshade and topographic contours are based on ASTER imagery. Fault gouge and thermochronologic samples are shown as yellow and green circles, respectively. Apatite (U-Th)/He ages are printed in italics, apatite fission-track ages are printed in bold italics, and zircon (U-Th)/He ages are printed in bold.

**Fig. 4.** Field photographs of sedimentary features. (A) Tilted Triassic Babaoshan Group unconformably deposited on lower – mid Triassic plutonic rocks within the Deshuiwai Basin. (B) Flat-lying Jurassic – Cretaceous Yangqu Group in the central Deshuiwai Basin with SUVs for scale. (C) Conglomerate of the Yangqu Group showing a heterogeneous source, generally dominated by Permian carbonate and Triassic metapelites. (D) Fine sandstone of the Cenozoic red beds show well developed cross bedding, indicative of a medium-energy fluvial environment. (E) Finely laminated lacustrine carbonate and carbonate-rich siltstone sequence of the Neogene Quoguo

Group. (F) Flat-lying Cenozoic red bed strata are unconformably deposited over steeply dipping and tightly folded Triassic metapelites.

**Fig. 5.** Field photographs of structural features observed. (A) Axial planar cleavage developed in shale layers and tilted sandstone bedding within the Triassic Naocangjiangou Group. (B) westward-looking photo of a large strike-slip fault along the northern Dongdatan Valley, with friable Triassic strata to the south (left) and steep topography developed within the Permian carbonate units to the north (right). (C) well developed breccia along the same fault shown in picture (B). (E) Taken looking roughly northeast and shows a well defined thrust fault with Triassic metapelites thrust over upper Yangqu Group red bed strata.

**Fig. 6.** QTQt modeling (Gallagher, 2012) results of thermochronologic data from various fault blocks in the central East Kunlun Shan. (A) Model results for crustal exhumation proximal to the Xidatan fault. (B) Model results for exhumation of the hanging wall of the Wenquan Hu thrust fault. (C) Model results for burial and exhumation of the footwall of the Wenquan Hu thrust fault. Green box represents the geologic constraint for deposition at surface temperatures of the Yangqu Group. (D) Model results for exhumation of the East Deshuiwai Mountains, a restraining bend along the Xidatan fault zone. (E) Model results for the Deshuiwai Basin, with a geologic constraint for deposition at surface temperatures of the Babaoshan Group.

**Fig. 7.** Observed and predicted thermochronologic ages for best fit QTQt models shown in Figure 6. Plots show age and 1σ uncertainty, as well as a dashed 1:1 line to assess goodness of fit. Apatite fission track ages and individual apatite and zircon (U-Th)/He aliquot ages for modeling time-temperature paths (A) near the Xidatan fault, (B) in the Wenquan Hu hanging wall fault block, (C) in the Wenquan Hu footwall fault block, (D) in the East Deshuiwai Mountains restraining bend, and (E) in Deshuiwai Basin. (F) Mean observed and modeled ages are calculated from the

individual ages shown in figures 7A-E for each sample modeled in all fault blocks. Modeling results for the Wenquan Hu hanging wall block are nearly identical whether 12DDT07 is included or excluded from QTQt. Despite ~20% uncertainty in 12DDT09 the mean zircon (U-Th)/He age, inclusion of these data improve the model fit to all other observed samples. Abbreviations include AHe: apatite (U-Th)/He, AFT: apatite fission track, and ZHe: zircon (U-Th)/He.

**Fig. 8.** Results for fault gouge dating within the Dongdatan Valley. For each sample, size fraction aliquot age and illite concentrations are plotted as small dots. Age errors are present but hidden by the size of data points. Data points that are used for authigenic illite age estimation are shown as white dots and data points omitted are shown as grey dots. The best-fit results from Bayesian linear regression are shown as dark blue lines and other acceptable linear regression lines are shown in lighter blue. (A) Thrust fault sample 11UMT55 with an estimated fault gouge age of 46.6 Ma. (B) Thrust fault sample 12DDT18 with an estimated fault gouge age of 112.5 Ma. (C) Strike-slip fault sample 11UMT50 with an estimated fault gouge age of 90.4 Ma. (D) Strike-slip fault sample 11UMT52 with no estimate for the timing of fault motion due to lack of linear age-illite concentration trend.

**Fig. 9.** Schematic block diagrams showing the evolution of deformation within the Dongdatan Valley. (A) Field observations of Permian carbonates thrust over Triassic metapelites and regional dating of plutons and metamorphic cooling episodes (Mock et al., 1999; Liu et al., 2005; Wu et al., 2019) suggest that the East Kunlun Shan experienced late Triassic north-south oriented compression from the northward accretion of the Qiangtang block. (B) North-south compression may have been reactivated during Jurassic – Cretaceous accretion of the Lhasa block based on the timing of Yangqu Group deposition and a separate regional cooling event documented in the West and East Kunlun Shan (Liu et al., 2005; Li et al., 2019). Permian marbles and Triassic metapelites

were exposed at the time of Yangqu deposition. (C) Late Cretaceous to Eocene shortening from collision between India and Eurasia resulted in thrust faulting along the Wenquan Hu thrust fault and burial of terrestrial strata in the footwall. Shortening and exhumation may have continued elsewhere in the East Kunlun Shan into late Eocene time, but ceased along the Wenquan Hu thrust fault by 43 Ma. (D) East-west oriented strike-slip faulting locally causes exhumation and erosion. Thermochronologic modeling suggest that strike-slip faulting initiated by ~20 Ma. Miocene – present strike-slip faulting results in basin subsidence in the East Wenquan basin, deposition of terrestrial strata, and juxtaposition of Jurassic – Cretaceous and Cenozoic strata.

**Fig. 10.** Schematic orogen-scale cross section of the geodynamic evolution of the Tibetan Plateau. (a) The onset of crustal shortening and thickening in northern Tibet soon after the Indo-Asian collision continued into late Oligocene time with moderate elevation gain. (b) Shortening in northern Tibet continues as a southward sweep of magmatism suggests the onset of slab rollback in southern Tibet. (c) Shortening ceases within the Hoh Xil Basin by 27 Ma and likely by 24 Ma in the East Kunlun Shan. Surface uplift may have continued due to crustal thickening via lower crustal flow in northern Tibet. Continued slab rollback may have destabilized the northern Tibetan mantle root by removing is southern buttress. (d) The onset of strike-slip faulting in the East Kunlun Shan between 23 and 20 Ma is coincident with proposed slab breakoff and elevation gain in southern Tibet, and proposed mantle root loss, surface uplift and increased magmatism within the northern Tibet. (e) After 20 Ma, strike-slip and normal faulting expanded throughout the Tibetan Plateau, coincident with the proposed onset of eastward-directed lower crustal flow.

**Fig. 11.** Map of major active strike-slip and normal faults in the Tibetan Plateau, adapted from Styron et al. (2010) and Fu et al. (2011). The estimated initiation age of each fault system is denoted, along with abbreviated names. Abbreviations for strike-slip faults are as follows; cKF: central

Kunlun Fault, eKF: east Kunlun Fault , wKF: west Kunlun Fault, wHF: west Haiyuan Fault, EF: Elashan Fault, RF: Riyueshan Fault, ATF: Altyn Tagh Fault, JF: Jiali Fault, RRF: Red River Fault; KF: Karakoram Fault, XF: Xianshuihe Fault, RCF: Riganpei Co Fault, GCF: Gyaring Co Fault, BCFS: Bue Co Fault System. Abbreviations for normal faults are as follows; TG: Thakkola Graben, ADR: Ama Drime Rift, KCR: Kung Co Rift, GMR: Gurla Mandhata Rift, RG: Ringbung Graben, YR: Yadong Rift, LR: Lunggar Rift, NR: Nyainqentanghlah Rift, LKR: Lopukangri Rift, TYCR: Tangra Yum Co Rift, PXR: Pumqu-Xainza Rift, GR: Gulu Rift, SHG: Shuang Hu Graben. Citations for the initiation of faulting are available in Tables S5 and S6.

Figure 1.

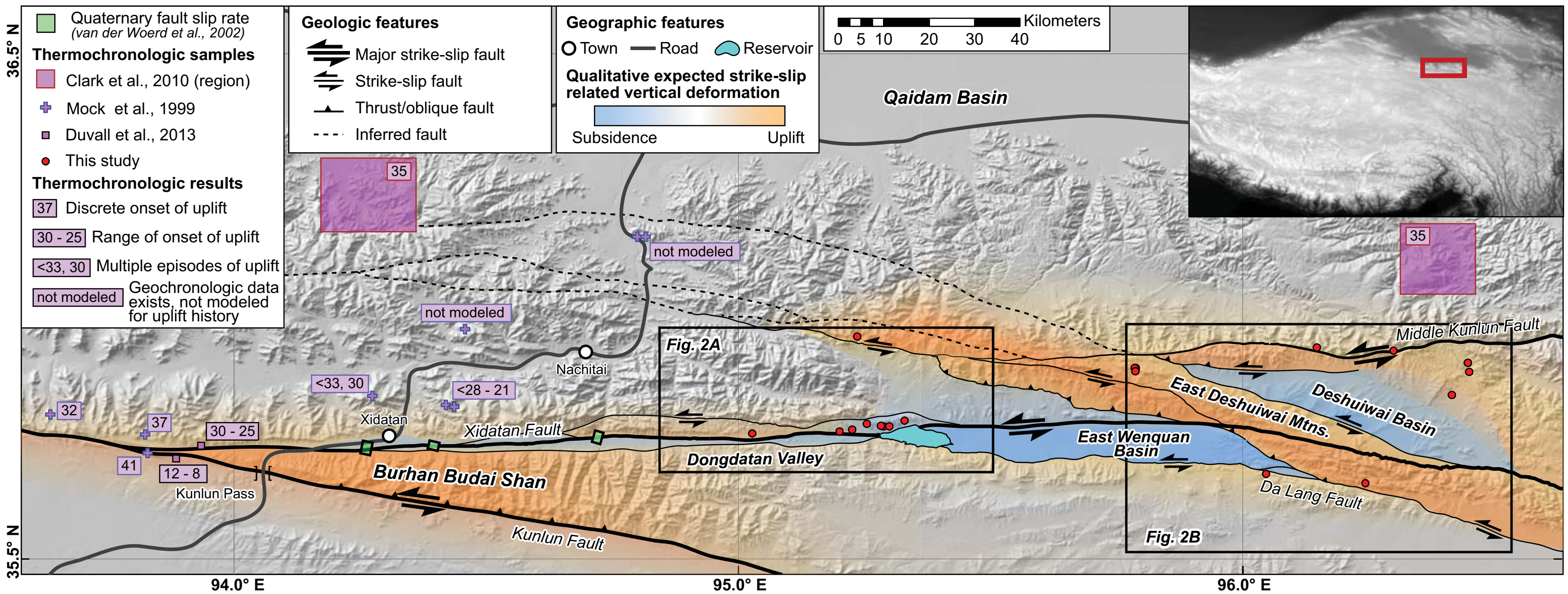
Quaternary fault slip rate (van der Woerd et al., 2002)
Thermochronologic samples
Clark et al., 2010 (region)
Mock et al., 1999
Duvall et al., 2013
This study
Thermochronologic results
37 Discrete onset of uplift
30 - 25 Range of onset of uplift
<33, 30 Multiple episodes of uplift
not modeled Geochronologic data exists, not modeled for uplift history
Geologic features
Major strike-slip fault
Strike-slip fault
Thrust/oblique fault
Inferred fault
Geographic features
Town
Road
Reservoir
Qualitative expected strike-slip related vertical deformation
Subsidence
Uplift
0 5 10 20 30 40 Kilometers
Qaidam Basin
Nachitai
Xidatan
Xidatan Fault
Kunlun Pass
Burhan Budai Shan
Kunlun Fault
Fig. 2A
Dongdatan Valley
East Wenquan Basin
Fig. 2B
East Deshuiwai Mtns.
Deshuiwai Basin
Middle Kunlun Fault
Da Lang Fault
36.5° N
35.5° N
94.0° E
95.0° E
96.0° E

**Figure 2.**

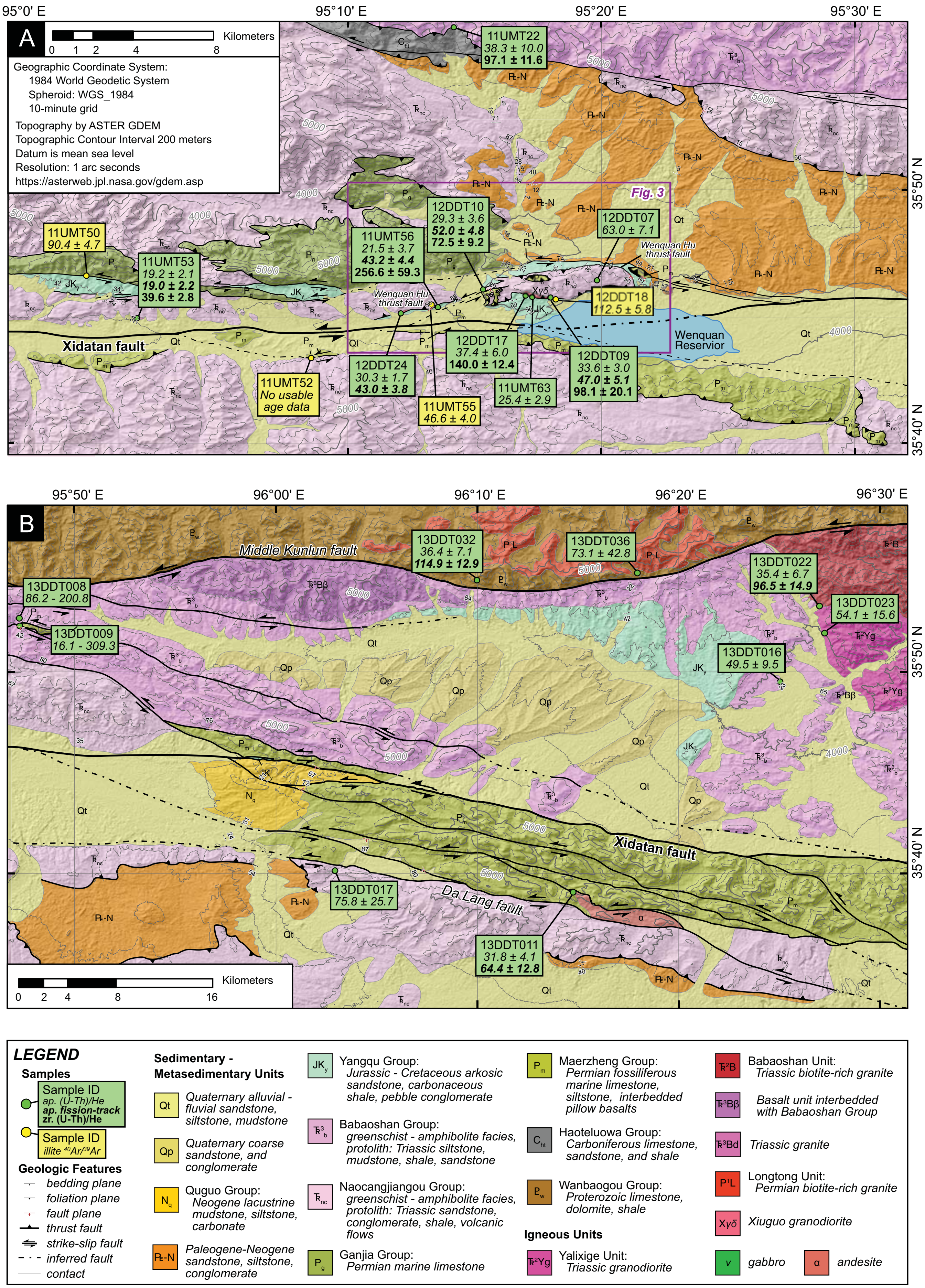
95°0' E
95°10' E
95°20' E
95°30' E
35°50' N
35°40' N
A
Kilometers
0 1 2 4 8
Geographic Coordinate System:
1984 World Geodetic System
Spheroid: WGS_1984
10-minute grid
Topography by ASTER GDEM
Topographic Contour Interval 200 meters
Datum is mean sea level
Resolution: 1 arc seconds
https://asterweb.jpl.nasa.gov/gdem.asp
11UMT22
38.3 ± 10.0
97.1 ± 11.6
Fig. 3
11UMT50
90.4 ± 4.7
11UMT53
19.2 ± 2.1
19.0 ± 2.2
39.6 ± 2.8
11UMT56
21.5 ± 3.7
43.2 ± 4.4
256.6 ± 59.3
12DDT10
29.3 ± 3.6
52.0 ± 4.8
72.5 ± 9.2
12DDT07
63.0 ± 7.1
Wenquan Hu thrust fault
12DDT18
112.5 ± 5.8
Xidatan fault
Wenquan Reservior
12DDT24
30.3 ± 1.7
43.0 ± 3.8
12DDT17
37.4 ± 6.0
140.0 ± 12.4
12DDT09
33.6 ± 3.0
47.0 ± 5.1
98.1 ± 20.1
11UMT52
No usable age data
11UMT55
46.6 ± 4.0
11UMT63
25.4 ± 2.9
95°50' E
96°00' E
96°10' E
96°20' E
96°30' E
B
Middle Kunlun fault
13DDT032
36.4 ± 7.1
114.9 ± 12.9
13DDT036
73.1 ± 42.8
13DDT022
35.4 ± 6.7
96.5 ± 14.9
13DDT023
54.1 ± 15.6
13DDT008
86.2 - 200.8
13DDT009
16.1 - 309.3
13DDT016
49.5 ± 9.5
Xidatan fault
Da Lang fault
13DDT017
75.8 ± 25.7
13DDT011
31.8 ± 4.1
64.4 ± 12.8
Kilometers
0 2 4 8 16
LEGEND
Samples
Sample ID
ap. (U-Th)/He
ap. fission-track
zr. (U-Th)/He
Sample ID
illite 40Ar/39Ar
Geologic Features
bedding plane
foliation plane
fault plane
thrust fault
strike-slip fault
inferred fault
contact
Sedimentary - Metasedimentary Units
Qt Quaternary alluvial - fluvial sandstone, siltstone, mudstone
Qp Quaternary coarse sandstone, and conglomerate
Nq Quguo Group: Neogene lacustrine mudstone, siltstone, carbonate
Pɛ-N Paleogene-Neogene sandstone, siltstone, conglomerate
JKy Yangqu Group: Jurassic - Cretaceous arkosic sandstone, carbonaceous shale, pebble conglomerate
Ŧ3b Babaoshan Group: greenschist - amphibolite facies, protolith: Triassic siltstone, mudstone, shale, sandstone
Ŧnc Naocangjiangou Group: greenschist - amphibolite facies, protolith: Triassic sandstone, conglomerate, shale, volcanic flows
Pg Ganjia Group: Permian marine limestone
Pm Maerzheng Group: Permian fossiliferous marine limestone, siltstone, interbedded pillow basalts
Cht Haoteluowa Group: Carboniferous limestone, sandstone, and shale
Pɛw Wanbaogou Group: Proterozoic limestone, dolomite, shale
Igneous Units
Ŧ2Yg Yalixige Unit: Triassic granodiorite
Ŧ2B Babaoshan Unit: Triassic biotite-rich granite
Ŧ3Bβ Basalt unit interbedded with Babaoshan Group
Ŧ3Bd Triassic granite
P1L Longtong Unit: Permian biotite-rich granite
Xγδ Xiuguo granodiorite
v gabbro
α andesite

**Figure 3.**

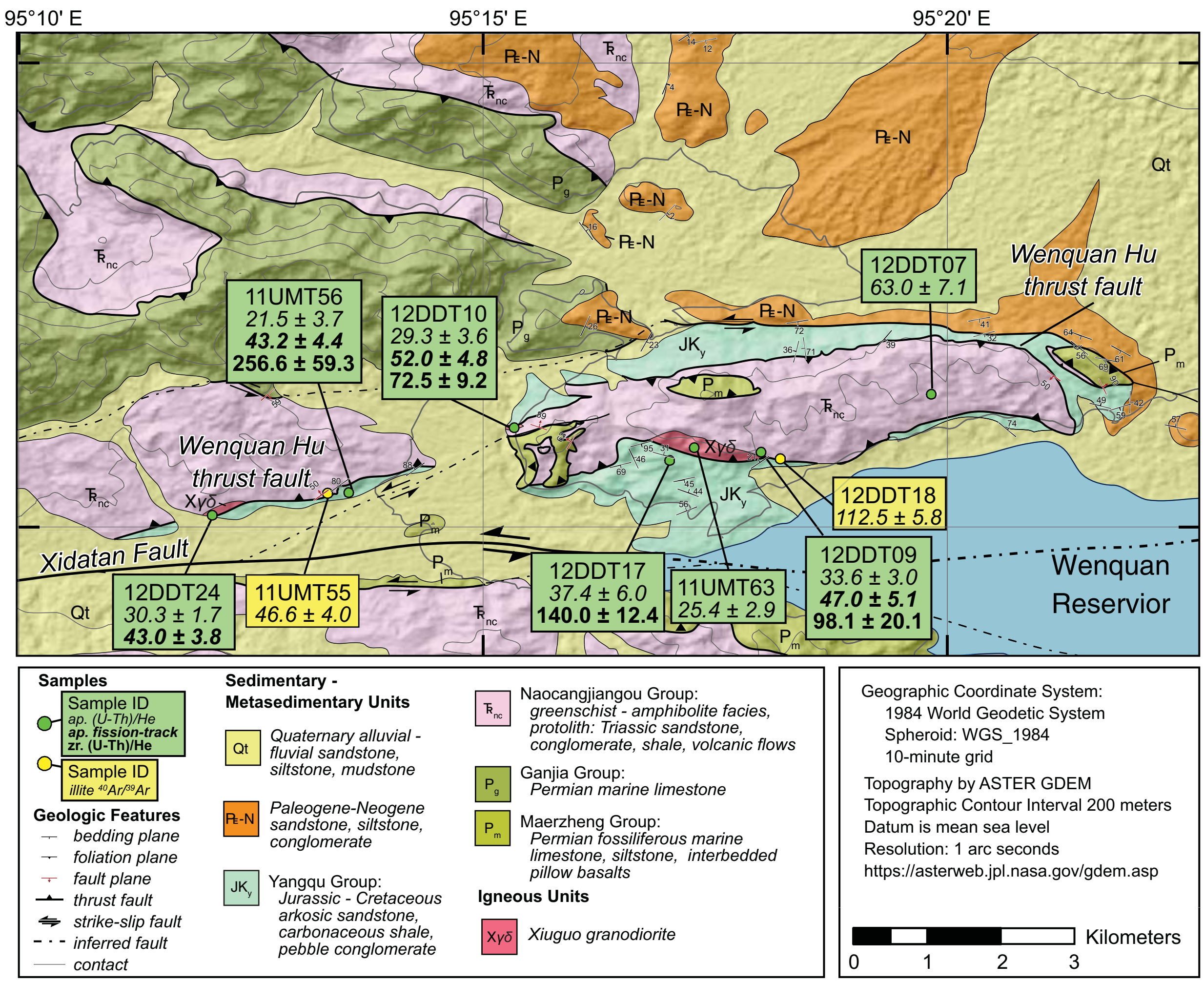
95°10' E
95°15' E
95°20' E
35°50' N
35°45' N
Wenquan Hu thrust fault
Wenquan Hu thrust fault
Xidatan Fault
Wenquan Reservior
12DDT07
63.0 ± 7.1
11UMT56
21.5 ± 3.7
43.2 ± 4.4
256.6 ± 59.3
12DDT10
29.3 ± 3.6
52.0 ± 4.8
72.5 ± 9.2
12DDT18
112.5 ± 5.8
12DDT24
30.3 ± 1.7
43.0 ± 3.8
11UMT55
46.6 ± 4.0
12DDT17
37.4 ± 6.0
140.0 ± 12.4
11UMT63
25.4 ± 2.9
12DDT09
33.6 ± 3.0
47.0 ± 5.1
98.1 ± 20.1
Samples
Sample ID
ap. (U-Th)/He
ap. fission-track
zr. (U-Th)/He
Sample ID
illite 40Ar/39Ar
Geologic Features
bedding plane
foliation plane
fault plane
thrust fault
strike-slip fault
inferred fault
contact
Sedimentary - Metasedimentary Units
Qt Quaternary alluvial - fluvial sandstone, siltstone, mudstone
Paleogene-Neogene sandstone, siltstone, conglomerate
JKy Yangqu Group: Jurassic - Cretaceous arkosic sandstone, carbonaceous shale, pebble conglomerate
Naocangjiangou Group: greenschist - amphibolite facies, protolith: Triassic sandstone, conglomerate, shale, volcanic flows
Ganjia Group: Permian marine limestone
Maerzheng Group: Permian fossiliferous marine limestone, siltstone, interbedded pillow basalts
Igneous Units
Xiuguo granodiorite
Geographic Coordinate System:
1984 World Geodetic System
Spheroid: WGS_1984
10-minute grid
Topography by ASTER GDEM
Topographic Contour Interval 200 meters
Datum is mean sea level
Resolution: 1 arc seconds
https://asterweb.jpl.nasa.gov/gdem.asp
Kilometers
0 1 2 3

**Figure 4.**

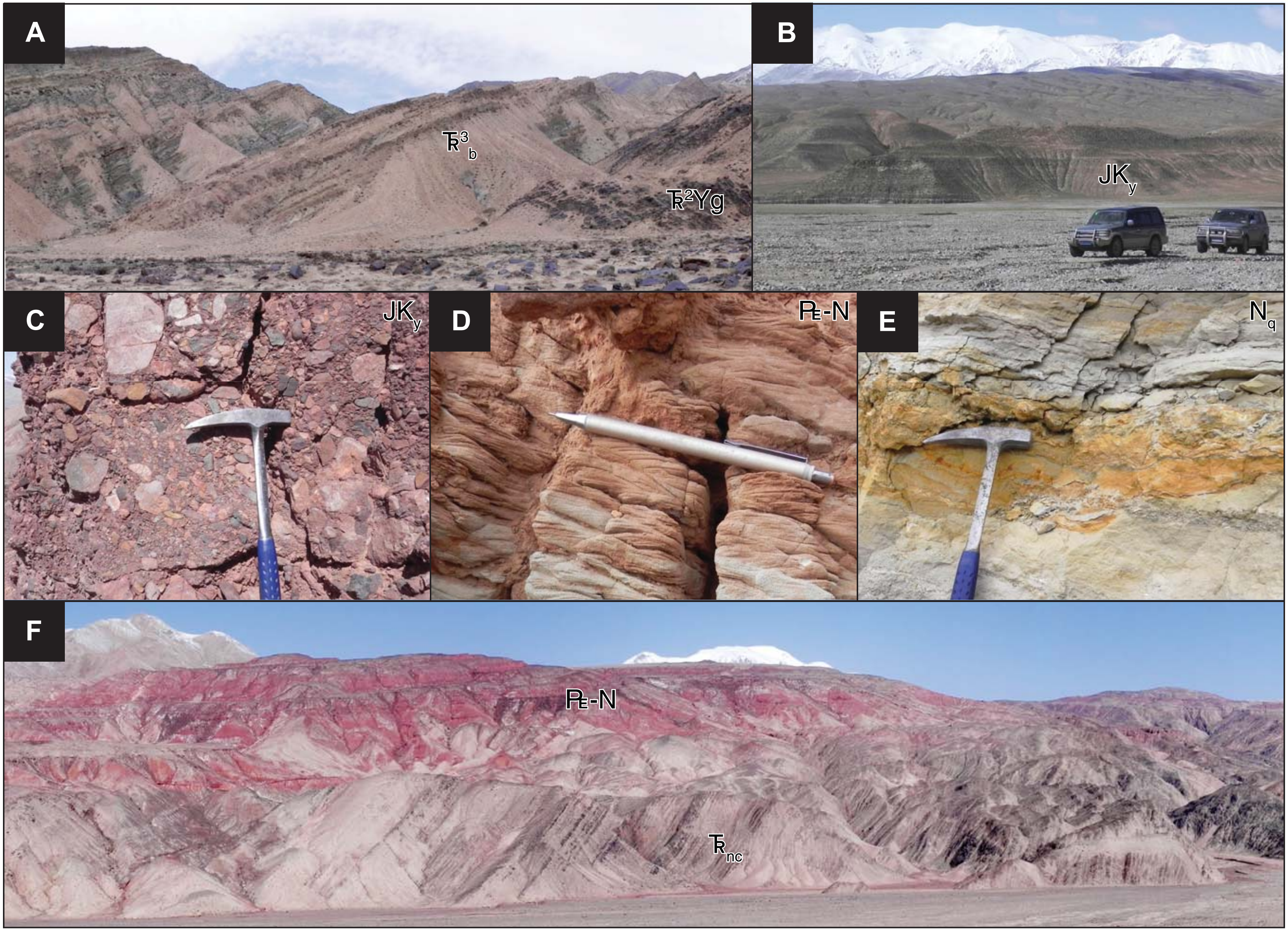
A
$TR^3_b$
$TR^2Yg$
B
$JK_y$
C
$JK_y$
D
PE-N
E
$N_q$
F
PE-N
$TR_{nc}$

**Figure 5.**

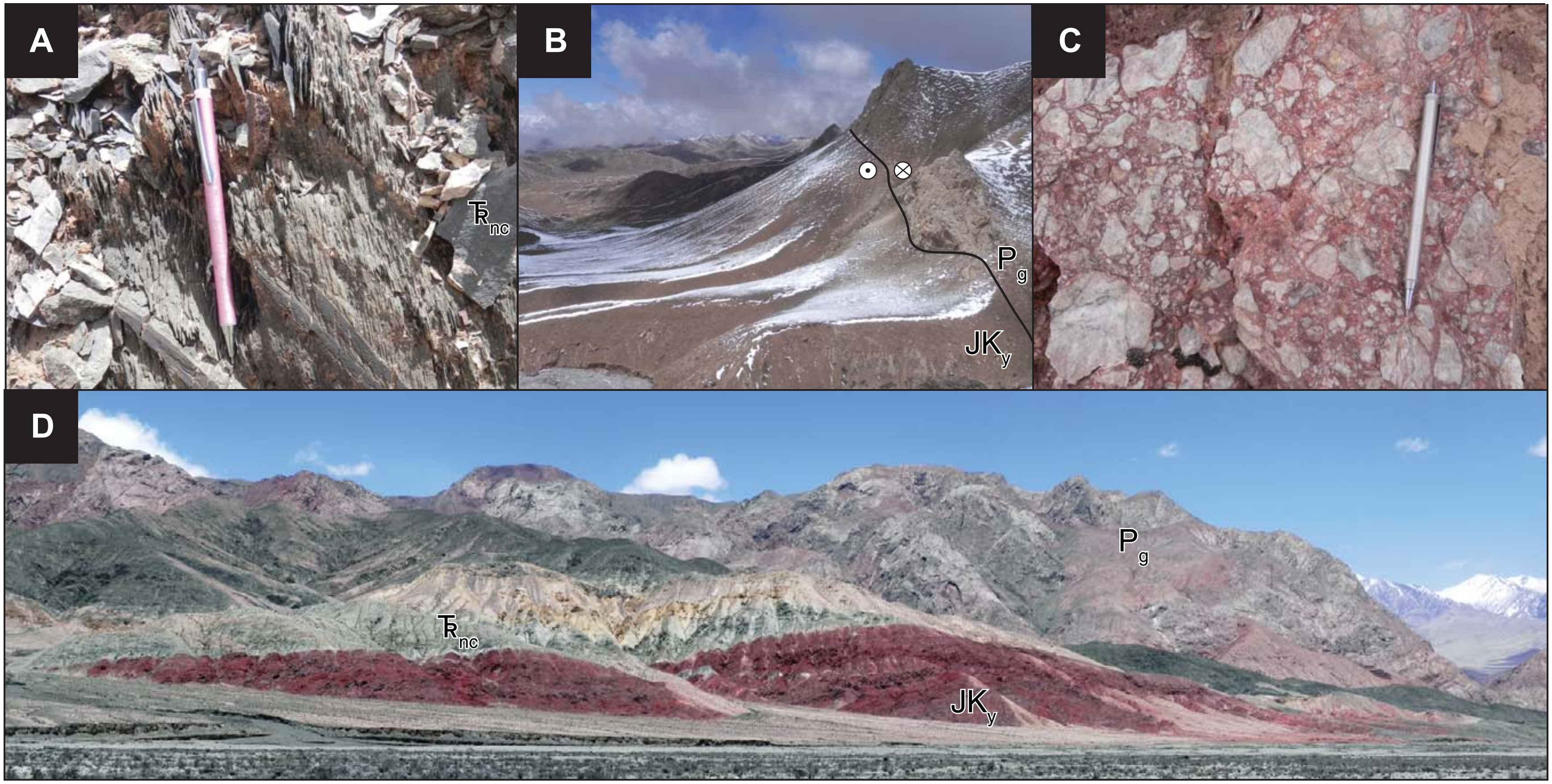
A
Ŧ$_{nc}$
B
P$_g$
JK$_y$
C
D
P$_g$
Ŧ$_{nc}$
JK$_y$

**Figure 6.**

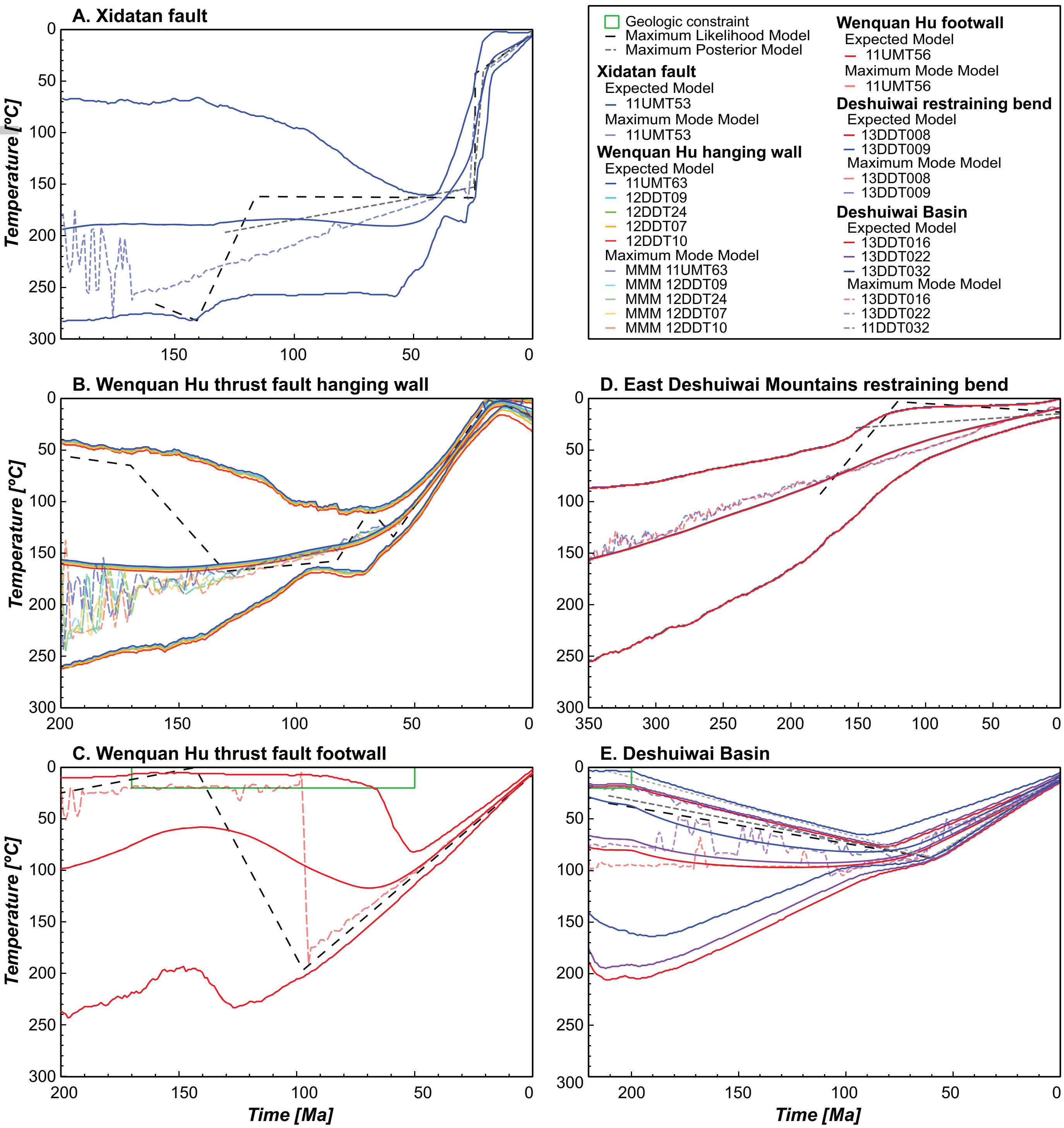
A. Xidatan fault
B. Wenquan Hu thrust fault hanging wall
C. Wenquan Hu thrust fault footwall
D. East Deshuiwai Mountains restraining bend
E. Deshuiwai Basin
Temperature [ºC]
Time [Ma]
Geologic constraint
Maximum Likelihood Model
Maximum Posterior Model
Xidatan fault
Expected Model
11UMT53
Maximum Mode Model
11UMT53
Wenquan Hu hanging wall
Expected Model
11UMT63
12DDT09
12DDT24
12DDT07
12DDT10
Maximum Mode Model
MMM 11UMT63
MMM 12DDT09
MMM 12DDT24
MMM 12DDT07
MMM 12DDT10
Wenquan Hu footwall
Expected Model
11UMT56
Maximum Mode Model
11UMT56
Deshuiwai restraining bend
Expected Model
13DDT008
13DDT009
Maximum Mode Model
13DDT008
13DDT009
Deshuiwai Basin
Expected Model
13DDT016
13DDT022
13DDT032
Maximum Mode Model
13DDT016
13DDT022
11DDT032

**Figure 7.**

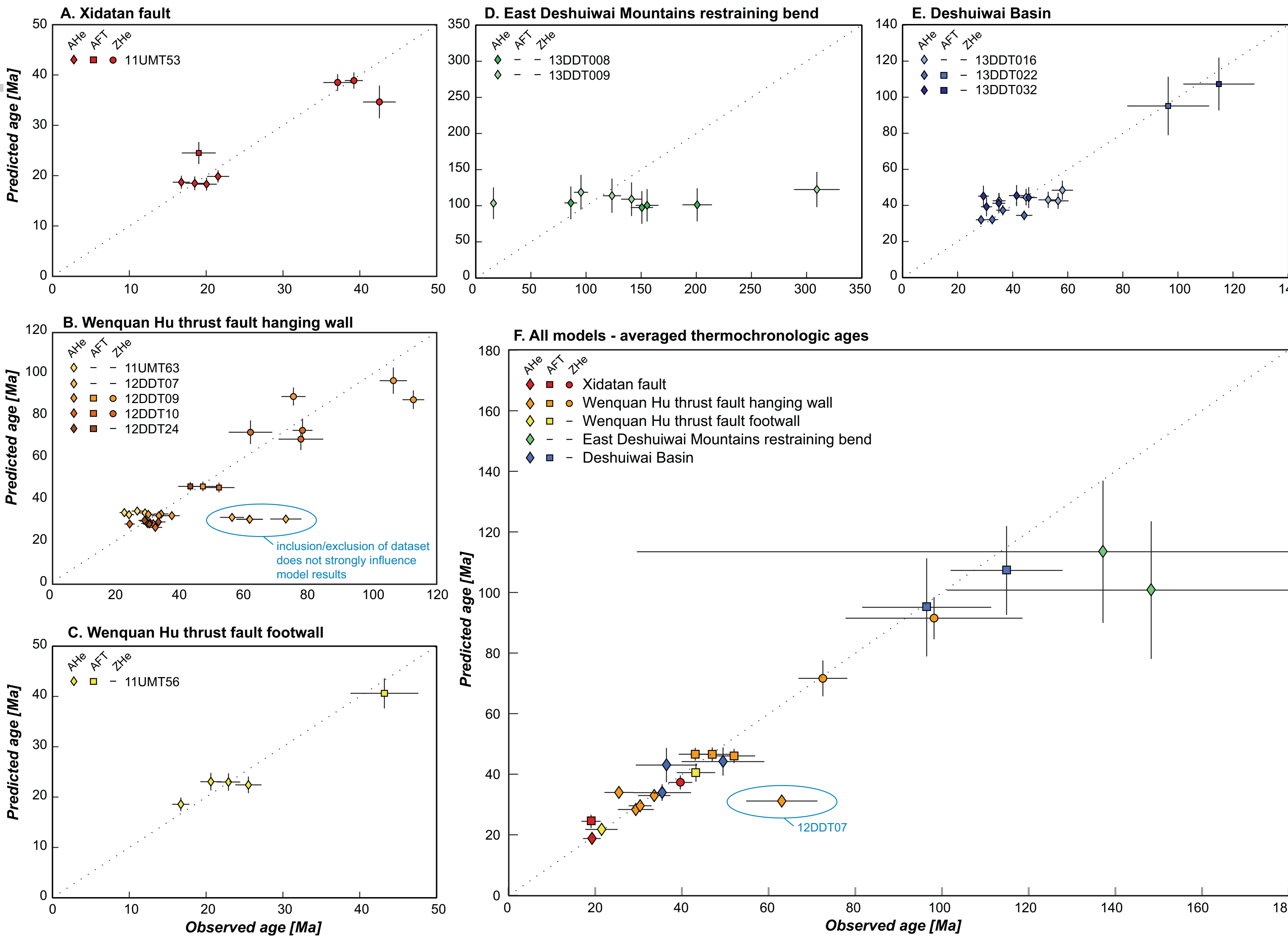

A. Xidatan fault
AHe AFT ZHe
11UMT53
Predicted age [Ma]
D. East Deshuiwai Mountains restraining bend
13DDT008
13DDT009
E. Deshuiwai Basin
13DDT016
13DDT022
13DDT032
B. Wenquan Hu thrust fault hanging wall
11UMT63
12DDT07
12DDT09
12DDT10
12DDT24
inclusion/exclusion of dataset does not strongly influence model results
C. Wenquan Hu thrust fault footwall
11UMT56
Observed age [Ma]
F. All models - averaged thermochronologic ages
Xidatan fault
Wenquan Hu thrust fault hanging wall
Wenquan Hu thrust fault footwall
East Deshuiwai Mountains restraining bend
Deshuiwai Basin
12DDT07

**Figure 8.**

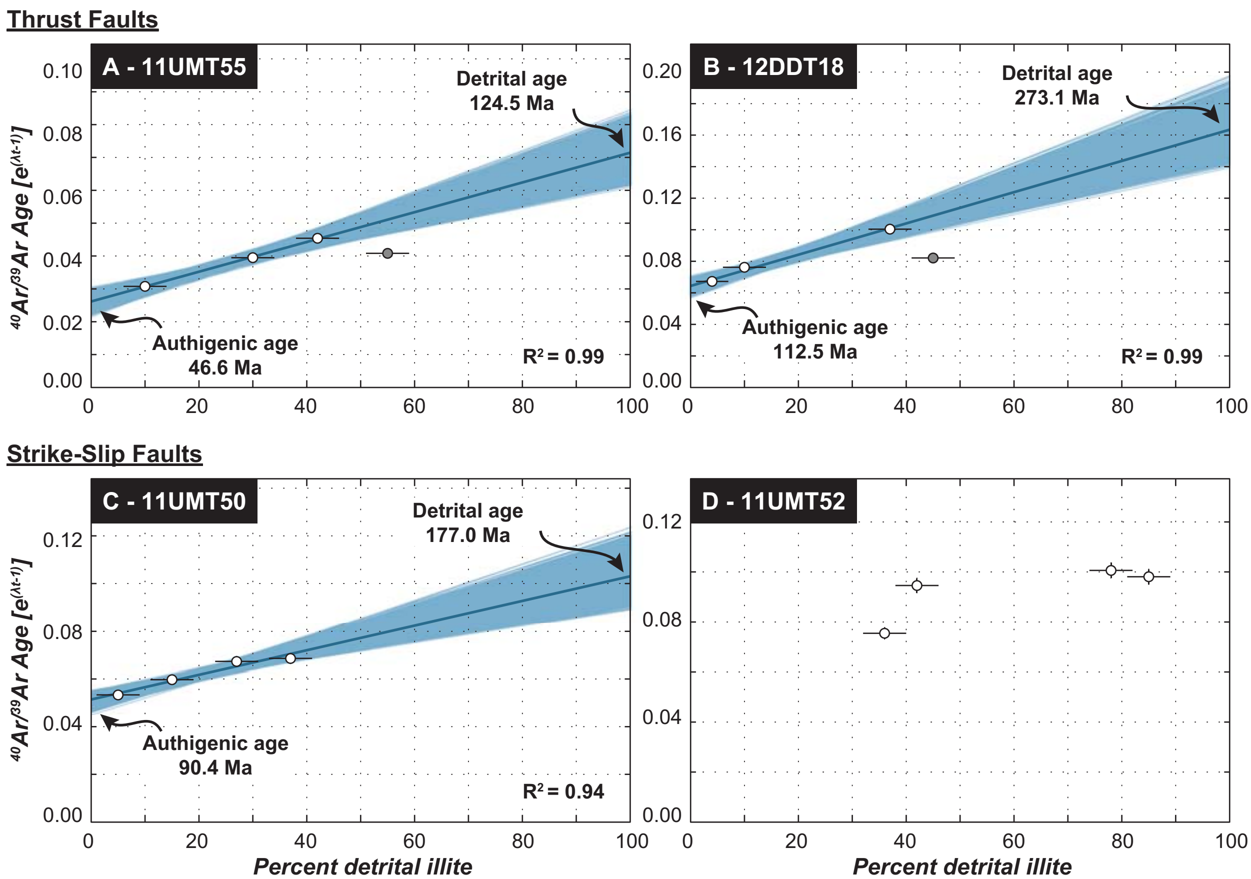

Thrust Faults
A - 11UMT55
Detrital age
124.5 Ma
Authigenic age
46.6 Ma
R² = 0.99
B - 12DDT18
Detrital age
273.1 Ma
Authigenic age
112.5 Ma
R² = 0.99
Strike-Slip Faults
C - 11UMT50
Detrital age
177.0 Ma
Authigenic age
90.4 Ma
R² = 0.94
D - 11UMT52
40Ar/39Ar Age [e^(λt-1)]
Percent detrital illite

**Figure 9.**

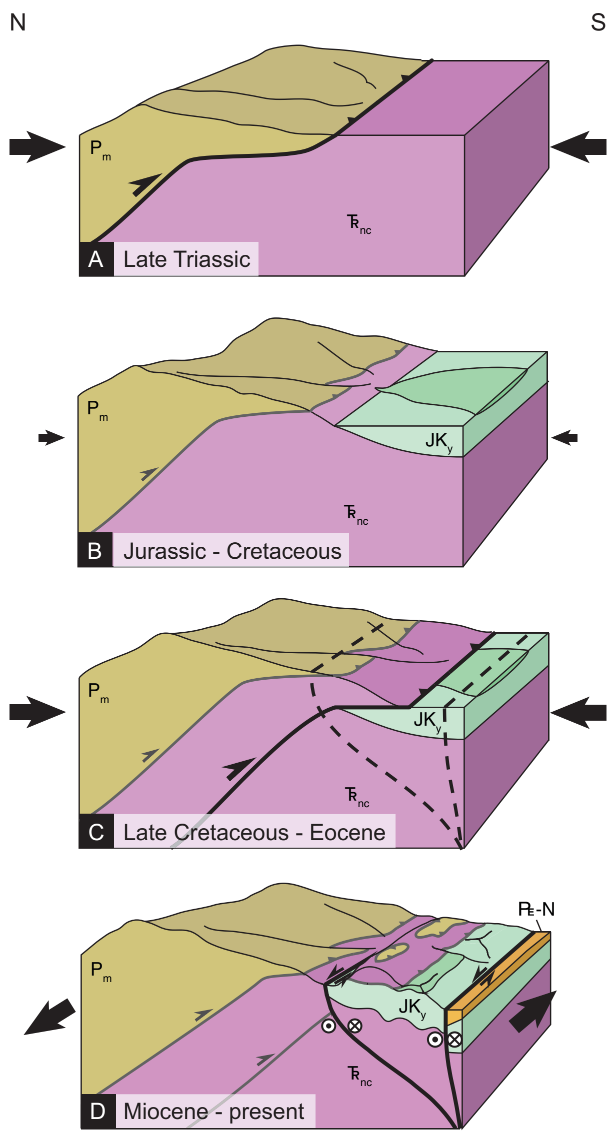

N
S
P m
Ŧ̵R nc
A Late Triassic
P m
JK y
Ŧ̵R nc
B Jurassic - Cretaceous
P m
JK y
Ŧ̵R nc
C Late Cretaceous - Eocene
Pɛ-N
P m
JK y
Ŧ̵R nc
D Miocene - present

**Figure 10.**

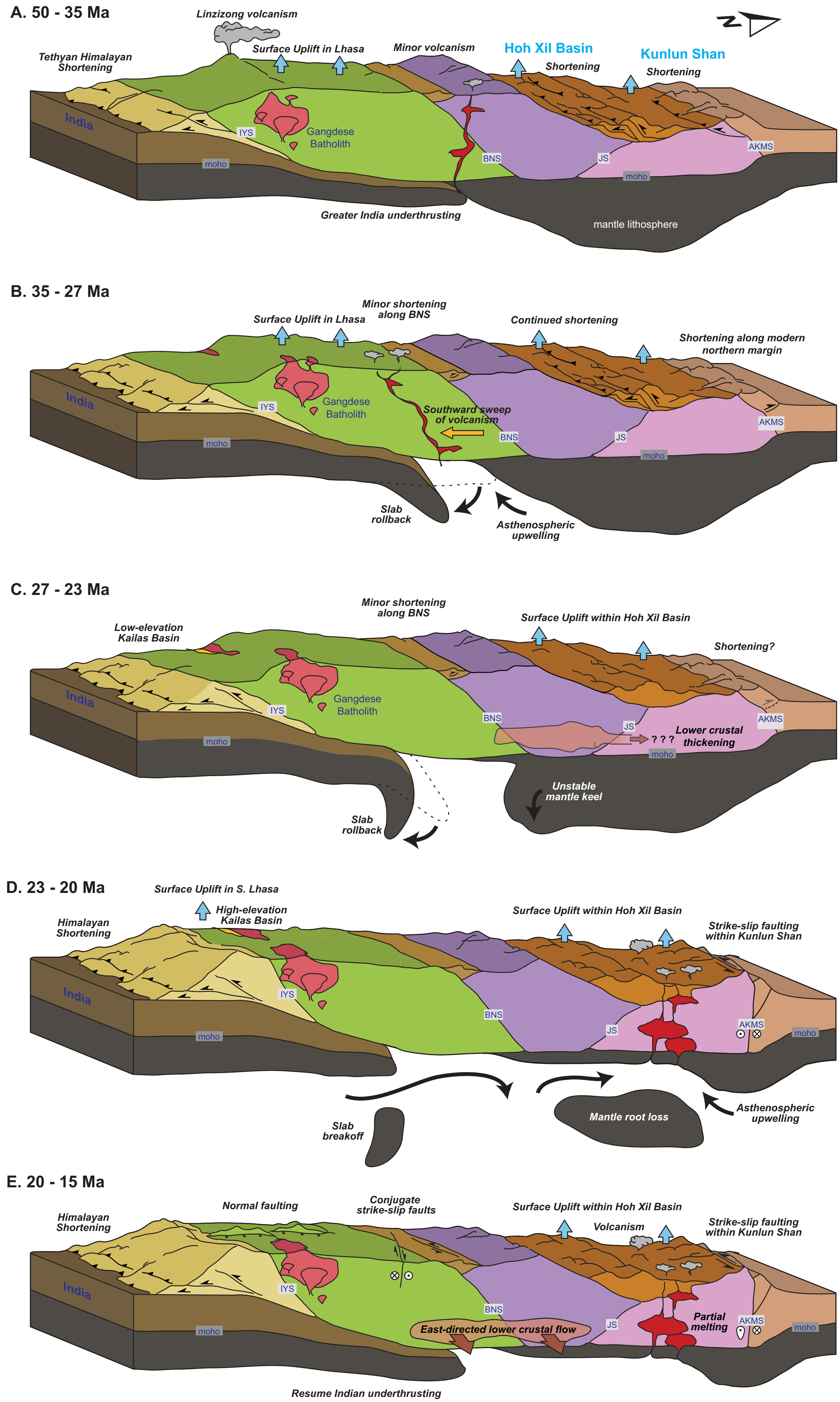
A. 50 - 35 Ma
Linzizong volcanism
Tethyan Himalayan Shortening
Surface Uplift in Lhasa
Minor volcanism
Hoh Xil Basin
Shortening
Kunlun Shan
Shortening
India
IYS
Gangdese Batholith
moho
BNS
JS
AKMS
moho
Greater India underthrusting
mantle lithosphere
B. 35 - 27 Ma
Minor shortening along BNS
Surface Uplift in Lhasa
Continued shortening
Shortening along modern northern margin
India
IYS
Gangdese Batholith
Southward sweep of volcanism
BNS
JS
AKMS
moho
moho
Slab rollback
Asthenospheric upwelling
C. 27 - 23 Ma
Minor shortening along BNS
Low-elevation Kailas Basin
Surface Uplift within Hoh Xil Basin
Shortening?
India
IYS
Gangdese Batholith
BNS
JS
AKMS
Lower crustal thickening
? ? ?
moho
moho
Unstable mantle keel
Slab rollback
D. 23 - 20 Ma
Surface Uplift in S. Lhasa
High-elevation Kailas Basin
Himalayan Shortening
Surface Uplift within Hoh Xil Basin
Strike-slip faulting within Kunlun Shan
India
IYS
BNS
JS
AKMS
moho
moho
Slab breakoff
Mantle root loss
Asthenospheric upwelling
E. 20 - 15 Ma
Himalayan Shortening
Normal faulting
Conjugate strike-slip faults
Surface Uplift within Hoh Xil Basin
Volcanism
Strike-slip faulting within Kunlun Shan
India
IYS
BNS
East-directed lower crustal flow
JS
Partial melting
AKMS
moho
moho
Resume Indian underthrusting

Figure 11.

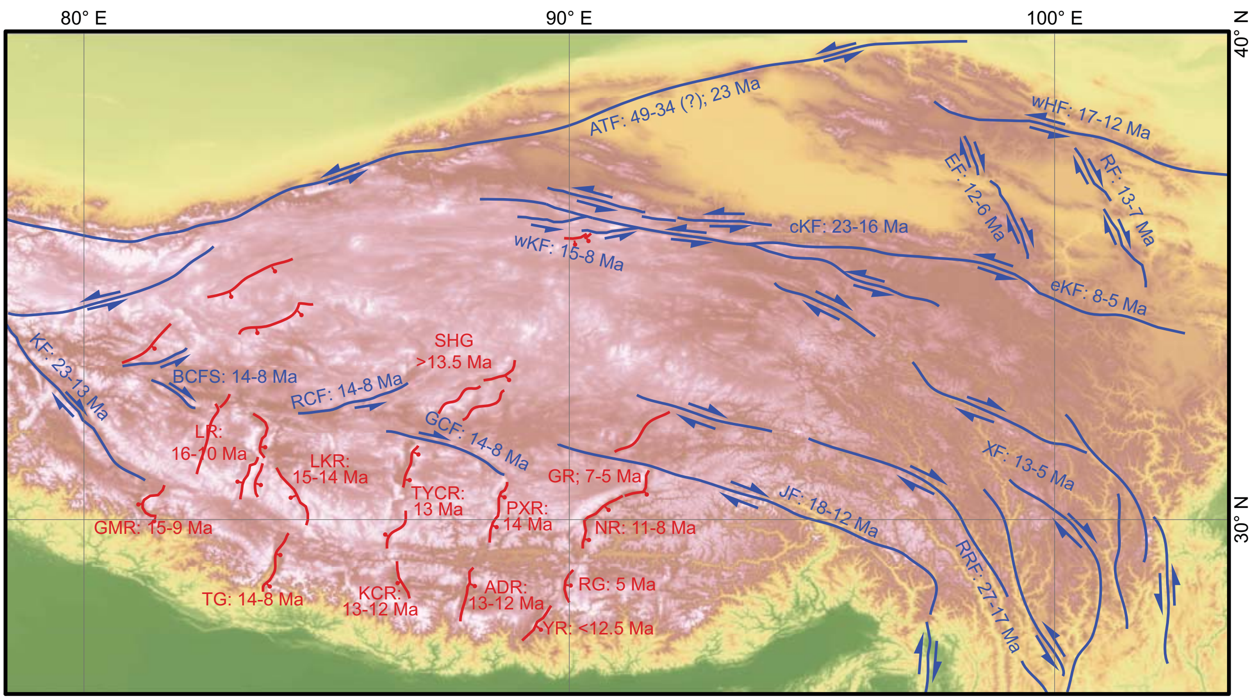
80° E
90° E
100° E
40° N
30° N
ATF: 49-34 (?); 23 Ma
wHF: 17-12 Ma
EF: 12-6 Ma
RF: 13-7 Ma
cKF: 23-16 Ma
wKF: 15-8 Ma
eKF: 8-5 Ma
KF: 23-13 Ma
BCFS: 14-8 Ma
RCF: 14-8 Ma
SHG
>13.5 Ma
GCF: 14-8 Ma
LR:
16-10 Ma
LKR:
15-14 Ma
TYCR:
13 Ma
PXR:
14 Ma
GR; 7-5 Ma
NR: 11-8 Ma
GMR: 15-9 Ma
TG: 14-8 Ma
KCR:
13-12 Ma
ADR:
13-12 Ma
RG: 5 Ma
YR: <12.5 Ma
JF: 18-12 Ma
XF: 13-5 Ma
RRF: 27-17 Ma

**Table 1.** Sample locations, rock type, mean apatite and zircon (U-Th)/He ages, and pooled apatite the central Kunlun Shan. All uncertainties are standard deviation reported at 1σ.

| Sample | Unit and rock type | Sample location: Latitude [°] | Sample location: Longitude [°] | Sample location: Elevation [m] | Apatite (U-Th)/He [Ma] | |
|---|---|---|---|---|---|---|
| Xidatan fault block | | | | | | |
| 11UMT53 | ^$^{3}$Bd - granitic gneiss | 35.7490 | 95.0279 | 4241 | 19.22 ± 2.05 | |
| Wenquan Hu thust fault hanging wall | | | | | | |
| 11UMT63 | Xγδ - granodioritic gneis | 35.7630 | 95.2880 | 4124 | 25.42 ± 2.85 | |
| 12DDT07 | ^nc - granitic gneiss | 35.7740 | 95.3305 | 4026 | 63.02 ± 7.06 | ‡ |
| 12DDT09 | ^nc - gneiss | 35.7626 | 95.2999 | 4068 | 33.58 ± 3.01 | |
| 12DDT10 | ^nc - gneiss | 35.7680 | 95.2556 | 3946 | 29.32 ± 3.64 | |
| 12DDT24 | ^nc - gneiss | 35.7523 | 95.2014 | 4063 | 30.33 ± 1.69 | |
| Wenquan Hu thust fault footwall | | | | | | |
| 11UMT56 | JKy - sandstone | 35.7563 | 95.2258 | 4046 | 21.45 ± 3.73 | |
| East Deshuiwai Mountains restraining bend | | | | | | |
| 13DDT008 | ^3b - metavolcanic | 35.8779 | 95.7872 | 4542 | 148.27 ± 47.13 | † |
| 13DDT009 | ^$^{3}$b - arkose | 35.8714 | 95.7877 | 4558 | 137.13 ± 107.52 | † |
| Deshuiwai Basin | | | | | | |
| 13DDT016 | ^$^{3}$b - arkose | 35.8255 | 96.4173 | 3929 | 49.48 ± 9.53 | ‡ |
| 13DDT022 | ^$^{2}$Yg - granodiorite | 35.8880 | 96.4496 | 4123 | 35.42 ± 6.67 | ‡ |
| 13DDT032 | < - andesitic dike | 35.9095 | 96.1664 | 4752 | 36.42 ± 7.07 | |
| Other samples | | | | | | |
| 12DDT17 | JKy - volcanic | 35.7639 | 95.2836 | 4084 | 37.38 ± 6.02 | * |
| 12DDT22 | ^$^{3}$b - sandstone | 35.9404 | 95.2364 | 4691 | 38.30 ± 9.96 | * |
| 13DDT011 | Pm - metavolcanic | 35.6320 | 96.2459 | 4916 | 31.84 ± 4.13 | |
| 13DDT017 | ^nc - tonalitic intrusion | 35.6688 | 96.0487 | 4373 | 75.76 ± 25.72 | ‡ |
| 13DDT021 | ^2Yg - granitoid float | 35.8880 | 96.4496 | 4123 | 50.75 ± 7.05 | |
| 13DDT023 | ^$^{2}$Yg - granodiorite | 35.8708 | 96.4514 | 4053 | 54.13 ± 15.63 | * |
| 13DDT036 | P$^{2}$L - granite | 35.9126 | 96.3012 | 4538 | 73.13 ± 42.75 | * |

* Helium analyses exhibit poor reproducibility (standard deviation > 20%) that cannot be attributed tc
‡ indicates correlation between the AHe age and eU (correlation coefficient > 0.85), possibly residec
† indicates correlation between AHe age and grain size (correlation coefficient > 0.99), possibly resi

fission-track ages for samples collected from

| Apatite fission-track [Ma] | Zircon (U-Th)/He [Ma] | |
|---|---|---|
| 19.04 ± 2.21 | 39.63 ± 2.75 | |
| - | - | |
| - | - | |
| 46.97 ± 5.07 | 98.14 ± 20.06 | * |
| 52.00 ± 4.84 | 72.50 ± 9.24 | |
| 43.04 ± 3.80 | - | |
| 43.22 ± 4.42 | 256.61 ± 59.27 | * |
| - | - | |
| - | - | |
| - | - | |
| 96.47 ± 14.88 | - | |
| 114.89 ± 12.93 | - | |
| - | 140.04 ± 12.43 | |
| - | 97.05 ± 11.62 | |
| 64.43 ± 12.77 | - | |
| - | - | |
| - | - | |
| - | - | |
| - | - | |

ɔ age-eU or age-grain size correlations
ɖ within PRZ for some time
ded within PRZ

**Table 2**. QTQt thermochronologic modeling inputs and reasoning

| Fault Block | Samples | Thermochronologic data input | Geologic constraint |
|---|---|---|---|
| Xidatan fault | 11UMT53 | AHe, AFT, ZHe ages | 0-20°C by 0 Ma;<br>Maximum cooling rate 1000 °C/Myr |
| Wenquan Hu thrust fault hanging wall | 11UMT63<br>12DDT07<br>12DDT09<br>12DDT10<br>12DDT24 | AHe, AFT, ZHe ages;<br>AFT track lengths | 0-20°C by 0 Ma;<br>Maximum cooling rate 1000 °C/Myr |
| Wenquan Hu thrust fault footwall | 11UMT56<br>12DDT17 | AHe, AFT ages | 0-20°C @ 170-50 Ma;<br>0-20°C by 0 Ma;<br>Maximum cooling rate 1000 °C/Myr |
| East Deshuiwai Mountains restraining bend | 13DDT008<br>13DDT009 | AHe ages | 0-20°C by 0 Ma;<br>Maximum cooling rate 1000 °C/Myr |
| Deshuiwai Basin | 13DDT016<br>13DDT022<br>13DDT032 | AHe, AFT ages | 0-20°C @ 250-200 Ma;<br>0-20°C by 0 Ma;<br>Maximum cooling rate 1000 °C/Myr |

| Supporting Observation |
| --- |
| Sample collected from gneiss body (small pluton intruded into Triassic Naocangjianguo Group) directly north of the Xidatan fault in Dongdatan Valley. All thermochronologic ages appear reset. |
| Samples collected from metamorphosed plutonic bodies emplaced within the Triassic Naocangjianguo Group in the hanging wall of the Wenquan Hu thrust fault. All thermochronologic ages appear reset. |
| Samples collected from the Yangqu Group strata in the footwall of the Wenquan Hu thrust fault. AHe and AFT ages appear reset. ZHe ages are interpreted as either detrital ages (11UMT56) or volcanic emplacement ages (12DDT17). Terrestrial deposition, at surface temperatures, loosely constrained between middle to late Jurassic and Eocene time. |
| Samples collected from the restraining bend between Wenquan and Deshuiwai Basins. Both samples show significant scatter in ages and correlation between AHe age and apatite grain size, suggesting slow cooling and variable He diffusion. |
| Samples collected from Triassic sedimentary and igneous in the East Deshuiwai Basin. Sample 13DDT16 collected from the upper Triassic Babaoshan Group. Terrestrial deposition, at surface temperatures, constrained during upper Triassic time. |

| Range for general prior |
| --- |
| 0-300°C and 0-300 Ma |
| 0-300°C and 0-300 Ma |
| 0-300°C and 0-300 Ma |
| 0-300°C and 0-300 Ma |
| 0-300°C and 0-300 Ma |

**Table 3.** Fault gouge data from thrust and strike-slip faults sampled in the Dongdatan Valley

| Sample | Size fraction [μm] | $^{40}Ar/^{39}Ar$ age [Ma] | Proportion $2M_1$ [%] | F-recoil [%] |
|---|---|---|---|---|
| 11UMT50 | | | | |
| | 1.0 - 2.0 | 119.76 ± 0.52 | 37 ± 4 | 17.2 |
| | 0.5 - 1.0 | 117.62 ± 0.71 | 27 ± 4 | 15.0 |
| | 0.2 - 0.5 | 104.58 ± 0.39 | 15 ± 4 | 18.8 |
| | 0.05 - 0.2 | 93.75 ± 0.33 | 5 ± 4 | 21.9 |
| 11UMT52 | | | | |
| | 1.0 - 2.0 | 168.77 ± 1.17 | 85 ± 4 | 10.1 |
| | 0.5 - 1.0 | 172.92 ± 0.78 | 78 ± 4 | 8.1 |
| | 0.2 - 0.5 | 163.05 ± 0.45 | 42 ± 4 | 10.1 |
| | 0.05 - 0.2 | 131.30 ± 0.41 | 36 ± 4 | 24.6 |
| 11UMT52 | | | | |
| | 1.0 - 2.0 | 72.17 ± 0.40 | 55 ± 4 | 14.8 |
| | 0.5 - 1.0 | 80.09 ± 0.59 | 42 ± 4 | 13.0 |
| | 0.2 - 0.5 | 69.86 ± 0.61 | 30 ± 4 | 15.5 |
| | 0.05 - 0.2 | 54.65 ± 0.21 | 10 ± 4 | 21.7 |
| 12DDT18 | | | | |
| | 1.0 - 2.0 | 142.39 ± 0.87 | 45 ± 4 | 20.3 |
| | 0.5 - 1.0 | 172.61 ± 0.64 | 37 ± 4 | 11.9 |
| | 0.2 - 0.5 | 132.52 ± 0.50 | 10 ± 4 | 21.6 |
| | < 0.05 | 117.35 ± 0.53 | 4 ± 4 | 23.7 |

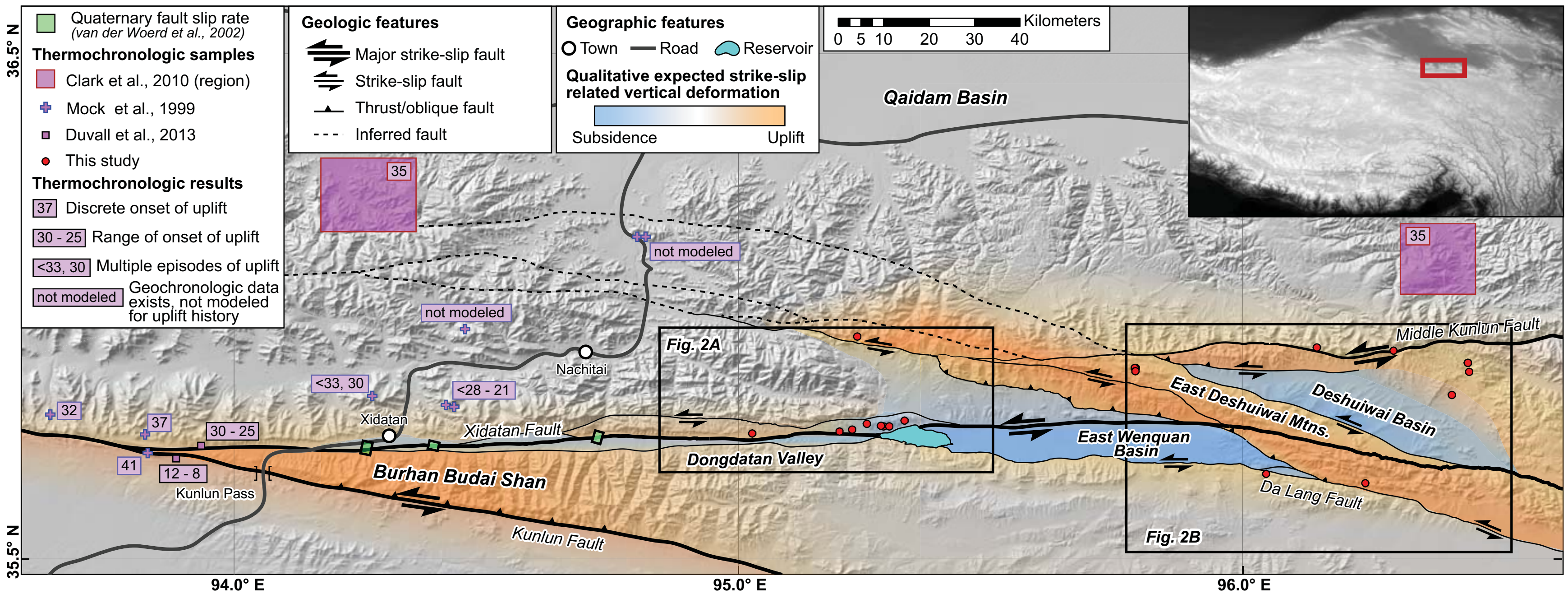

Quaternary fault slip rate
(van der Woerd et al., 2002)
Thermochronologic samples
Clark et al., 2010 (region)
Mock et al., 1999
Duvall et al., 2013
This study
Thermochronologic results
37 Discrete onset of uplift
30 - 25 Range of onset of uplift
<33, 30 Multiple episodes of uplift
not modeled Geochronologic data exists, not modeled for uplift history
Geologic features
Major strike-slip fault
Strike-slip fault
Thrust/oblique fault
Inferred fault
Geographic features
Town
Road
Reservoir
Qualitative expected strike-slip related vertical deformation
Subsidence
Uplift
0 5 10 20 30 40 Kilometers
Qaidam Basin
Nachitai
Xidatan
Xidatan Fault
Kunlun Pass
Burhan Budai Shan
Kunlun Fault
Fig. 2A
Dongdatan Valley
East Wenquan Basin
East Deshuiwai Mtns.
Deshuiwai Basin
Middle Kunlun Fault
Da Lang Fault
Fig. 2B
36.5° N
35.5° N
94.0° E
95.0° E
96.0° E

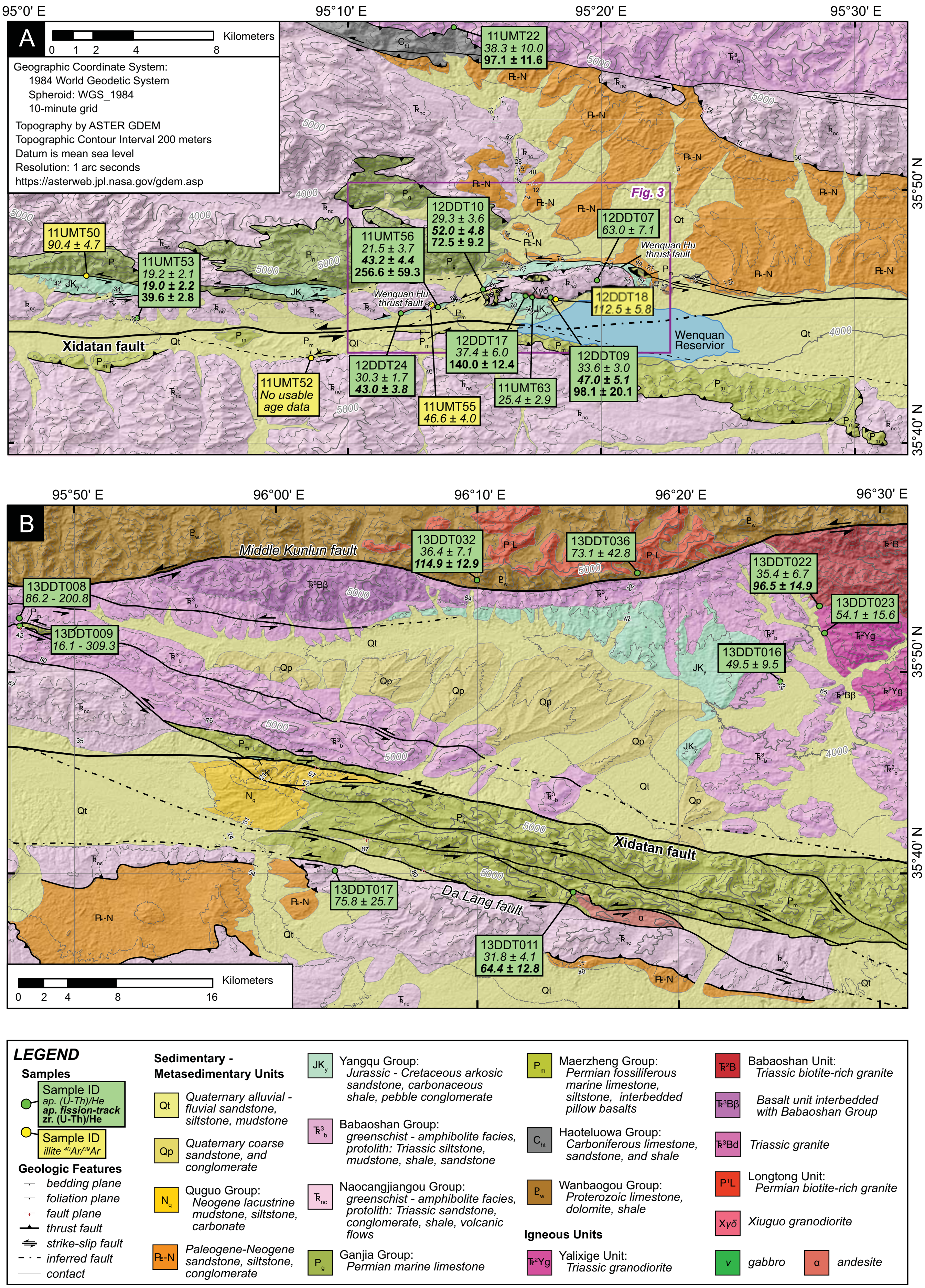
A
B
95°0' E
95°10' E
95°20' E
95°30' E
35°50' N
35°40' N
Kilometers
Geographic Coordinate System:
1984 World Geodetic System
Spheroid: WGS_1984
10-minute grid
Topography by ASTER GDEM
Topographic Contour Interval 200 meters
Datum is mean sea level
Resolution: 1 arc seconds
https://asterweb.jpl.nasa.gov/gdem.asp
Fig. 3
11UMT22 38.3 ± 10.0 97.1 ± 11.6
11UMT50 90.4 ± 4.7
11UMT53 19.2 ± 2.1 19.0 ± 2.2 39.6 ± 2.8
11UMT56 21.5 ± 3.7 43.2 ± 4.4 256.6 ± 59.3
12DDT10 29.3 ± 3.6 52.0 ± 4.8 72.5 ± 9.2
12DDT07 63.0 ± 7.1
12DDT18 112.5 ± 5.8
12DDT24 30.3 ± 1.7 43.0 ± 3.8
12DDT17 37.4 ± 6.0 140.0 ± 12.4
12DDT09 33.6 ± 3.0 47.0 ± 5.1 98.1 ± 20.1
11UMT52 No usable age data
11UMT55 46.6 ± 4.0
11UMT63 25.4 ± 2.9
Wenquan Hu thrust fault
Xidatan fault
Wenquan Reservior
95°50' E
96°00' E
96°10' E
96°20' E
96°30' E
Middle Kunlun fault
13DDT032 36.4 ± 7.1 114.9 ± 12.9
13DDT036 73.1 ± 42.8
13DDT022 35.4 ± 6.7 96.5 ± 14.9
13DDT023 54.1 ± 15.6
13DDT008 86.2 - 200.8
13DDT009 16.1 - 309.3
13DDT016 49.5 ± 9.5
13DDT017 75.8 ± 25.7
13DDT011 31.8 ± 4.1 64.4 ± 12.8
Xidatan fault
Da Lang fault
LEGEND
Samples
Sample ID
ap. (U-Th)/He
ap. fission-track
zr. (U-Th)/He
Sample ID
illite 40Ar/39Ar
Geologic Features
bedding plane
foliation plane
fault plane
thrust fault
strike-slip fault
inferred fault
contact
Sedimentary - Metasedimentary Units
Quaternary alluvial - fluvial sandstone, siltstone, mudstone
Quaternary coarse sandstone, and conglomerate
Quguo Group: Neogene lacustrine mudstone, siltstone, carbonate
Paleogene-Neogene sandstone, siltstone, conglomerate
Yangqu Group: Jurassic - Cretaceous arkosic sandstone, carbonaceous shale, pebble conglomerate
Babaoshan Group: greenschist - amphibolite facies, protolith: Triassic siltstone, mudstone, shale, sandstone
Naocangjiangou Group: greenschist - amphibolite facies, protolith: Triassic sandstone, conglomerate, shale, volcanic flows
Ganjia Group: Permian marine limestone
Maerzheng Group: Permian fossiliferous marine limestone, siltstone, interbedded pillow basalts
Haoteluowa Group: Carboniferous limestone, sandstone, and shale
Wanbaogou Group: Proterozoic limestone, dolomite, shale
Igneous Units
Yalixige Unit: Triassic granodiorite
Babaoshan Unit: Triassic biotite-rich granite
Basalt unit interbedded with Babaoshan Group
Triassic granite
Longtong Unit: Permian biotite-rich granite
Xiuguo granodiorite
gabbro
andesite

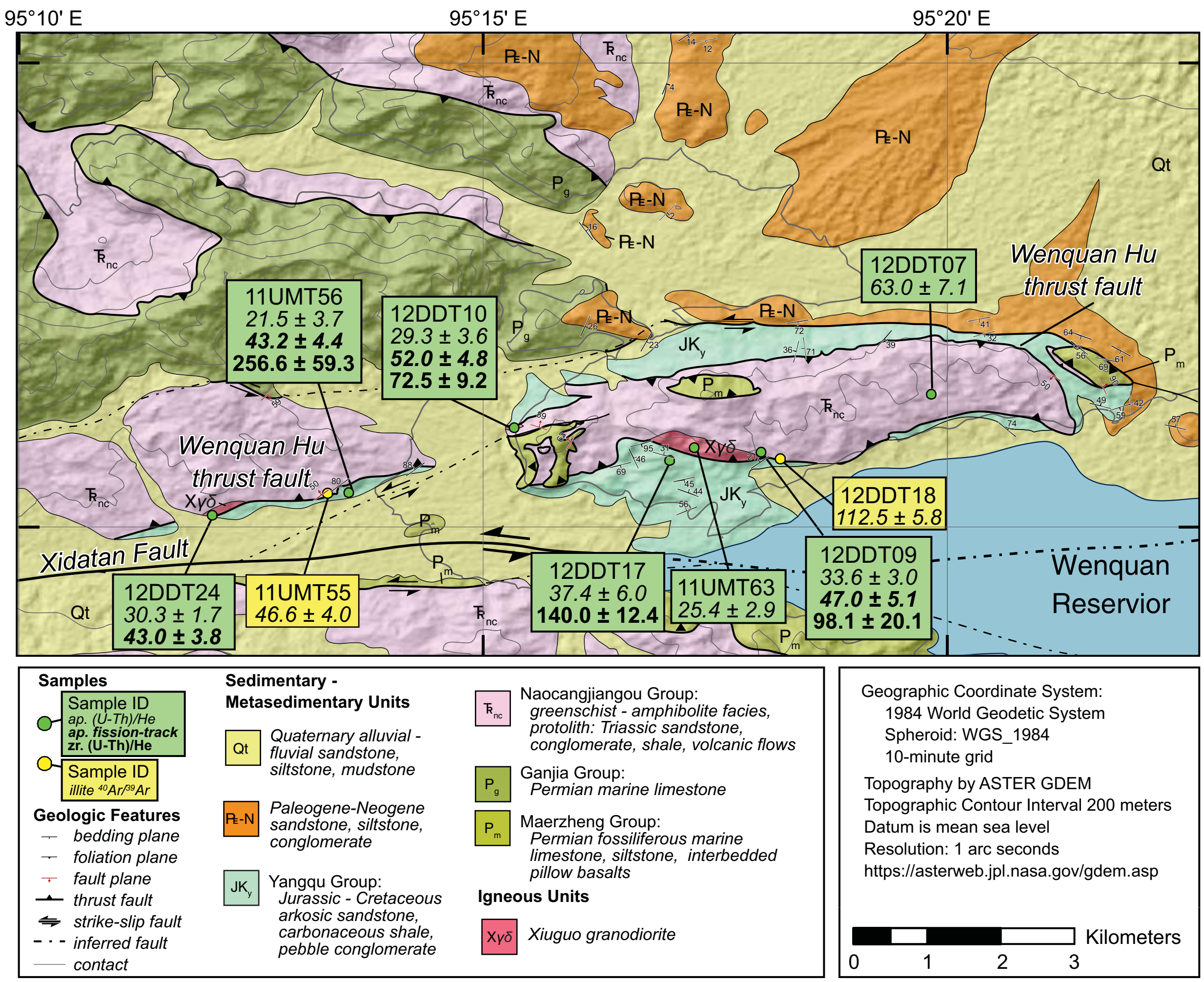

95°10' E
95°15' E
95°20' E
35°50' N
35°45' N
Wenquan Hu thrust fault
Wenquan Hu thrust fault
Xidatan Fault
Wenquan Reservior
11UMT56
21.5 ± 3.7
43.2 ± 4.4
256.6 ± 59.3
12DDT10
29.3 ± 3.6
52.0 ± 4.8
72.5 ± 9.2
12DDT07
63.0 ± 7.1
12DDT18
112.5 ± 5.8
12DDT09
33.6 ± 3.0
47.0 ± 5.1
98.1 ± 20.1
11UMT63
25.4 ± 2.9
12DDT17
37.4 ± 6.0
140.0 ± 12.4
11UMT55
46.6 ± 4.0
12DDT24
30.3 ± 1.7
43.0 ± 3.8
Samples
Sample ID
ap. (U-Th)/He
ap. fission-track
zr. (U-Th)/He
Sample ID
illite 40Ar/39Ar
Geologic Features
bedding plane
foliation plane
fault plane
thrust fault
strike-slip fault
inferred fault
contact
Sedimentary - Metasedimentary Units
Qt
Quaternary alluvial - fluvial sandstone, siltstone, mudstone
Pε-N
Paleogene-Neogene sandstone, siltstone, conglomerate
JKy
Yangqu Group: Jurassic - Cretaceous arkosic sandstone, carbonaceous shale, pebble conglomerate
Tnc
Naocangjiangou Group: greenschist - amphibolite facies, protolith: Triassic sandstone, conglomerate, shale, volcanic flows
Pg
Ganjia Group: Permian marine limestone
Pm
Maerzheng Group: Permian fossiliferous marine limestone, siltstone, interbedded pillow basalts
Igneous Units
Xγδ
Xiuguo granodiorite
Geographic Coordinate System:
1984 World Geodetic System
Spheroid: WGS_1984
10-minute grid
Topography by ASTER GDEM
Topographic Contour Interval 200 meters
Datum is mean sea level
Resolution: 1 arc seconds
https://asterweb.jpl.nasa.gov/gdem.asp
Kilometers
0
1
2
3

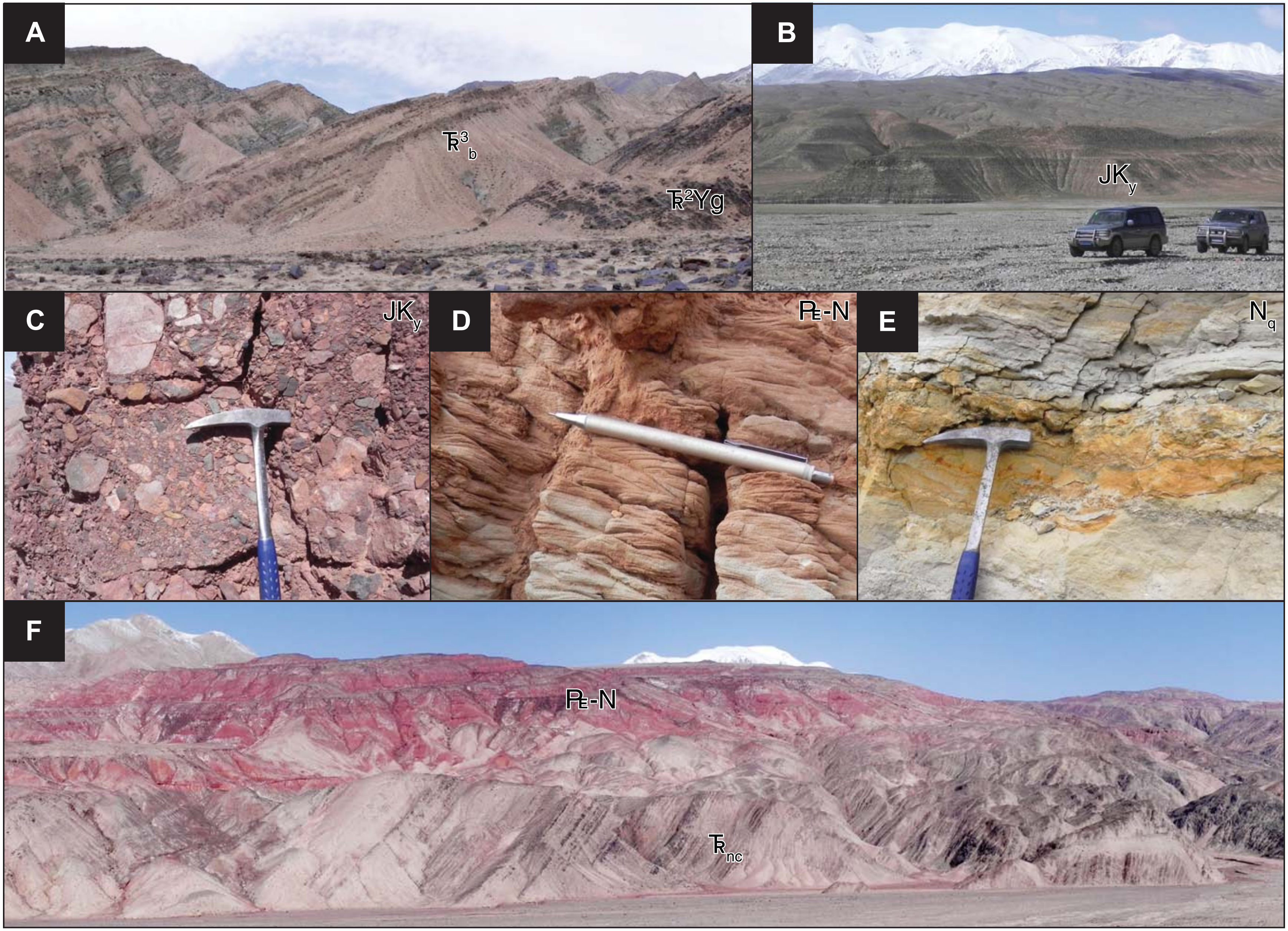
A
Ꞧ³b
Ꞧ²Yg
B
JKy
C
JKy
D
Pε-N
E
Nq
F
Pε-N
Ꞧnc

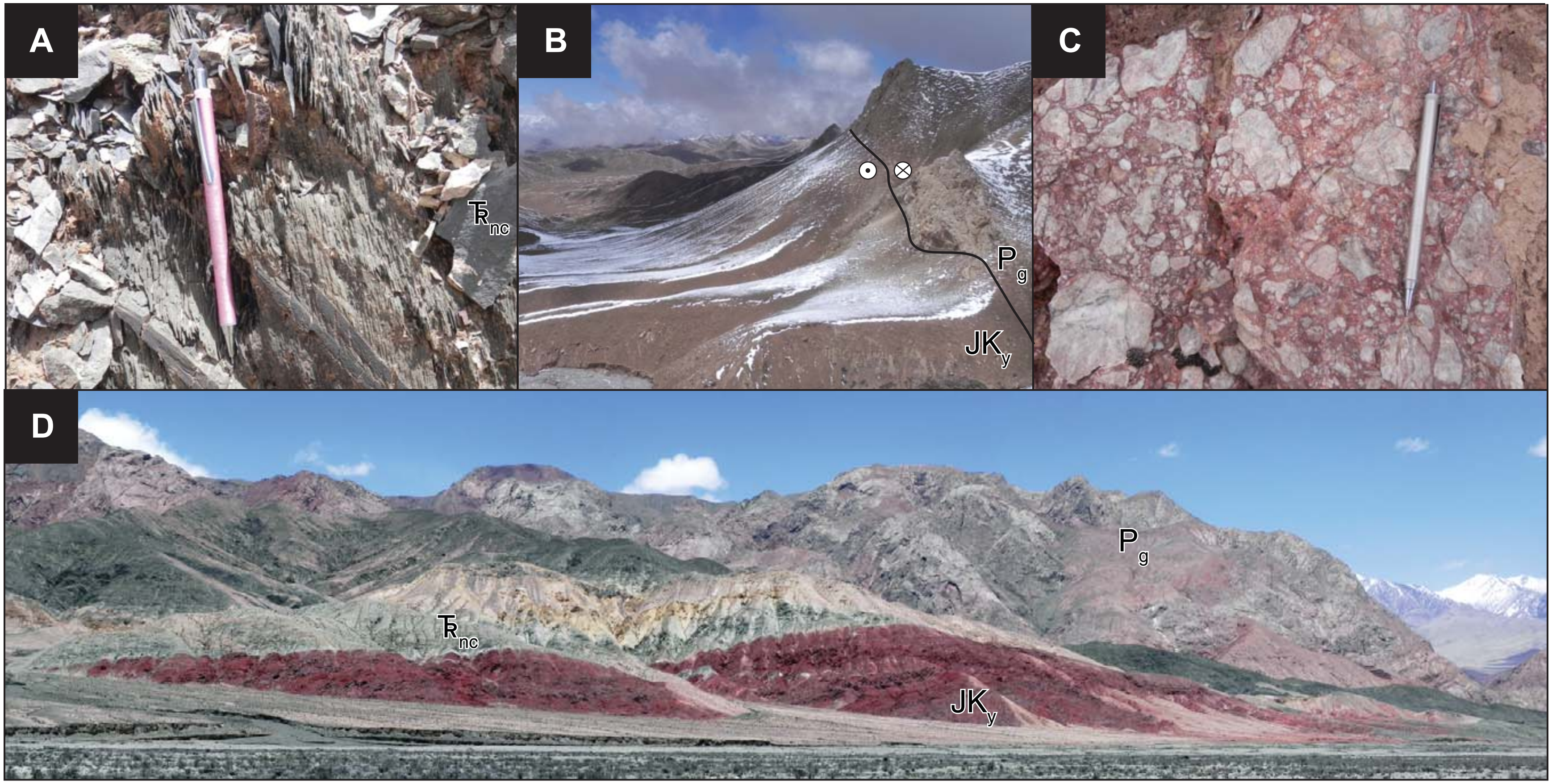
A
Ŧ$_{nc}$
B
P$_g$
JK$_y$
C
D
P$_g$
Ŧ$_{nc}$
JK$_y$

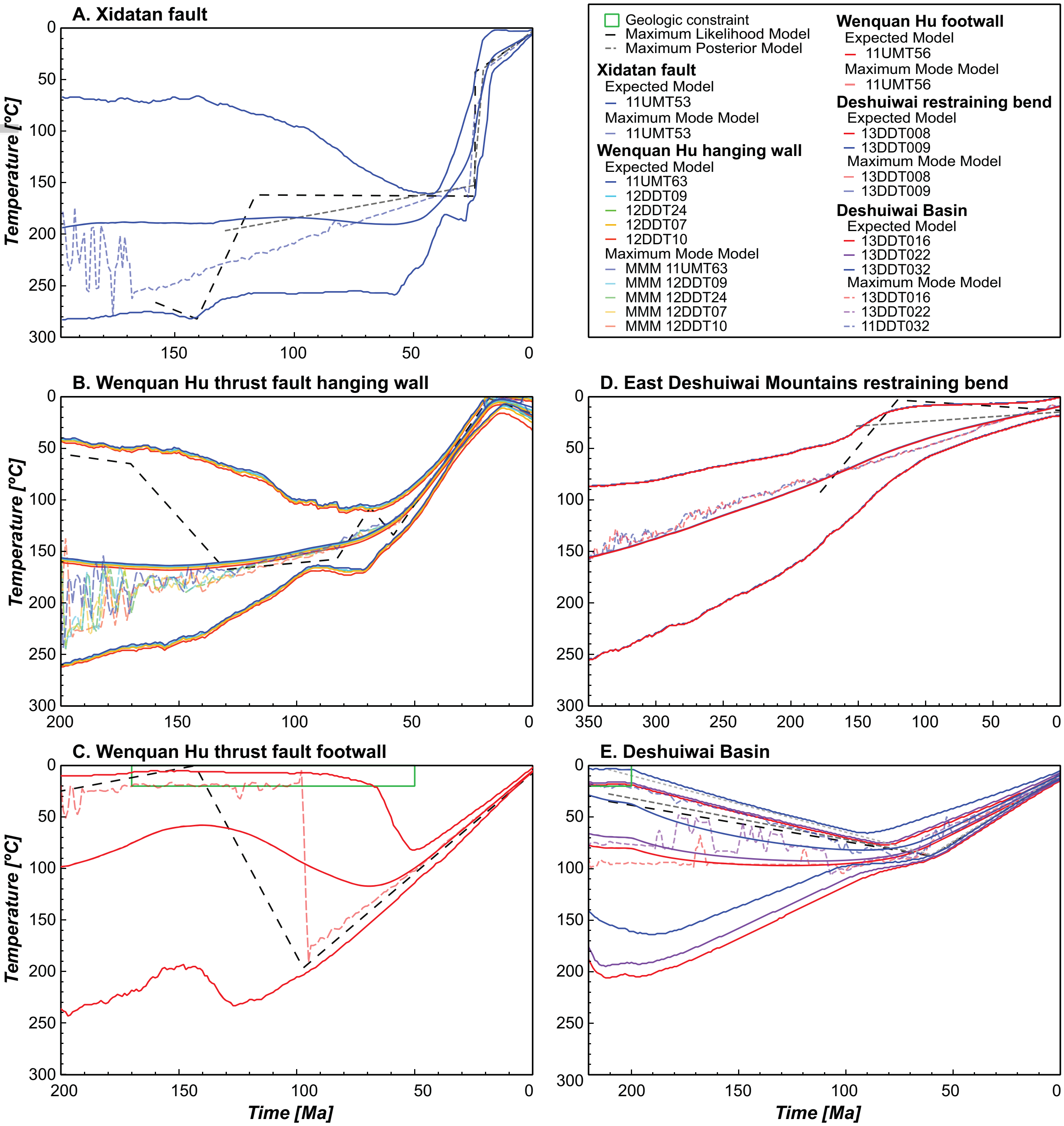

A. Xidatan fault
B. Wenquan Hu thrust fault hanging wall
C. Wenquan Hu thrust fault footwall
D. East Deshuiwai Mountains restraining bend
E. Deshuiwai Basin
Temperature [ºC]
Time [Ma]
Geologic constraint
Maximum Likelihood Model
Maximum Posterior Model
Xidatan fault
Expected Model
11UMT53
Maximum Mode Model
11UMT53
Wenquan Hu hanging wall
Expected Model
11UMT63
12DDT09
12DDT24
12DDT07
12DDT10
Maximum Mode Model
MMM 11UMT63
MMM 12DDT09
MMM 12DDT24
MMM 12DDT07
MMM 12DDT10
Wenquan Hu footwall
Expected Model
11UMT56
Maximum Mode Model
11UMT56
Deshuiwai restraining bend
Expected Model
13DDT008
13DDT009
Maximum Mode Model
13DDT008
13DDT009
Deshuiwai Basin
Expected Model
13DDT016
13DDT022
13DDT032
Maximum Mode Model
13DDT016
13DDT022
11DDT032

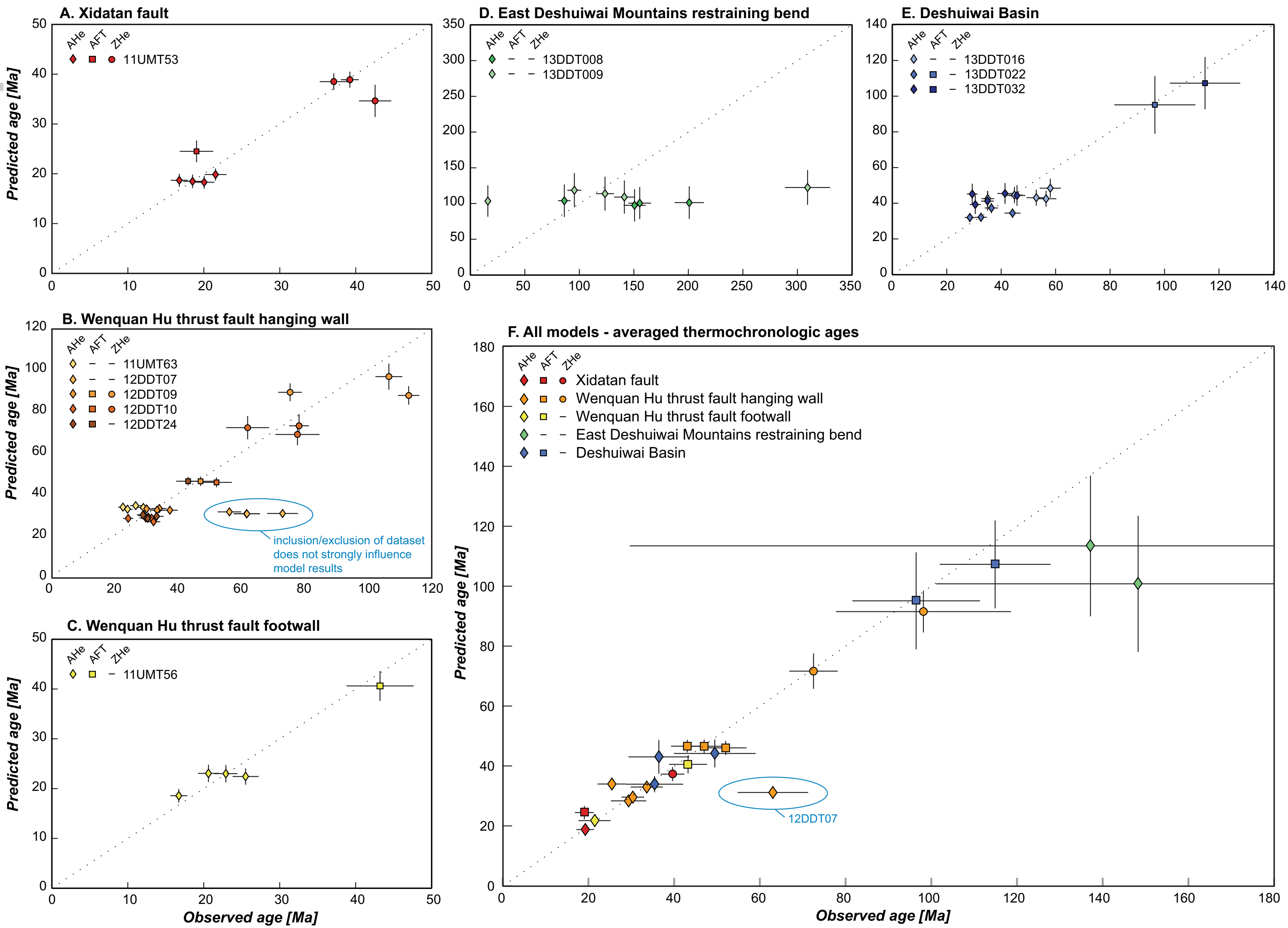
A. Xidatan fault
AHe AFT ZHe
11UMT53
D. East Deshuiwai Mountains restraining bend
13DDT008
13DDT009
E. Deshuiwai Basin
13DDT016
13DDT022
13DDT032
B. Wenquan Hu thrust fault hanging wall
11UMT63
12DDT07
12DDT09
12DDT10
12DDT24
inclusion/exclusion of dataset does not strongly influence model results
C. Wenquan Hu thrust fault footwall
11UMT56
F. All models - averaged thermochronologic ages
Xidatan fault
Wenquan Hu thrust fault hanging wall
Wenquan Hu thrust fault footwall
East Deshuiwai Mountains restraining bend
Deshuiwai Basin
12DDT07
Predicted age [Ma]
Observed age [Ma]

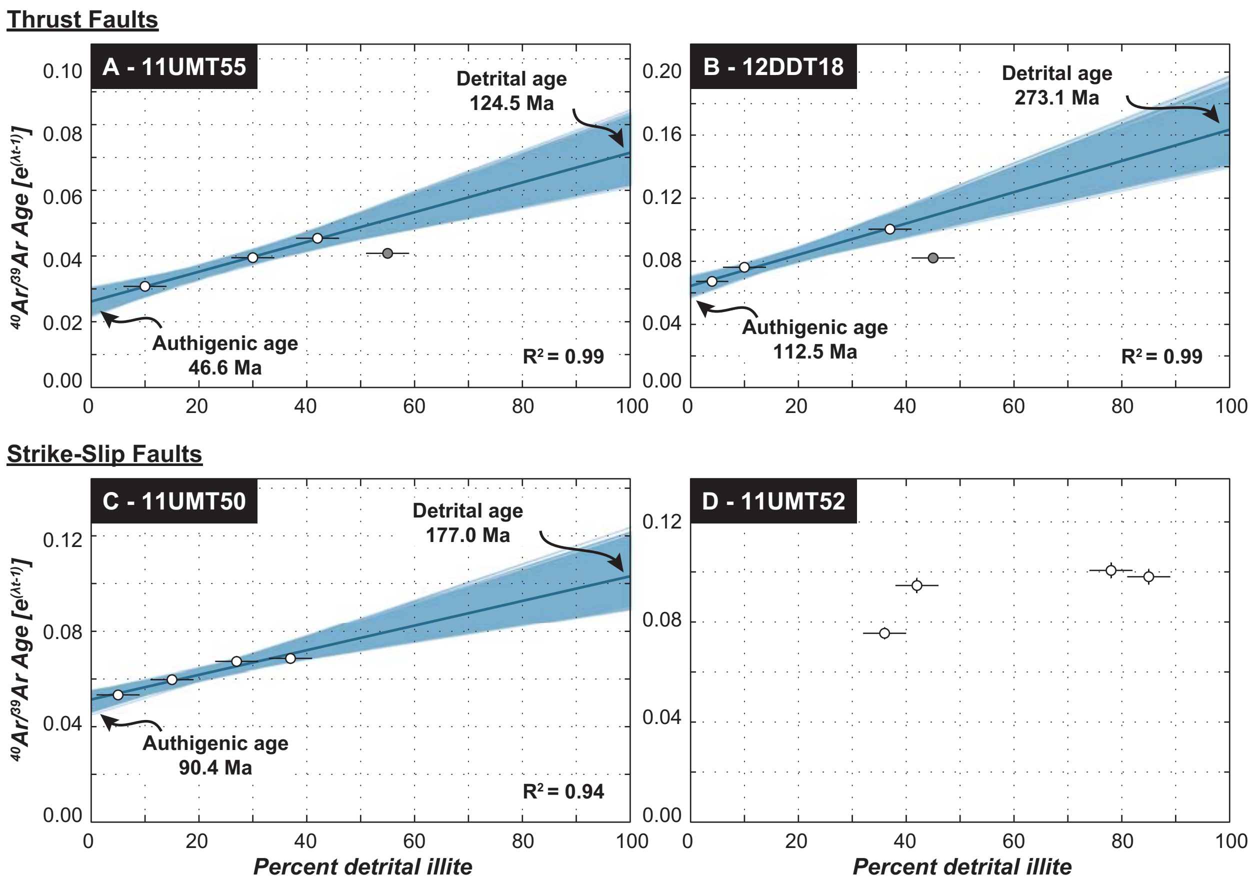
Thrust Faults
A - 11UMT55
Detrital age
124.5 Ma
Authigenic age
46.6 Ma
R² = 0.99
B - 12DDT18
Detrital age
273.1 Ma
Authigenic age
112.5 Ma
R² = 0.99
Strike-Slip Faults
C - 11UMT50
Detrital age
177.0 Ma
Authigenic age
90.4 Ma
R² = 0.94
D - 11UMT52
40Ar/39Ar Age [e^(λt-1)]
Percent detrital illite

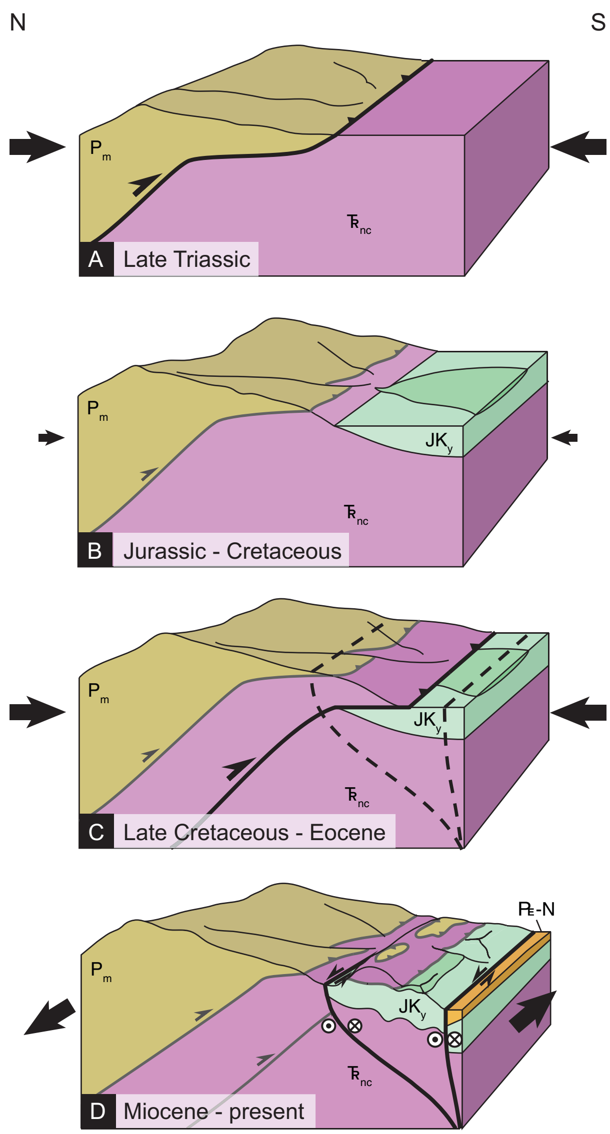
N
S
Pm
Ŧ̄Rnc
A Late Triassic
Pm
JKy
Ŧ̄Rnc
B Jurassic - Cretaceous
Pm
JKy
Ŧ̄Rnc
C Late Cretaceous - Eocene
Pε-N
Pm
JKy
Ŧ̄Rnc
D Miocene - present

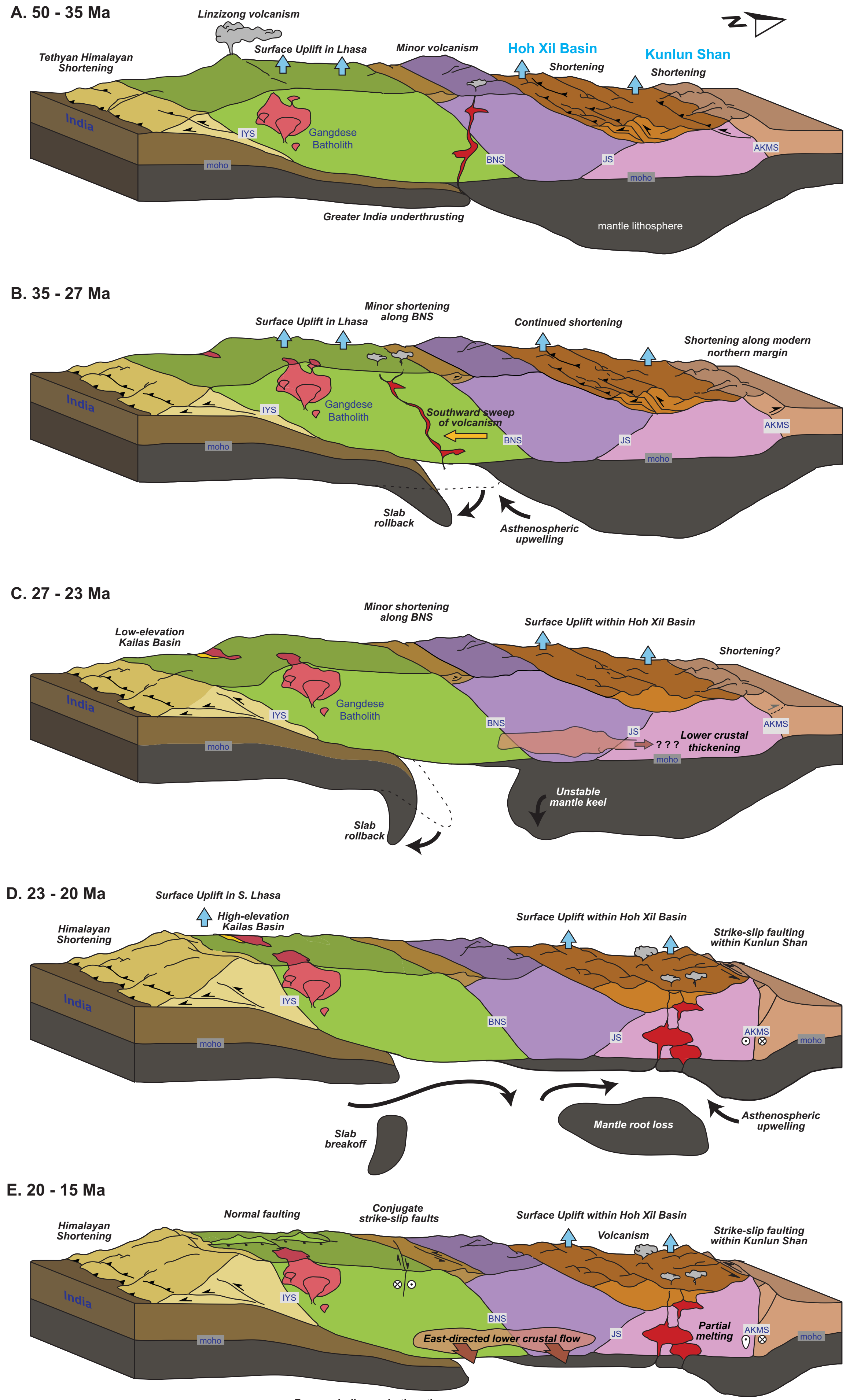

A. 50 - 35 Ma
Linzizong volcanism
Tethyan Himalayan Shortening
Surface Uplift in Lhasa
Minor volcanism
Hoh Xil Basin
Kunlun Shan
Shortening
Shortening
India
IYS
Gangdese Batholith
moho
BNS
JS
AKMS
moho
Greater India underthrusting
mantle lithosphere
B. 35 - 27 Ma
Minor shortening along BNS
Surface Uplift in Lhasa
Continued shortening
Shortening along modern northern margin
India
IYS
Gangdese Batholith
Southward sweep of volcanism
BNS
JS
AKMS
moho
moho
Slab rollback
Asthenospheric upwelling
C. 27 - 23 Ma
Minor shortening along BNS
Low-elevation Kailas Basin
Surface Uplift within Hoh Xil Basin
Shortening?
India
IYS
Gangdese Batholith
BNS
JS
AKMS
Lower crustal thickening
? ? ?
moho
moho
Unstable mantle keel
Slab rollback
D. 23 - 20 Ma
Surface Uplift in S. Lhasa
High-elevation Kailas Basin
Himalayan Shortening
Surface Uplift within Hoh Xil Basin
Strike-slip faulting within Kunlun Shan
India
IYS
BNS
JS
AKMS
moho
moho
Slab breakoff
Mantle root loss
Asthenospheric upwelling
E. 20 - 15 Ma
Himalayan Shortening
Normal faulting
Conjugate strike-slip faults
Surface Uplift within Hoh Xil Basin
Volcanism
Strike-slip faulting within Kunlun Shan
India
IYS
BNS
JS
East-directed lower crustal flow
Partial melting
AKMS
moho
moho
Resume Indian underthrusting

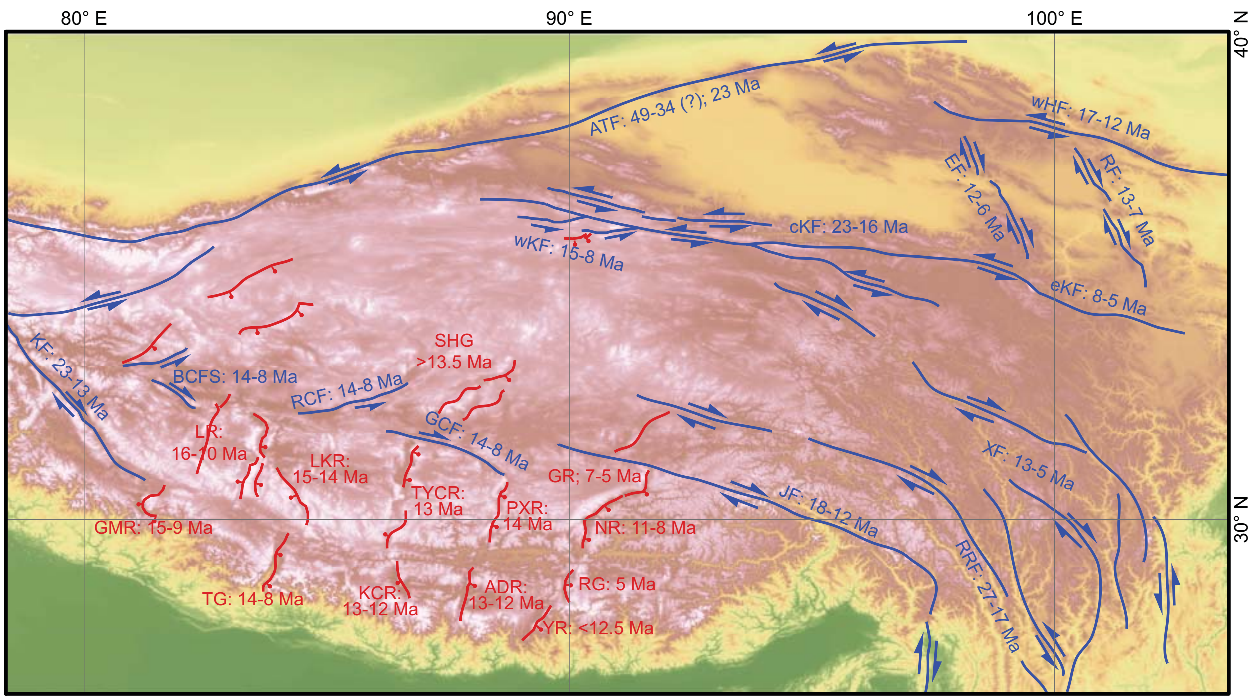
80° E
90° E
100° E
40° N
30° N
ATF: 49-34 (?); 23 Ma
wHF: 17-12 Ma
EF: 12-6 Ma
RF: 13-7 Ma
cKF: 23-16 Ma
wKF: 15-8 Ma
eKF: 8-5 Ma
KF: 23-13 Ma
BCFS: 14-8 Ma
RCF: 14-8 Ma
SHG
>13.5 Ma
GCF: 14-8 Ma
LR:
16-10 Ma
LKR:
15-14 Ma
TYCR:
13 Ma
PXR:
14 Ma
GR; 7-5 Ma
NR: 11-8 Ma
GMR: 15-9 Ma
TG: 14-8 Ma
KCR:
13-12 Ma
ADR:
13-12 Ma
RG: 5 Ma
YR: <12.5 Ma
JF: 18-12 Ma
XF: 13-5 Ma
RRF: 27-17 Ma